ENGINEERING BEHAVIOR OF TYPE I LIGHTWEIGHT CELLULAR CONCRETE AND THE EFFECTS OF PARTIAL SATURATION AND CONFINEMENT

by

Daniel DeSpain Barlow Seely

A dissertation submitted to the faculty of
The University of Utah
in partial fulfillment of the requirements for the degree of

Doctor of Philosophy

Department of Civil and Environmental Engineering

The University of Utah

August 2024

Copyright © Daniel DeSpain Barlow Seely 2024

All Rights Reserved

The University of Utah Graduate School

STATEMENT OF DISSERTATION APPROVAL

The dissertation of **Daniel DeSpain Barlow Seely**

has been approved by the following supervisory committee members:

Steven F. Bartlett	, Chair	**5/24/2024** Date Approved
Pedro Romero-Zambrana	, Member	**5/28/2024** Date Approved
Chris P. Pantelides	, Member	**5/25/2024** Date Approved
Evert C. Lawton	, Member	**5/31/2024** Date Approved
Jeffrey Ralston Moore	, Member	**5/24/2024** Date Approved

and by **Michael Ernest Barber** , Chair of

the Department of **Civil and Environmental Engineering**

and by Darryl P. Butt, Dean of The Graduate School.

ABSTRACT

Lightweight cellular concrete (LCC) is increasingly utilized in geotechnical applications; therefore, it is vital to understand engineering behavior under partially saturated field conditions. This study presented in this dissertation advances this knowledge by quantifying the effects of partial saturation on the low- and high-strain elastic moduli, and the ultimate shear strength at low to moderate levels of specimen confinement commonly encountered in roadway and retaining systems.

Back-pressure saturated hydraulic conductivity tests were performed on specimens prepared with a bentonite treatment to prevent hydraulic by-pass along the sidewall. Micro-computed tomography (CT) scans were performed on several specimens over a range of saturation from 1.6% to 35%. The results from this process were used to estimate the void size and pore water distribution within the partially saturated LCC.

A unique test protocol was developed and interpreted using a nonlinear regression model to evaluate the degree of saturation that may be expected in long-term field conditions. Unconfined compression strength (UCS) testing was also conducted at various curing times. A nonlinear regression model fitted to these data showed that the specimens gained almost all their long-term strength after 70 days. Therefore, standardizing a test protocol to 70+ days for subsequent testing allowed comparison of results minimizing curing effects.

Subsequently, test specimens were subjected to five partial saturation treatments, resulting in a range of saturation from 2.8% to 20.4%. These partially saturated test specimens were utilized in a testing program that included nondestructive resilient modulus (RM) testing, followed by either UCS testing or drained triaxial compressive strength testing.

Simple linear and multiple linear regression models (SLR & MLR) were developed using the data produced from the five treatment sets. These regression models include the initial yield stress, peak yield stress, and Young's modulus for unconfined and confined-drained axial compression. In addition, an MRL model for the RM under varying stress conditions was developed. Lastly, UCS and triaxial compression tests were paired with RM testing to establish a "surrogate" estimate of the RM for engineering practice. The predictive models are suggested for preliminary engineering estimations and are limited to the ranges presented for this study.

TABLE OF CONTENTS

ACKNOWLEDGMENTS

Aerix Industries graciously supplied the test specimens for this research project. Staff at Aerix Industries for whom I am thankful for their valuable advice for LCC testing and sample preparation. I'm thankful to the Mountain Plains Consortium which provided partial funding for the research.

I would thank IGES, Inc. who provided support for me throughout my graduate studies and allowed me unlimited access to their Geotechnical Laboratory for this research. I am appreciative of Jerry Flannery who was always willing to lend a helping hand with my research testing when needed.

I would like to express appreciation to my dissertation committee who challenged me where I needed it and were willing to give me their time and advice for my research. I and thankful to Dr. Lawton who taught me nearly everything I know about soil mechanics. Thank you to Dr. Bartlett who sought me out for this project and for his valuable guidance, advice, and wisdom throughout this research project – you've taught me more than you know.

Thank you to Ella who taught me how to work with the CT scan photos, to Syliva who helped with many specimen preparations, and to Henry who helped with the CT scans. Finally, thank you Amber for your patience and unconditional support throughout my graduate studies.

CHAPTER 1

INTRODUCTION

The ACI Committee 523 (2006) defines Lightweight Cellular Concrete (LCC) as a concrete product with an oven-dried unit weight of 50 pcf (800 kg/m3) or less and is made from hydraulic cement, water and preformed foam. Although not within the bounds set forth by the ACI, it is commonly accepted that LCC's unit weight ranges from 20 pcf to 120 pcf. LCC is also known as low-density cellular concrete (ACI Committee 523 2006), foamed concrete (Amran et al. 2015), lightweight foamed concrete (Kozłowski and Kadela 2018), low-density foam concrete (Song and Lange 2021), aerated concrete (Narayanan and Ramamurthy 2000), or simply cellular concrete (Lee et al. 2004).

Lightweight concrete was employed in construction as early as Roman times, where vesicular volcanic aggregates were included in concrete construction. The modern technology of LCC was first developed in the early 1900s in Sweden (Sutmoller 2020) and used in Europe and the United States as part of flooring systems. Cellular concrete was initially patented in 1923 by Axel Eriksson and was known as Ytong (Chica and Alzate 2019). A Swiss patent in 1932 by Siporex included a vapor curing process developed by Eklund (Chica and Alzate 2019; Taylor and Halsted 2021). Foamed concrete was used in the Soviet Union by Kudriashoff starting in 1938, where it was

employed for nonstructural construction elements (Chica and Alzate 2019). The use of LCC expanded through Europe and the rest of the world from the mid-1940s and began incorporating hydrolyzed protein-based foams, increasing the quality control of LCC production (Sutmoller 2020). The United Kingdom was introduced to LCC in the 1950s for load-bearing applications, including coal slag from thermoelectric plants (Chica and Alzate 2019). LCC technology was applied in oil wells and as fill for excavations around 1970 (Chica and Alzate 2019). In 1980, the Falkirk railway tunnel in Scotland utilized approximately 4,500 m^3 of LCC for the first large-scale project using LCC as fill (Chica and Alzate 2019). These introductions made advances in the production and quality of LCC of synthetic-based foam liquid concentrates in the early 1990s, which brought more stability to the foam air cells and the longevity of the LCC (Sutmoller 2020). Typical lightweight cellular concrete is considered a relatively impervious (i.e., impermeable) material but may also be classified as permeable using modern hybrid foam. These foams, consisting of protein-based and synthetic-based concentrates, were developed in the early 2000s, introducing permeable lightweight cellular concrete with a connecting open cell structure known as PLCC (Sutmoller 2020).

Many of the recent advancements in LCC technology involve the use of additives. These additives include fly ash, peroxide, slag, silica fume, sugarcane filter cake, laterite, palm oil fuel ash, waste clay brick, clay brick, soil, plastic waste (PE, PVC), recycled waste (glass, plastic), expanded polystyrene foam (EPS), latex, salt waste, polypropylene fibers, quick lime, poly-olefin, silica powders, sand, kaolin, bentonite food additives (methylcellulose, iota carrageenan gum), PVA fibers, cenospheres (Chica and Alzate 2019), vermiculite, perlite, water-reducing admixtures, set accelerators, high-reactivity

metakaolin (ACI Committee 523 2006). Many of the advances in additive constituents are driven by improvements for structural applications in Civil Engineering.

The primary advantages of LCC are (1) a significant reduction in weight, (2) thermal and acoustic insulation, (3) fire resistance, (4) relatively lower cost of production when compared with typical concrete, (5) ease of mixing and pumping, (6) omission of vibration during the placement as needed in typical concrete placement, and (7), does not require compaction like typical fill soils (Chica and Alzate 2019).

LCC is increasingly utilized in highway projects as a lightweight fill for settlement mitigation applications. Approximately 65,000 cubic yards of LCC have recently been used for new highway construction on the West Davis Corridor in Davis County, UT, which opened to the public in January 2024. Applications for LCC on that project included rapid embankment construction, bridge approaches, MSE wall backfill, and backfill over sensitive utilities. A fundamental understanding of the geotechnical engineering properties of LCC is crucial to the success of construction projects and long-term performance throughout the design life in which LCC is employed.

Literature Review and Previous Research

Although its primary constituent is Portland cement, LCC does not necessarily behave as typical concrete. Most LCC projects do not incorporate steel reinforcement or aggregates typically used in structural and pavement concrete. Almost all the research and testing defining the engineering properties of LCC has taken a hybrid approach based on soil, rock, and concrete testing. However, LCC is not soil, rock, or conventional concrete. With this in mind, LCC should be considered an intermediate material from a

geotechnical and materials standpoint. Lastly, it is vital to consider the method of production, the LCC density and strength classification, the mix design, and other additives when evaluating data published in the literature.

LCC may be generally classified by its unit weight and compressive strength, as shown in Table 1 (Aerix Industries n.d.). Much of the laboratory characterization of LCC follows the typical concrete strength protocol, defined by the compressive strength (unconfined, uniaxial) as a function of curing time. Also, as customary, the 28-day compressive strength is the defining strength characterization for LCC. The compressive strength of LCC should be performed per ASTM C796 and C495 (ACI Committee 523 2006; ASTM C09 Committee 2012, 2019a).

The determination of the as-cast density of LCC is described in ASTM C796, while the sampling and testing of insulating LCC are to be performed per ASTM C513 (ASTM C09 Committee 2011a, 2019a). The coefficient of thermal expansion is typically 5.0×10^{-6} to 7.0×10^{-6}/°F but varies with density (ACI Committee 523 2006).
The determination of the thermal conductivity is performed per ASTM C177, C518, and C1363 (ASTM C16 Committee 2019a; b, 2021), while the fire resistance of LCC is controlled per ASTM E119 (ASTM E05 Committee 2020).

The permeability or, more appropriately, hydraulic conductivity of closed cell LCC is typically in the range of 10^{-5} cm/sec to 10^{-6} cm/sec. This property is generally performed per ASTM D2434 (ASTM D18 Committee 2019a), with freezing and thawing evaluated per ASTM C666 (ASTM C09 Committee 2015). LCC mixtures are assessed per ASTM C796 and C869 (ASTM C09 Committee 2011b, 2019a). Also, Kearsley and

Wainwright (2001) have developed a methodology to optimize the fly ash content for strength.

René Féret was the first to develop a relationship for concrete strength in 1896, including the air volume as a variable.

$$f_c = K\left(\frac{c}{c+w+a}\right)^2 \quad (1)$$

where f_c (MPa) is the compressive strength of concrete, K is a constant, c is the volumetric proportion of cement, w is the volumetric proportion of water, and a is the volumetric proportion of air (Kearsley and Wainwright 2002). Additionally, Kearsley and Wainwright (2002) have determined experimentally that the compressive strength of LCC may be determined by

$$f_c = 39.6(\ln(t))^{1.174}(1-p)^{3.6} \quad (2)$$

where t is the time or age since casting in days and p is the mature porosity measured after one year. A plot of the compressive strength as a function of the porosity from Equation 2 is shown in Figure 1.

The vacuum saturation porosity (%), P, of LCC may be determined by

$$P = \frac{W_{sat} - W_{dry}}{W_{sat} - W_{wat}} \quad (3)$$

where W_{sat} is the weight in air of the saturated specimen, W_{wat} is the weight in water of the saturated sample, and W_{dry} is the weight of the oven-dried sample. For this relationship, the specimens were oven-dried to a constant weight, placed in a desiccator under vacuum for at least 3 hours, and then filled with de-aired distilled water (Cabrera and Lynsdale 1988).

Various alternative methods have been evaluated to determine LCC's porosity, including 1) freeze-drying, vacuum-drying, 2) oven-drying at 60°C, and 3) oven-drying at 105°C. The last method produces the highest porosity but perhaps overestimates the true porosity due to damage to the microstructure (Galle 2001). Galle (2001) also suggests that the most appropriate method of porosity determination is the freeze-drying method.

Tikalsky et al. (2004) have developed a modified freeze-thaw procedure that involves saturation of the LCC specimens before the freeze-thaw cycling. The study has shown that strength, depth of initial water penetration, absorption, and absorption rate all affect the freeze-thaw durability of LCC. These authors demonstrated that the density and permeability of the LCC are not significant variables in freeze-thaw durability. However, further research should be undertaken to generate a more extensive data set to characterize the freeze-thaw durability of LCC further and more completely.

A comprehensive experimental study was undertaken at the Sandia National Laboratories to determine the mechanical material properties of cellular concrete with controlled unit weights of 62.4 pcf and 87.4 pcf. This testing program included uniaxial compression, triaxial compression, uniaxial strain, extension, and tension tests (Lee et al. 2004). The Sandia study generated constitutive models based on the cap plasticity models (Sandler and Rubin 1979) for both unit weight classes.

Kearsley and Wainwright (2002) showed that the strength of LCC is dependent mainly on dry density and age but not necessarily affected by the ash type or ash content. In contrast, Jones and McCarthy (2005) have shown that using fly ash in foamed concrete significantly improves its properties (e.g., reducing the heat of hydration).

A contributing study was undertaken with LCC used as subgrade fill. This study found that adding fly ash contributed to strengthening the LCC. The strengthening effect was due to pozzolanic and hydration reactions, which aided the densification of the structural skeleton (Liu et al. 2020). Liu et al. (2020) recommend a fly ash content of 25 percent to optimize this admixture. Using fly ash as an admixture in LCC has also created a more uniform air void distribution and consistent air voids (Nambiar and Ramamurthy 2007). Nambiar and Ramamurthy (2007) have also shown that the air void shape in LCC does not necessarily significantly affect LCC properties. Narayanan and Ramamurthy (2000) and Ramamurthy et al. (2009) provide overviews of the data and relationships in the literature.

As LCC is used more in geotechnical applications, the performance of LCC during earthquakes has been an area of research interest. Tiwari et al. (2018) undertook a study to investigate the response of LCC under dynamic loading under cyclic simple shear testing. Specimens utilized in the study were Class II and Class IV LCC. Data sets and models were generated for dynamic backbone curves, maximum shear modulus curves, modulus reduction curves, and damping curves.

Song and Lange (2021) presented data on the dynamic Young's modulus measurement using the resonant column test per ASTM C215 (ASTM C09 Committee 2019b). Unit weights of the LCC considered in the study ranged from 25.5 pcf to 123.5 pcf. As expected, the dynamic Young's modulus exhibited a dependence on the unit weight of the LCC. This relation was expressed as an exponential increase in stiffness with an increase in unit weight.

To date, the studies of Lee et al. (2004), Song and Lange (2021), and (Tiwari et al. 2017, 2018) show the most comprehensive material property evaluations applicable to the geotechnical implementation of LCC.

Geotechnical Engineering Applications

According to ACI Committee 523 (2006), geotechnical engineering applications of LCC includer embankments, roadway bases, pipeline and culvert backfills, void space and tank infills, and insulation and isolation fills. In most cases, LCC offers advantages over other earthen commonly used materials in geotechnical engineering. These advantages include low density, ease of excavation, relatively controllable strength, strength advantages over conventional compacted soil, high resistance to freeze-thaw, self-leveling and consolidation behavior, favorable energy dissipation and damping, inert and nonflammable properties, and construction with LCC requires less transportation costs. Teig and Anderson (2012) suggest the following benefits of the use of LCC: 1) lighter and stronger than conventional compacted soil, 2) small equipment used in construction leading to lower environmental impacts, 3) bridge abutments may experience significantly reduced lateral earth pressures and small live load surcharges. 4) block-like behavior (similar to geofoam) and reduced inertial effects in seismic conditions, 5) reduced imposed settlements compared to conventional compacted soil fill, and 6) up to 30% cost savings as compared to conventional cast-in-place concrete walls with soil fills. Additionally, Taylor and Halsted (2021) listed the following alternate advantages: 1) LCC provides for aggregate conservations, 2) resistance to freeze-thaw, 3) self-leveling and consolidation, 4) energy dissipation and damping, 5) LCC is very

excavatable, 6) LCC is considered inert and nonflammable, 7) materials may be locally sourced, 8) LCC is easily pumpable, 9) construction with LCC requires fewer transportation costs and reduces emissions, and finally, 10) LCC construction offers worker safety advantages.

Backfill

LCC has been placed adjacent to bridge abutments and retaining walls as a lightweight fill to reduce settlement, and due to its cementitious nature, it requires no compaction. According to ACI Committee 523 (2006), the general fill should comprise 30 pcf material. Still, the upper two to three feet of the fill should consist of 42 pcf material so that this material is less susceptible to frost damage and provides a solid base for pavement or approach slabs.

Several instances demonstrate that LCC may be used as mechanically stabilized earth wall (MSE) fill (Bartlett 2015; Pradel and Tiwari 2015; Sutmoller 2020; Teig and Anderson 2012; Tiwari et al. 2017, 2018). Bartlett (2015) suggested using Rankine Theory for lateral earth pressures using the effective friction angle obtained from direct simple shear tests and a relatively low cohesion intercept. Tiwari et al. (2017) suggest using a stress-dependent effective friction angle and zero cohesion for MSE external stability calculations. Also, numerical analyses of LCC used as MSE wall fill reinforced with geogrid behave as a semi-rigid body under cyclic conditions and perform well (Pradel and Tiwari 2015).

Teig and Anderson (2012) reported an embankment fill over the Colton railway flyover that utilized LCC due to settlement and right-of-way constraints imposed on the

project. The project required a relatively high seismic design acceleration criterion. A numerical evaluation method was developed for this project based on previous work performed in similar geomaterials and applications by Bartlett et al. (2011) and Bartlett and Lawton (2008).

Roadways

LCC has been used in roadway construction as a base over soft soils. When used as such, LCC has been shown to span localized settlements up to 3.2 ft (ACI Committee 523 2006). Sutmoller (2020) and Taylor and Halsted (2021) have noted advantages when LCC has been used for subgrade modifications and improvements. Also, work was undertaken by Decký et al. (2016) to back-calculate the modulus of LCC by in-situ testing of a sand subgrade and LCC base material. The study was based on the theoretical 2-layer Sojuzdornii equivalent deformation model. Lastly, Averyanov (2018) undertook extensive research evaluating using LCC in soft soil conditions as a base material in a pavement section. The study showed many advantages to using LCC as a base material, particularly a reduction in the depth of over-excavation and the replacement of poor subgrade materials.

Inti et al. (2021) suggest the advantageous use of PLCC in pervious parking lot sections to replace the granular subbase. Testing indicated the PLCC demonstrated sufficient strength and permeability with infiltration rates of about 700 in./hr. These authors found that the density of the PLCC is critical when considering the strength, infiltration rate, and water storage. Effluents from infiltration typically showed a higher pH and alkalinity than conventional granular permeable pavement sections.

Pipeline and Culvert Fills

Allen and Meade (1984) discuss an embankment fill on I-275 in Kentucky, where LCC was utilized as an embankment material spanning an existing box culvert. The vertical stresses caused by conventional fill (soil) would exceed the box culverts' structural capacity. Hence, LCC was a lightweight material for embankment construction that reached heights up to 47 feet. The dry unit weight of the LCC used for the project was 25 to 30 percent of conventional fill, but saturated LCC unit weights were about 60 to 70 percent of traditional embankment material. The report details construction methods, laboratory test results, and instrumentation. Class II test specimens were subjected to 20 cycles of temperature changes from 0 to 70 °F. Unfortunately, some specimens completely disintegrated under these test conditions. The instrumentation data seems inconclusive and merits more evaluation.

Void Fills

LCC is an effective material for large void fills where flowability is a factor and a reduction in dead load is desired. Examples of void fills are abandoned swimming pools, abandoned pipelines, excavations, annular spaces around pipelines, undemolished structures, tunnels, and underground fuel or oil tanks (ACI Committee 523 2006; Sutmoller 2020). Federal regulations indicate that LCC is an inert substance for abandonment applications (ACI Committee 523 2006).Insulation and Isolation

Fills and Miscellaneous Applications

Regions that experience permafrost conditions have typically employed crushed-rock air convection embankment (ACE) technologies to prevent permafrost from thawing in road constructions. ACE is an insulator in summer and a convection cooler in winter conditions. Wu et al. (2020) undertook a study in which numerical simulations compared the performance of typical ACE embankments and the replacement of crushed rock with LCC. The study indicates that LCC has better thermal conductivity and heat capacity performance with a reduced cost. Advantages, as seen elsewhere, are the reduction of the environmental impact resulting from the installation. Additional insulation and isolation applications are possible for utility protection and geothermal utility insulation (Sutmoller 2020).

LCC has been used with EPS for a potential fault crossing. The LCC and EPS system was designed to absorb fault offset over a water pipeline in a rupture event (Taylor 2015). Lastly, LCC blocks have been used as an energy dissipation system for runaway truck ramps, particularly for airplanes adopted by the FAA (Taylor and Halsted 2021). Other applications Taylor and Halsted (2021) presented include lightweight dam and levee structural fills, landslide repair, and slope stabilization.

Durability

The durability of LCC from a highway/roadway perspective is the ability of the material to last through the design life of the application under conditions of varying water content, chemical attack from both natural water sources and potential roadway surface contaminants, and resisting damage from repetitive traffic loading. LCC's degree

of durability depends on the material's location within the pavement section as a direct function of the traffic loading, confinement, and strains. Also, the vertical position of the LCC in a pavement system may affect its freeze-thaw susceptibility. For example, if the LCC is placed sufficiently deep, where nightly temperature changes are insignificant, the performance of the LCC may not be adversely impacted by frost.

Lannen et al. (2018) characterized the strength of cellular grout and abrasion resistance. Abrasion testing protocols were per ASTM C1138M-19 Standard Test Method for Abrasion Resistance of Concrete (Underwater Method) (ASTM C09 Committee 2019c). Their study consisted of cellular grout samples with unit weights ranging from 90 pcf to 110 pcf, representing the high end of LCC unit weights. The general testing protocol outlined in ASTM C1138M-19 involves the agitation of a concrete specimen submerged underwater using a rotating agitator that moves a set of hardened chrome steel grinding balls of varying prescribed sizes. The testing results report the mass or volume loss due to the abrasion, which occurs after a specified duration of agitation. Lannen et al. (2018) also reported the average depth of abrasion.

Liu et al. (2019) studied a selection of factors influencing durability, which include wet density, compressive strength, filling aspect ratio, safety factor, slope rate of connecting surface, steel wire mesh setting, production equipment, agitation sufficient degree, flow valve, single layer pouring thickness, single layer pouring time, interlayer pouring interval time, construction environment, curing time, vehicle load, drainage condition, chemical corrosion, and temperature change. Although the highlight of the paper is the application of fuzzy logic utilizing the Analytical Hierarchy Process (AHP) and Fuzzy Comprehensive Evaluation (FCE), the inputs to the study are of interest from a

durability standpoint. Some areas of the study address project-specific durability concerns and are not likely to have significant research impacts concerning highway/roadway applications. Curing time is an important consideration when developing research or a testing program for durability. Any testing results will vary due to LCC's mechanical and chemical behavior being dependent on the rate of reaction cure time. Of most importance for applying LCC to highway and roadway durability conditions are items are the wet density, compressive strength, vehicle load, drainage condition, chemical corrosion, and temperature change, respectively.

The unit weight or density of the LCC will primarily be a function of the design and reflected in the project specifications. However, the in-place (i.e., wet) density will be influenced by natural wetting-induced changes in water content resulting from surface infiltration or subsurface unsaturated flow. Tiwari et al. (2017) state that LCC has a low water absorption ability, suggesting that some research has been undertaken to address absorption. The authors report LCC hydraulic conductivities from 10^{-3} cm/sec to 10^{-6} cm/sec, which supports the notion that water absorption may be relatively low. However, when coupled with LCC's open vesicular pore structure, this relatively low hydraulic conductivity suggests that water absorption may be controlled by diffusion rather than advective flow. Even though LCC's potential for water adsorption is a site/project-specific factor, the range of its influence on the mechanical properties of LCC will be addressed in this research.

Past studies have convincingly demonstrated correlation of LCC's unconfined compressive strength (UCS) with cast density. Thus, the in-situ UCS of LCC will always be important in project design and construction. Because of this, the UCS of test samples

is often used as an "index" measure of the quality of the LCC mix. Kozłowski and Kadela (2018), Namsone et al. (2017), and Tiwari et al. (2017), among many others, have suggested relationships in the form of regression equations for the UCS as a function of the unit weight or density.

The durability of LCC as a function of temperature change is an important aspect to consider in the highway/roadway application. Tiwari et al. (2017) have suggested that LCC has a high freeze-thaw resistivity, but no confirmation data was given in their study. However, this subject has also been discussed in the research of Kozłowski and Kadela (2018).

In addition, a Latvian study on LCC durability was conducted and reported by Namsone et al. (2017). It included the durability aspects of strength, density, water absorption, carbonization, and frost resistance. One unique durability aspect explored by Namsone et al. (2017) is the tendency of LCC to exhibit shrinkage. The authors argue that shrinkage is due to cement hydration and water loss and that shrinkage causes strength reduction and increases thermal conductivity and susceptibility to freeze-thaw cycles. Carbonation, a process that transforms $Ca(OH)_2$ to $CaCO_3$, does not necessarily appear to affect compressive strength, but it does influence shrinkage. The results indicate that carbonation depth is typically less than six mm. These authors further suggest that analyzing the experimental data shows a correlation between water absorption, carbonation depth, and compressive strength; however, they do not present any correlation plots. Independently, the frost resistance and carbonation were qualitatively observed. Nonetheless, additional research is needed to correlate durability factors with UCS values. This exploration would be of value to practicing engineers.

Like most research papers involving LCC, Kozłowski and Kadela (2018) have reported on testing to address the apparent density and compressive strength. Additionally, these authors investigated the modulus of elasticity, flexural strength, and LCC degradation under freeze-thaw cycles. The modulus of elasticity and flexural strength are important factors to consider when including LCC as a structural component in a pavement section. Still, these factors are not necessarily direct indicators of durability. The data and degradation analysis based on the number of freeze-thaw cycles was done by comparing the compressive strength after 25 freeze-thaw cycles. Kozłowski and Kadela (2018) have reported an approximately 15% reduction in strength after being subjected to the freeze-thaw cycles, a relatively modest decrease from a durability standpoint.

The most comprehensive study on LCC's mechanical properties was published by Tiwari et al. (2017). Their study includes laboratory testing on Class II and Class IV LCC specimens with a range of 19.7 pcf to 47.7 pcf unit weights. The test methods in the study include cast and cured unit weight, unconfined compressive strength, direct shear strength, direct simple shear strength, isotropically consolidated-drained and consolidated-undrained triaxial compressive strength, K_0 consolidation, hydraulic conductivity, and one-dimensional consolidation. The saturated direct simple shear effective friction averaged 35° with an effective cohesion intercept of 750 psf. The effective friction angle obtained from the consolidated drained and undrained triaxial compression shearing mode of the saturated test specimens averaged 34° with an effective cohesion intercept of 1,630 psf.

The results from the K_0 consolidation testing showed a range from 0.2 to 0.5, corresponding to Poisson's ratio values from 0.2 to 0.3, respectively. Class II LCC exhibited significant deformation with vertical stresses higher than 6,250 psf, while Class IV LCC showed considerable deformation with vertical stresses higher than 14,600 psf. The data generated by the study seems to indicate that the strength and stiffness of the LCC generally decrease with 100% saturation. The hydraulic conductivity testing was performed using ASTM D5084 (ASTM D18 Committee 2016a), commonly known as the flexible-wall or back-pressure saturated permeability. The hydraulic conductivity results ranged from 1.7×10^{-4} cm/sec to 1.2×10^{-3} cm/sec, indicating no decrease in permeability with an increase in effective confining stress.

The test data presented mainly applies to the general geotechnical design aspects to be encountered in a project involving LCC, particularly for applying LCC backfill for MSE retaining walls. It was noted that the strain rate used in the unconfined compressive strength testing was 0.5%/hr, which is exceptionally low and would tend to underestimate the strength of the LCC cylinders significantly. Also noted was that the hydraulic conductivity test results showed no appreciable change when subjected to varying effective confining stresses. However, this result is contrary to intuition and experience. Admittedly, Tiwari et al. (2017) have identified hydraulic conductivity as an area that requires additional research. It is apparent that the durability information and conclusions derived from the paper are interpretive. Also, the testing was stress-controlled and not strain-controlled, which limits the data value in use from a service-limit state perspective, the limit state most applicable to pavement design.

Knowledge Gaps

Previous research has been conducted on LCC, including a history of the usage and characterization of various engineering parameters. Geotechnical applications include backfill, roadways, pipelines, culvert backfill, void fills, insulation and isolation fills, and durability.

Because the data presented by Lannen et al. (2018) is very brief and specific to the high end of the LCC unit weight range, the findings do not apply to evaluating the durability of typical LCC as a potential base or subbase material or as a underlayment for bridge approach slabs. In these applications, the LCC will not be a wearing surface; hence, it will not be subjected to abrasion from traffic loading. Also, modeling suggests that pavement materials typically undergo induced tensile strains from 10^{-5} to 10^{-7} at the pavement-base interface. Hence, the high-strain abrasion action produced by the ASTM C1138M-19 test procedure does not represent the small-strain levels incurred at the pavement-LCC base interface; therefore, the test is too aggressive for the applications suggested above.

Another important topic absent in the current literature is defining the point in time when the mechanical and durability behavior of the LCC has reached a steady state. This research defines this point as when sufficient hydration reaction has occurred where no appreciable strength gain is demonstrated with additional curing time. Therefore, strength and durability test data are only comparable when the hydration reaction is sufficiently complete. For example, from a construction standpoint, the LCC product will not be put into traffic service until a certain level of curing has occurred. From a design standpoint, the "steady state" properties are needed to evaluate the serviceability

and ultimate limit states for various failure mechanics and live and dead-loading combinations.

Another aspect of durability that requires detailed evaluation is the effect of the degree of saturation or water content on the mechanical behavior of LCC. Data presented by Tiwari et al. (2017) suggest that saturating the LCC to 100% yields a decrease in compressive strength. However, this conclusion is not substantiated by the test data reported therein. Hence, the study does not provide a means of vetting the conclusion or exploring the effects of varying saturation states on the mechanical and durability properties.

A vital engineering property for the design of roadways is the stiffness or low-strain modulus of the pavement system materials. It is apparent in the literature that the modulus available is derived from the stress-strain data of testing using monotonic loading at moderate to high levels of strain. However, traffic loading impulses are relatively low-strain and time-dependent. In addition, the magnitude of the induced pressure depends on the various vehicle types' weight and wheel loading configurations. The pavement's modulus is typically dependent on the state of stress and the confinement of the pavement material. LCC's resilient modulus (RM) is an additional engineering property missing in research literature and engineering practice. This property is an essential input for mechanistic pavement design and can be performed in a triaxial cell used in geotechnical soil testing. The RM testing protocol is performed per AASHTO Technical Subcommittee: 1a, Soil and Unbound Recycled Materials 2017). The axial load is applied to a cylindrical test specimen using a haversine-shaped load pulse, which simulates traffic loading. The confinement and load amplitude are varied throughout the

test, producing a stress-dependent modulus of elasticity. Since the loading simulates traffic loading, it also addresses the long-term durability of LCC.

Problem Statement

The use of LCC for geotechnical applications is rapidly increasing in popularity, particularly in roadway projects. As discussed previously, LCC has many advantages over conventional compacted soils in roadway projects and is typically utilized for vertical stress reduction and the resulting settlement mitigation.

Except for one direct shear test, published laboratory test data has been generated on either fully saturated or "dry" test specimens; both states are rarely if ever, achieved in pavement applications. For example, partial saturation is inevitable as surface runoff infiltrates pavement sections through pathways from cracking, expansion joints, damage, etc. Projects with relatively high groundwater tables may partially saturate LCC as the matric suction increases saturation. Therefore, accounting for the degree of saturation as it changes with time and its effect on LCC's behavior and engineering properties is essential to advance the state of knowledge.

Because LCC is subject to a curing process driven by a hydration reaction, there is an elapsed time where testing may be undertaken to reasonably define the long-term (i.e., steady state) properties for comparative purposes. The literature review has discovered a research gap addressing this phenomenon and concept.

Although the cyclic loading behavior of LCC has been briefly explored and published, the data applies to geotechnical earthquake engineering. Due to the advantages of using LCC for roadway applications, it is a natural progression to utilize

LCC as a base or subbase material in constructing pavement sections and approach slabs. No data has been published on the pertinent engineering properties (i.e., RM), moisture effects, and durability of LCC undergoing repetitive, simulated traffic loadings.

Research Contributions and Goals

The primary research contributions and goals are as follows. 1) Because LCC is subject to curing, which changes the material behavior with time, suites of tests or comparisons of test results are complex or invalid when tests are performed at various curing stages. Thus, this research seeks to establish the elapsed time (i.e., the time for curing) before material testing or evaluation of the tests should commence. 2) The current literature presents test results for dry or "fully" saturated conditions. However, these water content states represent the endpoints of the saturation spectrum and are less likely to be encountered in field applications of LCC. Unfortunately, the effects of the degree of saturation on the material behavior of LCC remain primarily unknown and not discussed in the literature. Thus, an essential goal of this research is to generate representative geotechnical material properties (e.g., compressive strength, stiffness, low-strain moduli, durability, etc.) at varying degrees of saturation. This current study will employ both UCS, isotropically consolidated drained triaxial (CIDTx) compressive strength, and RM testing to evaluate the effects of saturation on LCC's mechanical and durability properties. This research envisions that LCC will have relatively widespread application as a base or subbase replacement in pavement systems. Unfortunately, current research and engineering practice lack the critical material properties required for incorporating LCC into the design and construction of pavement sections. The most

obvious example is that no RM data have been published to support mechanistic pavement design. Thus, this research will generate data on resilient moduli values at varying degrees of LCC saturation. This evaluation will allow the incorporation of LCC in mechanistic pavement design as a stronger and stiffer material than many compacted soils. 3) There is also little understanding regarding the effects of sample confinement on hydraulic conductivity. Thus, another research objective is to evaluate whether variations in the effective confinement pressure affect the hydraulic conductivity of LCC. 4) Also, because RM testing is relatively specialized and expensive, the data generated from the UCS and CIDTx tests will be compared and correlated to develop models for estimating the RM for these standard tests. This new knowledge can also be used to support LCC mechanistic pavement design. 5) Lastly, empirical models will also be developed to appropriately evaluate the degree of saturation's effects on LCC's engineering behavior, focused primarily on the stiffness (i.e., initial modulus) of the LCC as measured by the RM tests.

We believe these evaluations are warranted and necessary to contribute to the state-of-the-art knowledge regarding LCC's mechanical behavior and properties. In addition, the anticipated widespread application of LCC for pavement and other roadway systems requiring rapid construction techniques positions this study to become a significant contribution to engineering practice.

Research Tasks

The first task of the current research is to characterize LCC samples cast from three batches: Batch 1 (B1), Batch 2 (B2), and Batch 3 (B3). These batches have

corresponding average batch cast unit weights of 27.7 pcf, 28.2 pcf, and 28.6 pcf, respectively, averaging 28.2 pcf as a population. A total of 35 Styrofoam cylinder mold boxes, each containing four samples, were filled, totaling 140 samples. The initial phase of the test program revolved around the unconfined or unconfined compressive strength (UCS) of the LCC cylinders as a function of time. The UCS tests were performed to a point where no appreciable gain in strength was observed with time, at which point the remaining testing program commenced. Due to the strength change with time, testing must either be performed simultaneously (impossible due to limited equipment availability) or when the strength increase is no longer significant. If so, the tests performed using this latter approach have comparable and implementable results.

Because the degree of saturation is not a direct measurement and is computed through phase relationships, the specific gravity of the solids in LCC must be determined. Four specific gravity determinations were performed on each of the three batches of LCC.

The saturated hydraulic conductivity were measured on three specimens from of each of the batches of LCC per ASTM D5084 (ASTM D18 Committee 2016a) in a staged fashion with the effective confining stresses of 2.5 psi, 5 psi, 7.5 psi, and 10 psi.

LCC samples (60 in total) were subjected to various treatments to produce specimens over a range of degrees of saturation. The samples were be subjected to an air-dried treatment (AD), exposure to a 100% humidity environment for one week (H100), submerged in water for 5 minutes, then exposed to a 100% humidity environment for one week (M5), submerged in water for one day, then exposed to a 100% humidity

environment for one week (D1), and finally submerged in water for one week, then exposed to a 100% humidity environment for one week (W1).

A simple model based on regression analysis is developed to indicate the range of possible degrees of saturation of LCC due to burial in a high-humidity environment.

Once the saturation treatment for the individual specimens was complete, all specimens underwent a primary RM test per the base loading schedule from AASHTO T307 (AASHTO Technical Subcommittee: 1a, Soil and Unbound Recycled Materials 2017). Since the range of stresses in the RM tests is in the range of elastic deformation for LCC, subsequent secondary tests can be performed and provide a one-to-one compassion between the primary and secondary tests. As the RM is expressed and a culmination of all stress conditions, the results were initially evaluated using commonly accepted model forms as shown and discussed in Von Quintus and Killingsworth (1998).

Several test specimens were selected for UCS and CIDTx tests in general accordance with ASTM C796 and C495 (ASTM C09 Committee 2012, 2019a) and ASTM D2166 (ASTM D18 Committee 2016b). We note that all compressive tests on the unconfined and triaxial specimens were tested after the RM test sequence was performed. The subsequent compressive testing is valid because the RM test is nondestructive, and its low-strain load cycling does not significantly affect the results for the high-strain, destructive compression tests. In addition, upon completion of the compressive testing and in quick succession, a water content determination was conducted following ASTM D2216 (ASTM D18 Committee 2016b) for these specimens.

Ultimately, correlative models based on regression analysis were developed from the secondary surrogate tests (unconfined and triaxial compression) to estimate the RM

from these standard geotechnical tests and to explore the effects of saturation on the engineering behavior of LCC. Finally, an estimated strength for LCC is proposed in terms of the Mohr-Coulomb strength envelope derived from the CIDTx strength tests.

Table 1. General classification of LCC.
LCC classification is generally based on the density or unit weight and the minimum unconfined compressive strength at 28 days.

Class	LCC unit weight (pcf)	Minimum compressive strength at 28 days (psi)
I	24-29	10
II	30-35	40
III	36-41	80
IV	42-49	120
V	50-79	160
VI	80-90	300

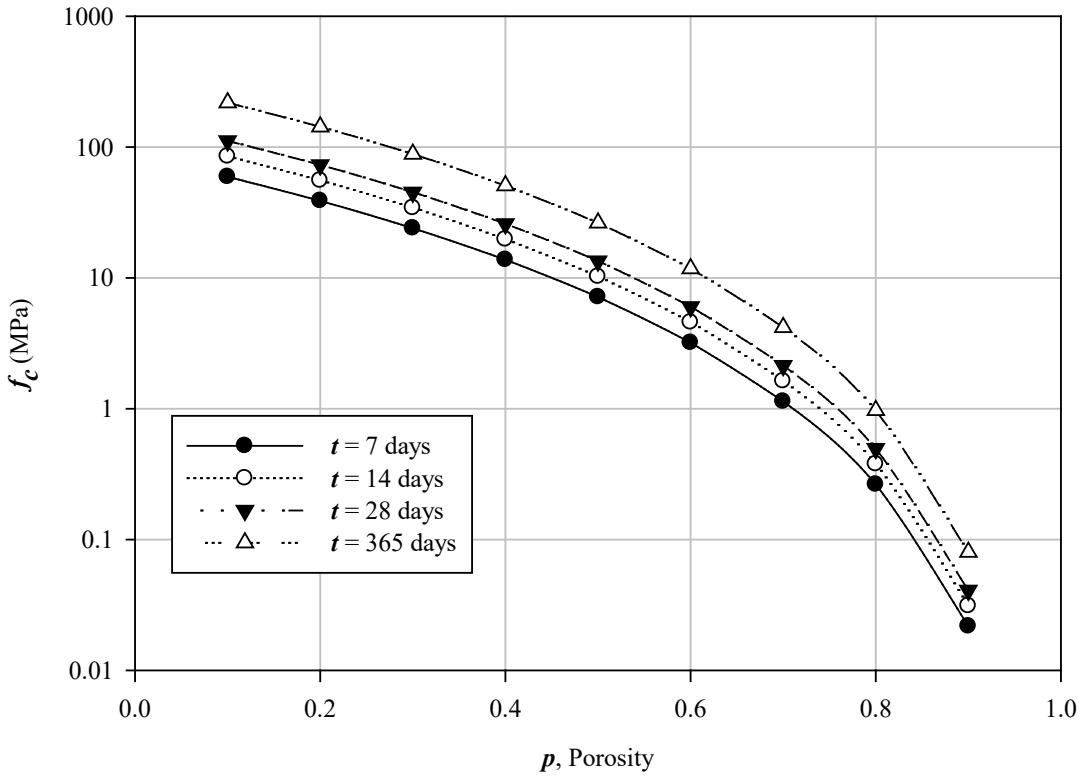

Figure 1. Estimated unconfined compressive strength as a function of porosity and time.

Intuitively, the strength of LCC increases with a decrease in porosity and increases with time as the curing reaction progresses. The steady-state strength as a function of time, however, is not apparent.

CHAPTER 2

LCC MATERIAL CHARACTERIZATION

Batch Design and Samples

The LCC cylinders utilized in this study, with a target density of 28 pcf, were batched on 5/26/2020 at and by Aerix Industries in Golden, CO. The sample cylinders, with an Aerix Sample ID of 20-600, were cast from three batches, Batch 1 (B1), Batch 2 (B2), and Batch 3 (B3), with corresponding cast unit weights of 27.7 pcf, 28.2 pcf, and 28.6 pcf, respectively. The cylinders had a nominal diameter of three inches and a nominal length of six inches. A total of 35 Styrofoam cylinder molds containing four samples were filled, totaling 140 samples. Aerix retained two molds (eight total samples) from Batch 1 for comparative unconfined compression testing, two each at seven, 14, 28, and 56 days. An excerpt of the mix design report Aerix Industries is shown in Figure 2.

The samples were allowed to cure at the Aerix laboratory for one day, after which the Styrofoam cylinder molds were carefully packaged into three 45-gallon plastic storage bins and strapped onto two separate pallets for shipping. Reddaway picked up the pallets in the early evening of 5/28/2020. The pallets arrived at the Intermountain GeoEnvironmental Services, Inc. (IGES) geotechnical laboratory in South Salt Lake, UT, on the morning of 6/1/2020. The samples arrived in good condition with no signs of

damage. A total of 24 cylinders from B1, 76 cylinders from B2, and 32 cylinders from B3 were provided for the study.

Sample Preparation

The sample preparation commenced by removing the samples from their molds. This was done by systematically cutting the Styrofoam from the LCC cylinders into sections. The Styrofoam cutting was accomplished using a DemandTM Products, Inc. CutRite Hot Knife CRTM fitted with an eight inch blade. The samples were placed on a wire rack to air-dry for one day before further sample preparation and testing.

After the samples were allowed to air-dry for one day, the ends of the specimens were ground using a Kent USA SGS-608 surface grinder. The surface grinder was fitted with a trued diamond cup wheel and tooled with a hardened four-inch V-block mounted on a trued magnetic chuck. The V-block was subsequently squared to within 0.0002" over about four inches perpendicular to the grinding wheel. The specimens were indexed and placed on the V-block (lengthwise aligned with the V notch), and the end (cross-section) was surface ground until at least 95% cleanup was achieved. The specimens were then rotated and indexed 180 degrees end-to-end, and grinding was repeated. The end parallelism of each specimen was checked with a Fowler C-16 comparator. Measurements indicated 0.003", or less variation across the diameter of the specimens, which confirmed the quality of the grinding setup.

As testing progressed, it was observed that the bottom of the specimens exhibited a frothier texture than the rest of the sample (termed a "soft bottom"). The soft bottoms were, therefore, ground off from the specimens for subsequent testing by removing

approximately one-quarter to 3/8 of an inch from the bottom of the specimen during the grinding process.

The dimensions of the test specimen were measured to within 0.001" using a calibrated digital caliper and digital height gauge. The length of each specimen was measured at three different locations at approximately 120 degrees from one another using the digital height gauge, with the specimen standing vertically on a clean granite surface plate. The diameter of each test specimen was determined with a digital caliper in three locations (top quarter, middle, and bottom quarter) and approximately 120 degrees from one another. The mass of each specimen was determined to the nearest 0.01 gram using a calibrated AND FX-3000i digital scale. The representative specimen dimension was computed from the average measurement for each respective specimen.

Specific Gravity

The solids' specific gravity was determined in accordance with ASTM D854 (ASTM D18 Committee 2014). A total of 12 test specimens were prepared for specific gravity testing which were sampled from portions of destructed samples following completed unconfined compressive strength tests. The specimens were prepared for specific gravity testing by pulverizing the sub-samples in a mortar and pestle. The results of the specific gravity tests are summarized in Table 2, yielding an average of 2.671 with a standard deviation of 0.036. This average specific gravity was used for all subsequent specimen phase relationship computations.

Unit Weight and Phase Relationships

Standard geotechnical phase relationships were utilized to estimate the degree of saturation based on the unit weight determination, as described above, the specific gravity of the solids, and the water content. The water content was determined after previous destructive testing was performed in accordance with ASTM D2216 (ASTM D18 Committee 2019b). The water content, ω, is computed by,

$$\omega = \frac{m_w}{m_s} \quad (4)$$

where m_w is the mass of water loss upon drying and m_s is the mass of the dry solids. The total unit weight of the specimen, γ, is determined by,

$$\gamma = \frac{m \cdot g}{V} \quad (5)$$

where m is the specimen's total mass, g is the acceleration of gravity, and V is the volume of the specimen. The dry unit weight, γ_d, is determined by,

$$\gamma_d = \frac{\gamma}{1 + \omega} \quad (6)$$

The porosity, n, of the LCC is determined by,

$$n = 1 - \frac{\gamma_d}{G_s \cdot \gamma_w} \quad (7)$$

where γ_w is the unit weight of water (62.43 pcf) and G_s is the specific gravity of the solids. Finally, the degree of saturation, S, is calculated by,

$$S = \frac{\omega}{\left(\frac{\gamma_w}{\gamma_d}\right) - \left(\frac{1}{G_s}\right)} \quad (8)$$

As the hydration curing reaction advanced with time, LCC's dry unit weight also increased, as shown in Figure 3. The cured dry unit of the LCC had an average of 19.66

pcf with a minimum of 18.93 pcf, a maximum of 20.81 pcf, and a standard deviation of 0.3871 pcf. The cured porosity of the LCC used in this study had an average of 88.21% with a minimum of 87.52%, a maximum of 88.65%, and a standard deviation of 0.2321%.

CT Scanning and VSD Estimation

Three test specimens, B1-23, B1-24, and B3-24, with dry unit weights of 19.86 pcf, 20.01 pcf, and 19.86 pcf, respectively, were selected to undergo micro-computed tomography (CT) scans. The CT scans were performed to understand better the cellular void sizes, void-size distribution (VSD), and visual interpretation of the consistency of the samples. This scanning was also done to understand the distribution of pore water as a function of the degree of saturation. The CT scans were performed at the Surface Analysis Laboratory of the Utah Nanofab at the University of Utah. The instrument used to conduct the CT scans was a Zeiss Xradia 620 Versa 3D X-Ray Microscope/Nano-CT Scanner, shown in Figure 4.

Because the CT scanning machine operates at an elevated temperature and preservation of the degree of saturation was paramount to the study, the specimens must be sealed to prevent any water loss due to evaporation during the scanning process. A unique set of end caps was machined from polyethylene using a Grizzly G0570G metal lathe. The end caps were cut square and machined with an O-ring groove around the circumference. The O-ring groove allowed for a 0.012" thick latex membrane to be stretched over the specimens and sealed to the end caps with a rubber O-ring for the duration of the CT scans. A recess was machined in the bottom platen to fit and index on

the Zeiss Xradia 620 Versa specimen pedestal platen, as shown in Figure 5. After the CT scanning process was completed, the data were post-processed using Zeiss Reconstructor software by adjusting the center shift, beam hardening, and peak equalization across the specimen cross-section. Example images of the initial cross-sectional views of the CT scans are shown in Figure 6, Figure 7, and Figure 8. The post-processing resulted in cross-section image slices spaced about 0.003" lengthwise for a total length of about 3.106".

Images similar to those shown in Figure 6, Figure 7, and Figure 8 were selected for slices at the center of the specimens (image 0486) as well as 0.778" above and below the center of the specimens (i.e., images 0243 and 0729, respectively). The selected images were adjusted for contrast and inverted in preparation for further VSD analysis. The converted images were analyzed with WipFrag Fragmentation Analysis Software version 2.7.27, by WipWare.

The images were scaled and scanned with the WipFrag software, which typically identifies particles but, in this case, identifies voids in the image and computes and assigns a corresponding equivalent diameter of a sphere based on the 2-D cross-section. The void sizes were further analyzed resulting in a void size distribution, as summarized in Table 3, Table 4, and Table 5.

Table 6 summarizes a composite VSD that combines the results from the three analyses for each of the three specimens, providing an average estimated VSD of the LCC specimens. The VSD results are graphically displayed for intra-sample comparison in Figure 9, Figure 10, and Figure 11. Figure 12 shows the graphs of each merged data

for inter-sample comparison. Figure 13 illustrates the results for the average of nine merged VSDs for the LCC used in this study.

As shown in the VSD tables, the maximum void sphere size observed in the LCC specimens was less than 6.75 mm in diameter. As the nominal minimum specimen dimension is three inches (the diameter), this yields a minimum specimen dimension to the maximum void size ratio of about 11. Standard geotechnical testing practices suggest this ratio, comparing the maximum particle size, however, should be at least six and up to 10. The ratio of 11 satisfies the accepted testing criteria and the assumption that the largest void sphere sizes likely do not influence the test results.

Table 2. Summary of the specific gravity test results.
Specific gravity tests were performed on pulverized sub-samples of destructed test specimens used for unconfined compressive strength testing.

Sample No.	Specific Gravity
B1-01	2.715
B1-05	2.687
B1-10	2.633
B1-15	2.625
B1-18	2.671
B2-04	2.667
B2-09	2.654
B2-14	2.630
B3-03	2.737
B3-08	2.717
B3-13	2.657
B3-17	2.663

Table 3. Summary of the estimated VSD for sample B1-23.
VSD estimations were accomplished with the use of WipFrag software. The merged slices estimation is a sum of all the voids from the slices 0243, 0486, and 0729 for an average VSD of the specimen.

Void size	Percent finer			
(mm)	Slice 0243	Slice 0486	Slice 0729	Merged slices
6.75	100.00	100.00	100.00	100.00
4.50	99.14	100.00	100.00	99.71
3.00	97.90	98.48	96.76	97.71
2.00	86.05	83.92	79.81	83.24
1.30	40.76	39.08	33.78	37.86
0.90	11.41	10.60	8.47	10.15
0.60	3.49	3.01	2.42	2.97
0.40	1.27	1.07	0.89	1.08
0.25	0.34	0.28	0.27	0.30
0.17	0.19	0.15	0.17	0.17
0.12	0.13	0.11	0.13	0.12
0.08	0.09	0.08	0.10	0.09
0.05	0.02	0.02	0.02	0.02
0.03	0.00	0.00	0.00	0.00

Table 4. Summary of the estimated VSD for sample B1-24.
VSD estimations were accomplished with the use of WipFrag software. The merged slices estimation is a sum of all the voids from the slices 0243, 0486, and 0729 for an average VSD of the specimen.

Void size	Percent finer			
(mm)	Slice 0243	Slice 0486	Slice 0729	Merged slices
6.75	100.00	100.00	100.00	100.00
4.50	100.00	100.00	99.55	99.85
3.00	96.45	98.26	96.24	96.98
2.00	82.91	86.10	79.27	82.76
1.30	39.79	42.42	37.34	39.85
0.90	10.57	11.83	9.92	10.77
0.60	3.21	3.61	3.00	3.27
0.40	1.11	1.27	1.02	1.13
0.25	0.30	0.32	0.26	0.30
0.17	0.16	0.16	0.14	0.15
0.12	0.11	0.10	0.10	0.10
0.08	0.08	0.07	0.08	0.07
0.05	0.02	0.02	0.02	0.02
0.03	0.00	0.00	0.00	0.00

Table 5. Summary of the estimated VSD for sample B3-24.
VSD estimations were accomplished with the use of WipFrag software. The merged slices estimation is a sum of all the voids from the slices 0243, 0486, and 0729 for an average VSD of the specimen.

Void size	Percent finer			
(mm)	Slice 0243	Slice 0486	Slice 0729	Merged slices
6.75	100.00	100.00	100.00	100.00
4.50	100.00	100.00	99.53	99.84
3.00	96.41	93.25	94.53	94.73
2.00	81.74	74.59	77.40	77.90
1.30	49.24	43.28	45.43	45.98
0.90	16.85	14.85	15.08	15.60
0.60	4.06	3.46	4.03	3.85
0.40	1.40	1.18	1.42	1.33
0.25	0.42	0.36	0.41	0.40
0.17	0.22	0.20	0.20	0.21
0.12	0.15	0.14	0.13	0.14
0.08	0.10	0.10	0.10	0.10
0.05	0.03	0.03	0.03	0.03
0.03	0.00	0.00	0.00	0.00

Table 6. Summary of the combined estimated VSD for samples B1-23, B1-24, and B3-24.
VSD estimations were accomplished with the use of WipFrag software. The estimation is a sum of all the voids from the slices 0243, 0486, and 0729 for each of the three specimens resulting in an average VSD of the specimens.

Void size (mm)	Percent finer
6.75	100.00
4.50	99.85
3.00	95.48
2.00	79.53
1.30	43.94
0.90	13.99
0.60	3.66
0.40	1.27
0.25	0.36
0.17	0.19
0.12	0.13
0.08	0.09
0.05	0.03
0.03	0.00

Date: 26 May 2020
Sample ID: 20-600
Client: Dan Seely / University of Utah
Application: PhD Research for Impermeable LDCC and Permeable PLDCC
Target Density: 28 pcf (Actual = 27.7 pcf + 28.2 pcf + 28.6 pcf. **Avg. = 28.2 pcf**)
Target Strength: To Be Determined

Date	No.	Age	Density	load	Strength
02 Jun 2020	1	7 Days	23.1 pcf	756 lbs	107 pcf
	2	7 Days	23.1 pcf	747 lbs	106 pcf
				(Avg @ 7 days	= 106.5 pcf)
09 Jun 2020	3	14 Days	23.5 pcf	967 lbs	137 psi
	4	14 Days	23.7 pcf	1019 lbs	144 psi
				(Avg @ 14 days	= 140 psi)
23 Jun 2020	5	28 Days	22.8 pcf	1314 lbs	186 psi
	6	28 Days	22.7 pcf	1264 lbs	179 psi
				(Avg @ 28 days	= 182 psi)
21 Jul 2020	7	56 Days			
	8	56 Days			

Foam Density = 3.0 pcf ** Three batches were made and 35 Styrofoam molds, each with 4 cylinders, were filled.

	Log No.	Lab Batch Weight	Unit
Cement	Quikrete Type I/II	B1 = 25, B2 = 35 pcf, B3 = 30 **	Lbs
Fly ash	N/A	N/A	g.
Sand	N/A	N/A	g.
Water	0.50 w/c ratio	B1 = 12.5, B2 = 17.5, B3 = 15	Lbs.
Chemical	Mearlcrete	25	ml/L
Additive			
Base Density		114.5	pcf

Figure 2. Excerpt of the mix design report from Aerix Industries.

Mix design parameters and select strengths of the LCC cylinders retained by Aerix Industries.

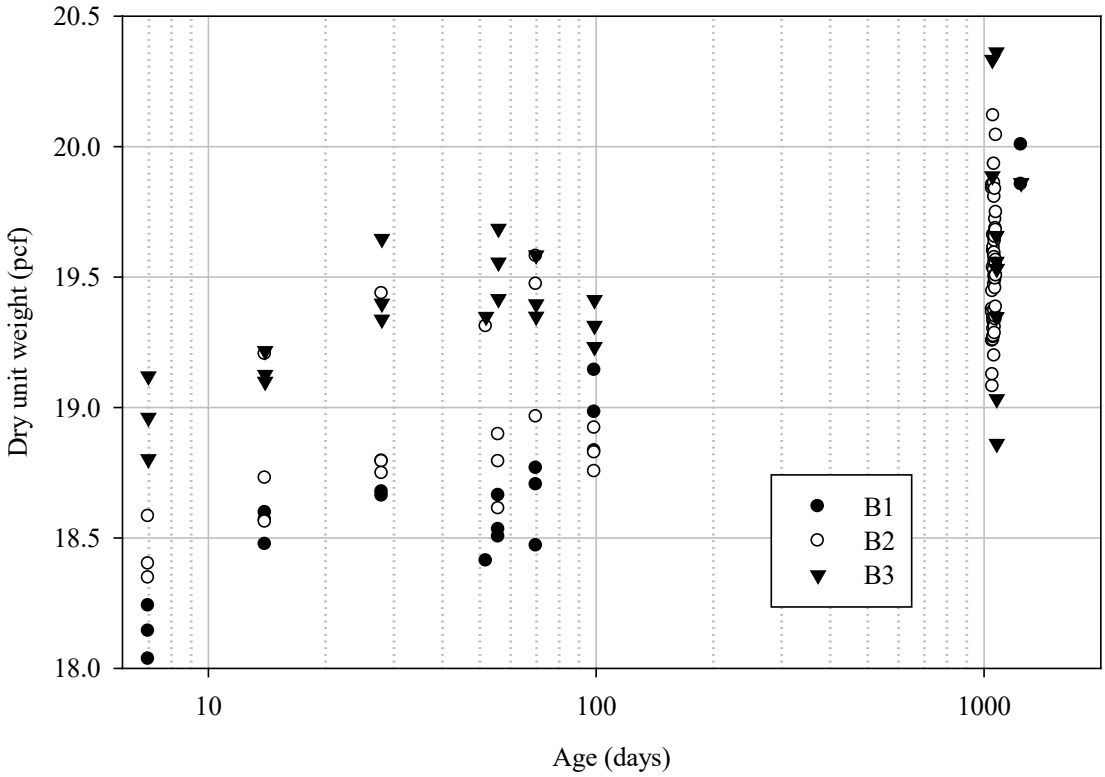

Figure 3. Dry unit weight for the LCC specimens as a function of time.

As the curing time and thus the hydration reaction of the LCC advances, the dry unit weight of the specimens increases. As shown in Chapter 6, the unconfined compressive strength follows a similar trend.

Figure 4. Photograph of the Zeiss Xradia 620 Versa.

The Xradia 620 Versa micro-CT scanner was used to scan three select test specimens at four levels of saturation. The data generated from the CT scans were used to estimate the VSD of the LCC.

Figure 5. Photograph of a test specimen prepared for CT scanning.

The photo shows the test specimen sealed in a latex membrane and O-rings mounted on the custom end caps to prevent any changes to the degree of saturation during the CT scan.

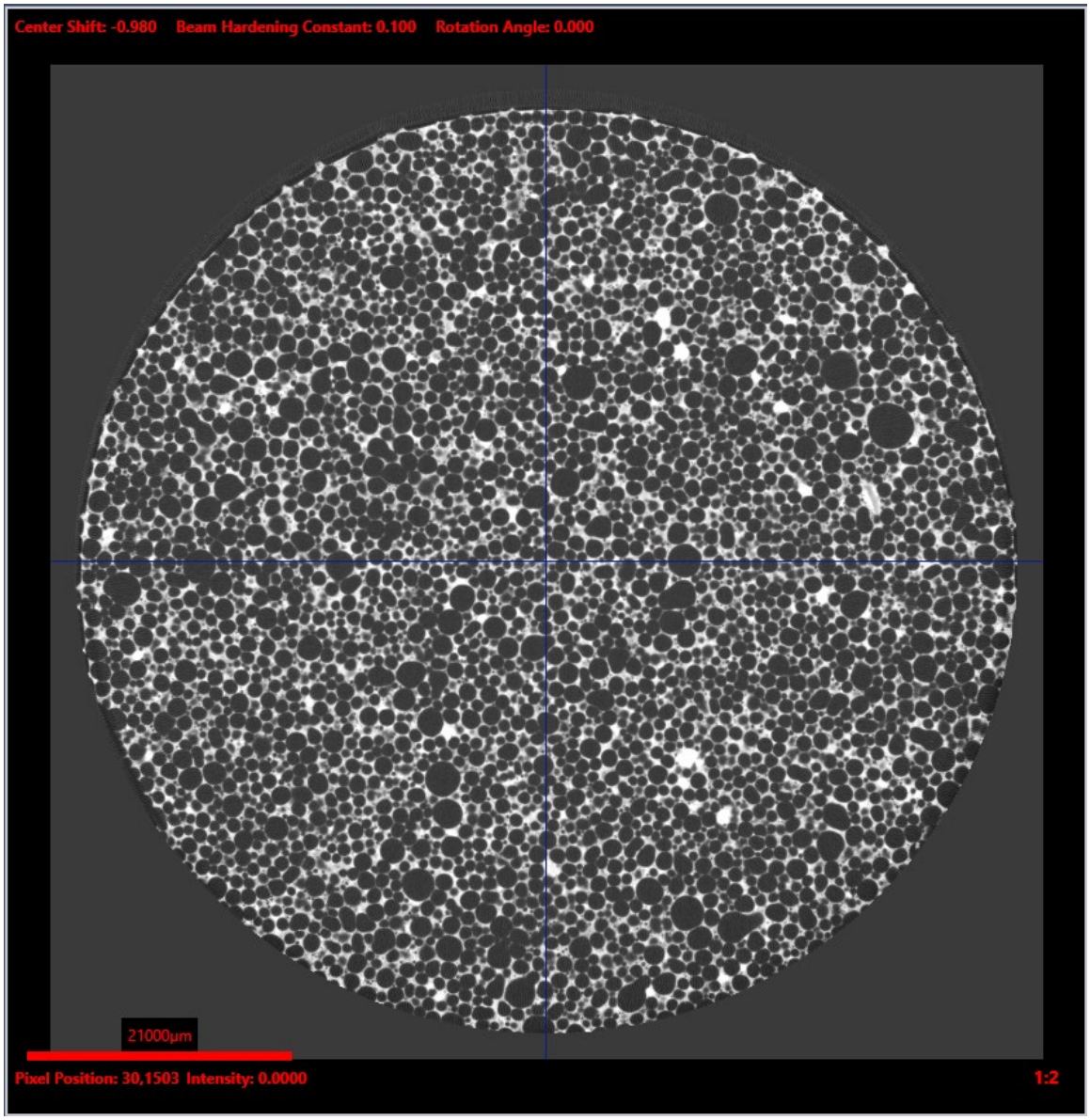

Figure 6. Initial view from the CT scan image reduction for sample B1-23.

Test specimen B1-23 CT image cross-section for the air-dried state. The dark spherical objects are the foamed air voids, and the light matrix is the concrete skeleton structure. The red scale bar in the lower left of the image is 21,000 µm.

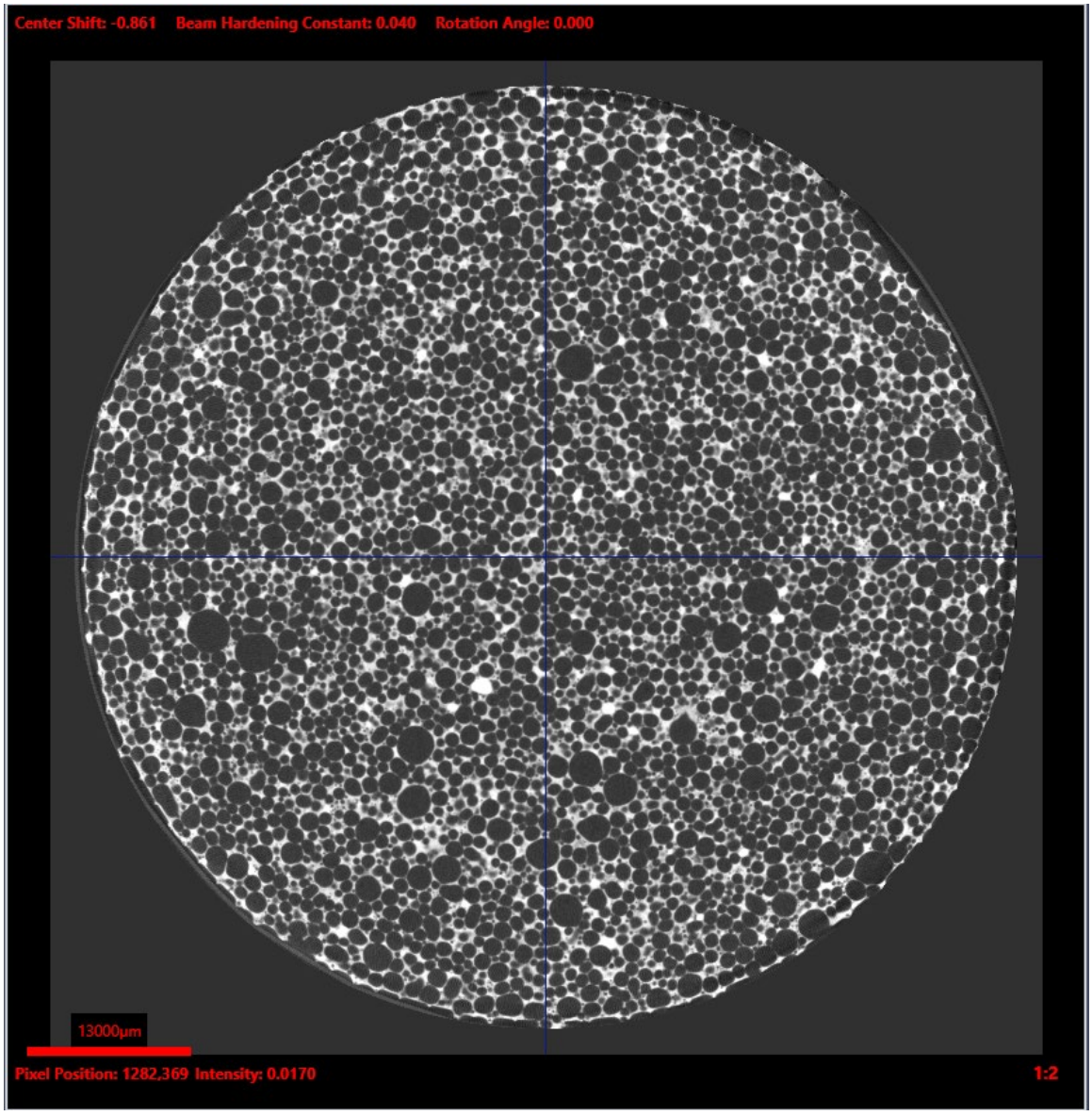

Figure 7. Initial view from the CT scan image reduction for sample B1-24.

Test specimen B1-24 CT image cross-section for the air-dried state. The dark spherical objects are the foamed air voids, and the light matrix is the concrete skeleton structure. The red scale bar in the lower left of the image is 13,000 µm.

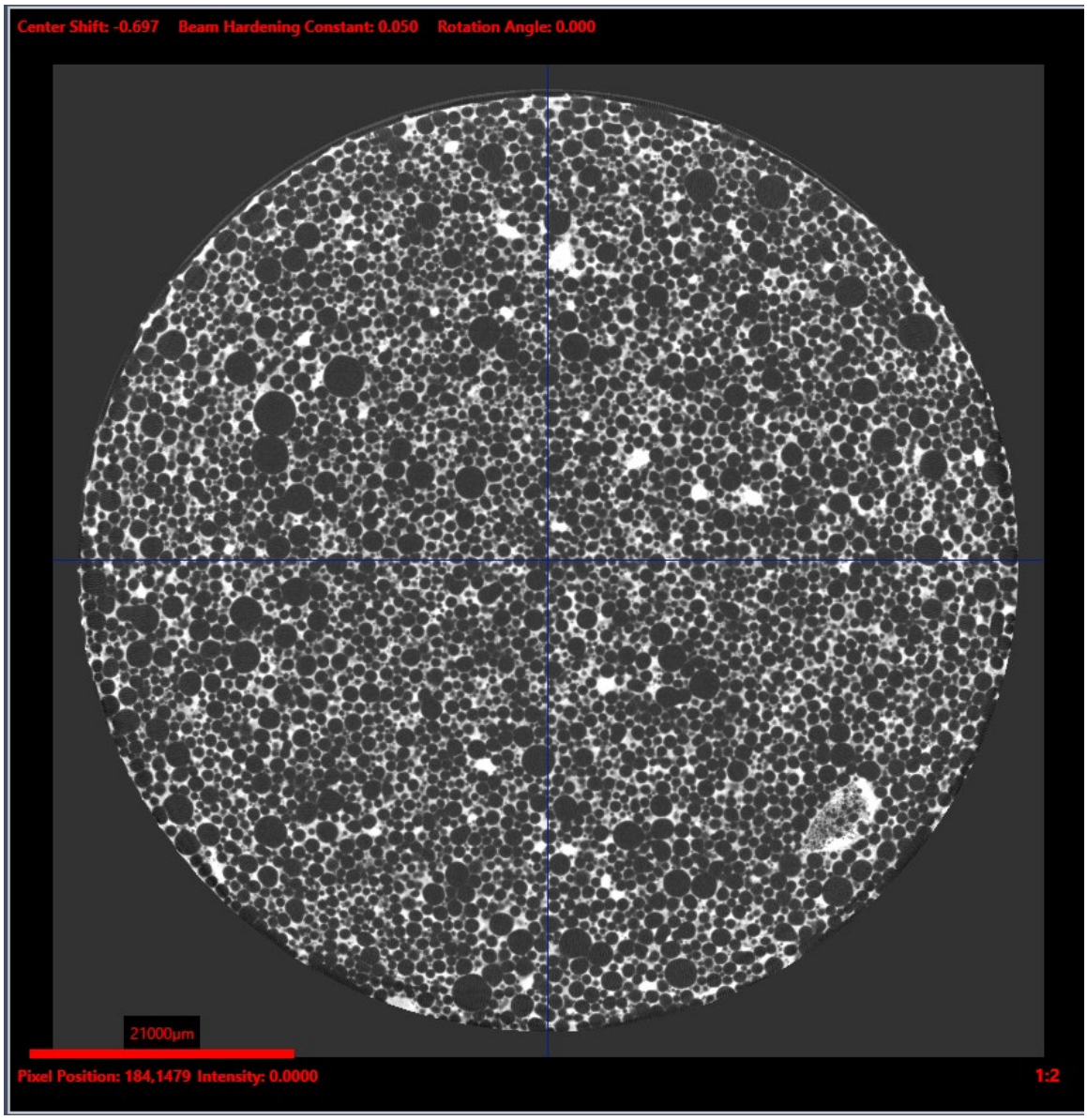

Figure 8. Initial view from the CT scan image reduction for sample B3-24.

Test specimen B3-24 CT image cross-section for the air-dried state. The dark spherical objects are the foamed air voids, and the light matrix is the concrete skeleton structure. The red scale bar in the lower left of the image is 21,000 mm.

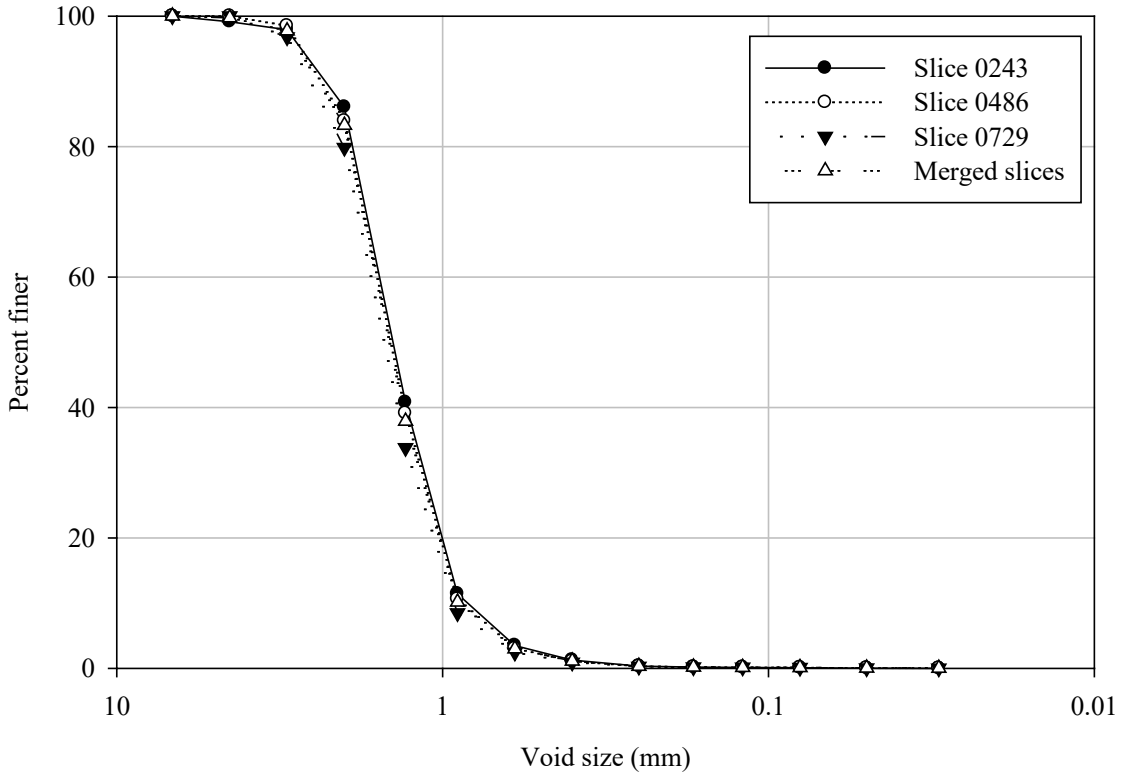

Figure 9. VSD estimations for Sample B1-23.

A comparison of the plots for the data shown in Table 3 which indicates a relatively small variance of the VSD within the sample.

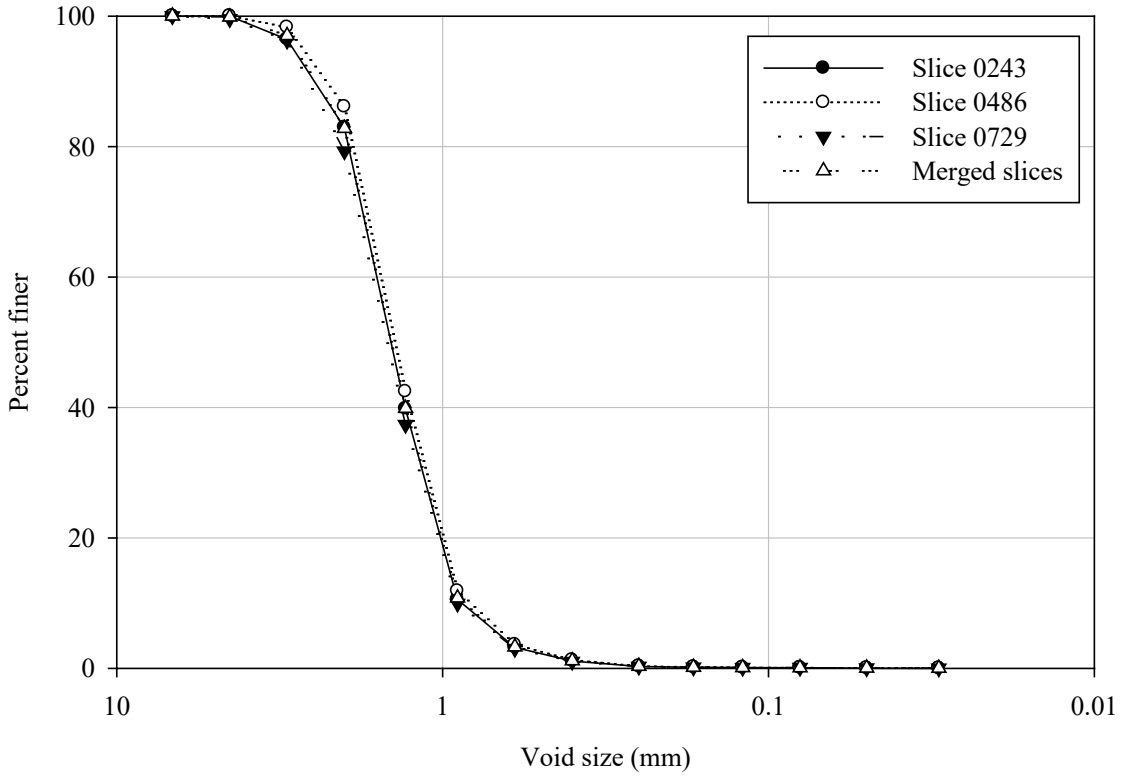

Figure 10. VSD estimations for Sample B1-24.

Comparison of the plots for the data shown in Table 4 which indicates a relatively small variance of the VSD within the sample.

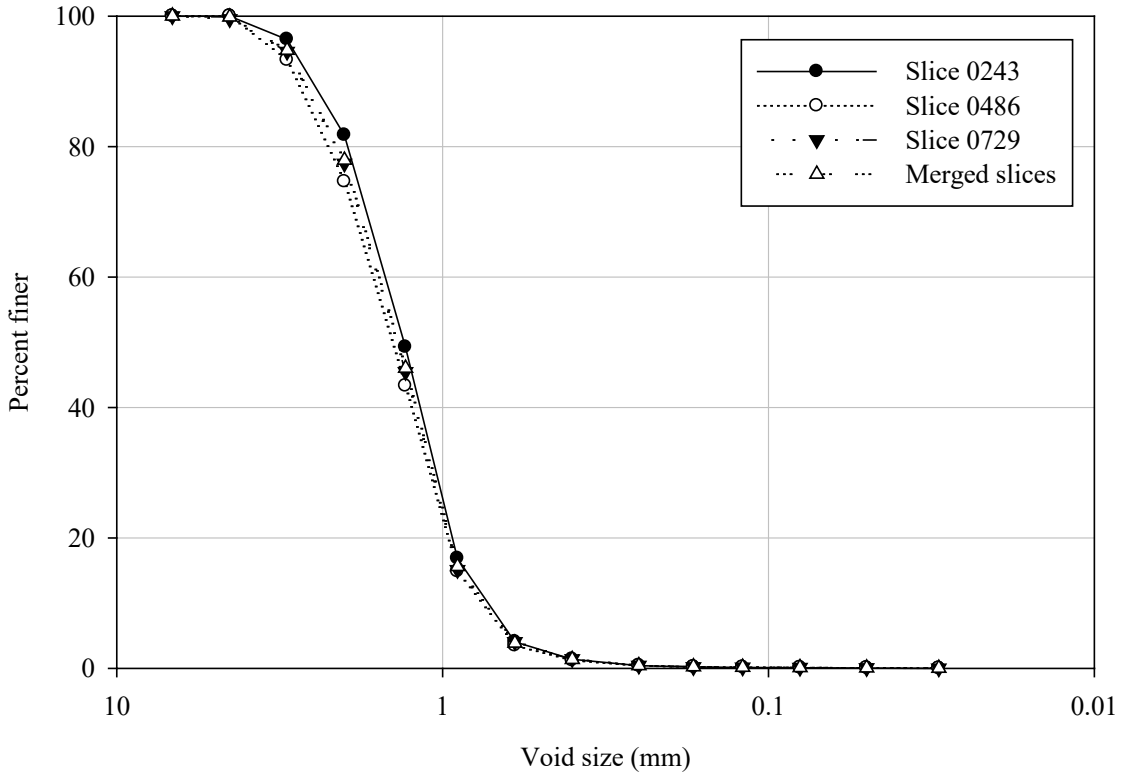

Figure 11. VSD estimations for Sample B3-24.

Comparison of the plots for the data shown in Table 5 which indicates a relatively small variance of the VSD within the sample.

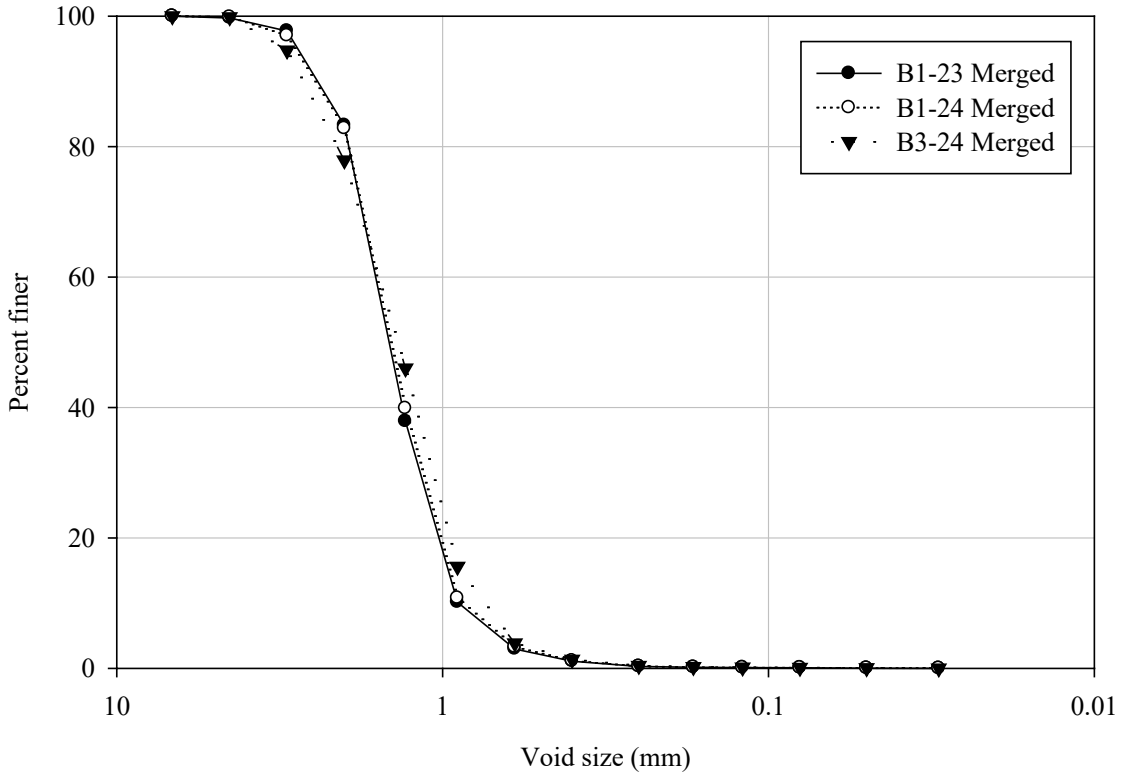

Figure 12. Merged respective VSD estimations for Samples B1-23, B1-24, and B3-24.

Comparison of the plots of each merged analysis from Table 3, Table 4, and Table 5 which indicates a slightly different VSD for sample B1-24.

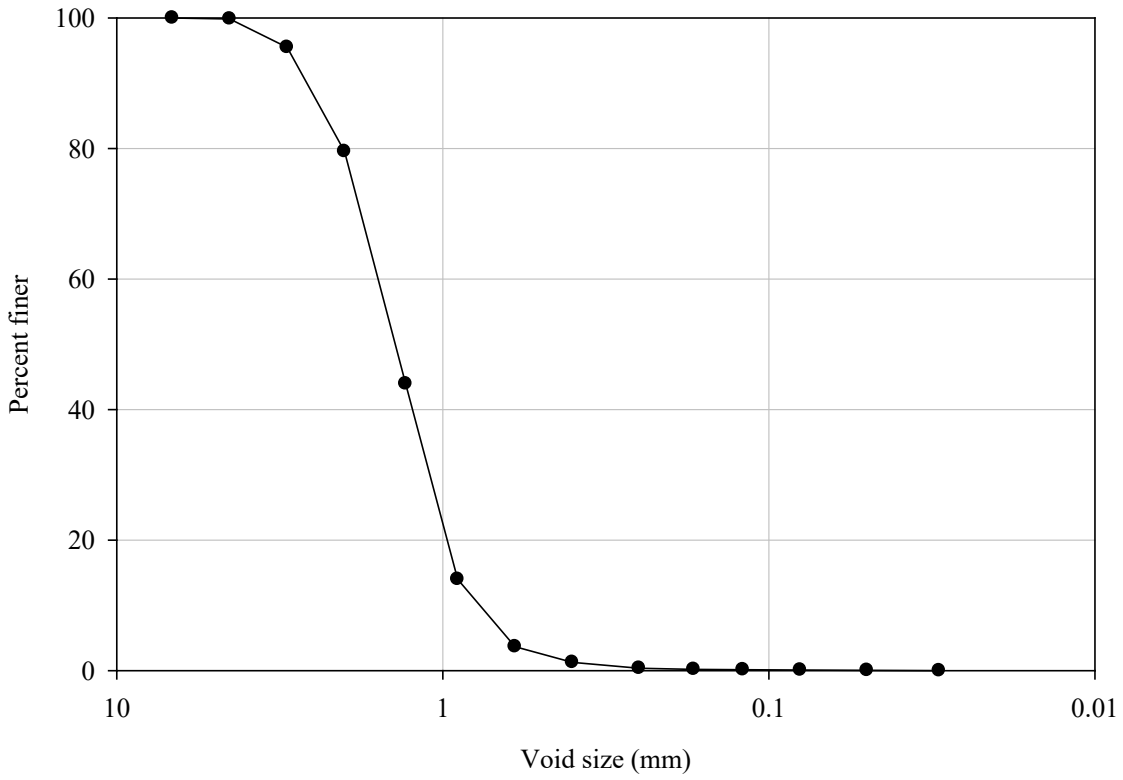

Figure 13. Combined VSD estimations for all WipFrag analyses.

Plot of the data shown which is the average VSD representing the nine VSD estimations for the LCC used in this study.

CHAPTER 3

PARTIALLY SATURATED STATES

A program was devised to produce a range of partially saturated LCC states that may be encountered under in-situ conditions. The program included five treatments (i.e., degrees of saturation, described below) for the LCC samples to investigate the effects of the degree of saturation on LCC's engineering behavior. After completing the treatments, mechanical testing was performed, including nondestructive RM testing, followed by either a UCS or CIDTx axial compression testing.

Partial Saturation Treatment Protocol

The treatments included groups identified as AD, H100, M5, D1, and W1, with each group having 12 specimens. All partially saturated treatment protocols were performed in a controlled laboratory environment, having an ambient temperature of about 72° F and an atmospheric pressure of about 12.6 psi. The AD (air-dried) treatment protocol exposed the samples to relatively low relative humidity (typically no more than 50%) for about 24 hours. The H100 treatment protocol exposed the samples to a 100% relative humidity environment for one week. The M5 treatment protocol started with submersion of the samples in water for 5 minutes and then allowing them to equalize by exposure to a 100% relative humidity environment for one week. The D1 treatment

protocol consisted of submersion of the samples in water for 24 hours and then allowing them to equalize by exposure to a 100% relative humidity environment for one week. Finally, the W1 treatment protocol consisted of submersion of the samples in water for one week and allowing them to equalize by exposure to a 100% relative humidity environment for one week. A summary of the resulting degrees of saturation for each of the treatments is shown in Table 7. The data in the table are the degrees of saturation, in percent, achieved from each treatment protocol described above.

Partial Saturation Treatment Statistics

The sample mean and population standard deviation for each treatment are shown in Table 8. Figure 14 shows histograms of the resulting saturations for each treatment, while Figure 15 shows a box plot of the saturation for each treatment. Several observations are noted from the results shown in these figures. The first observation is that the variance increases with the degree of saturation achieved for each treatment group. The second observation is that the AD, H100, and M5 treatments are easily distinguished as populations with differing saturation means. The third observation is that it is not apparent that treatments D1 and W1 have different sample means and variances. The following sections will further explore these hypotheses, and the supporting statistical evaluation is presented in Appendix A.

F-Test for Sample Variance

As shown in Figure 14 and Figure 15, it is evident that the variance increases with an increase in saturation resulting from the treatments. An initial *F*-test with a

significance level, $\alpha = 0.05$, is warranted to test for equal or unequal variance in the two data sets to decide to pursue a pooled-variance *t*-test or an independent variance *t*-test as appropriate. The null hypothesis for the *F*-test states there is no statistically significant difference between the variance of the two data sets. The alternative hypothesis for the *F*-test states that there is a statistically significant difference between the variance of the two data sets. The analysis resulted in an *F*-statistic for treatments in D1 and W1 are 1.885 and 0.308, respectively. The critical *F*-statistic was computed to be 2.818. Since the *F*-statistic for D1 is greater than the critical *F*-statistic, the null hypothesis is rejected, and the alternative hypothesis is accepted. Therefore, with 95% confidence, there is statistical evidence of a difference between the variance between the two data sets and an independent variance *t*-test is appropriate.

t-Test for Difference Between the Means

The widths of the histogram bars for each group in Figure 14 are scaled by bin size, which aids in comparing variance within the group. Treatments AD, H100, and M5 indicate a noticeable difference between the means. It is not apparent, however, that there is a difference between the means for groups D1 and W1.

A standard *t*-test with a significance level of $\alpha = 0.05$ was performed to evaluate if there was a significant difference between the means of the two data sets. The null hypothesis for the *t*-test states there is no statistically significant difference between the means of the two data sets. The alternative hypothesis is that there is a statistically significant difference between the means of the two data sets. In other words, the mean for W1 is statistically greater than D1, and the two means must be treated and evaluated

separately. The analysis resulted in a computed *t*-value test statistic of 3.749 with a weighted critical *t*-value of 2.201 for a single-tailed test (Figure 16). The null hypothesis is rejected because the test statistic *t*-value is greater than the critical *t*-value, and the alternative hypothesis is accepted (i.e., the means are statistically different). Therefore, with 95% confidence, there is statistical evidence that the mean of group W1 is greater than the mean of group D1. See also Appendix A.

Long-Term Saturation

Three test specimens, B3-30, B3-31, and B3-32, with corresponding dry unit weights of 19.03 pcf, 18.86 pcf, and 19.53 pcf, were selected for a long-term saturation test. The test aimed to understand the possible range of the degree of saturation that may be encountered in the field for LCC from ambient conditions below roadway grade as the LCC will likely absorb water after curing and then subsequently being buried. This absorption may be due to installation near the groundwater table where it may be subject to capillary action, exposure to free water from surrounding earthen materials, or subject to surface water infiltration through pavement sections or embankment fills. Each of the above scenarios resides in a high-humidity environment, which has been shown to promote partially-saturated flow through advection and diffusion (Seely et al. 2014).

The samples were cured, oven-dried, and subsequently subjected to a 100% relative humidity environment for 377 days. The mass of each specimen was determined about every 7 days for the test duration. The resulting change in saturation as a function of time is shown in Figure 17, with the corresponding increase in total unit weight being shown in Figure 18.

Nonlinear Regression Model

As observed in Figure 17, the degree of saturation rapidly increases when exposed to the high humidity environment, then tapers to a gradual asymptote. The data resembles both hyperbolic and exponential curves, which were further explored.

Nonlinear regressions were performed using SigmaPlot version 11.0.0.77. The nonlinear regression method assumes the population is normally distributed about the mean regression function, the variance of the dependent variable is constant, and the resulting residuals are independent of each other (i.e., not correlated). Several hyperbolic and exponential forms were regressed through an iterative process with a 95% confidence interval, $\alpha = 0.05$, that regression coefficients are statistically significant (i.e., are not zero). The form given in Equation 9 provided the best fit with satisfactory *p*-values. A *p*-value of 0.05 or greater signifies that the given regression coefficient has a 95% or greater probability of being non-zero.

$$S(\%) = a(1 - e^{-b \cdot x}) + c(1 - e^{-d \cdot x}) \qquad 9$$

Summaries of the regression results with the associated coefficients and *p*-values are found in Table 9. Plots of the fitted models from the regression for each test specimen are shown in Figure 19.

Based on the experimental data and reasonable extrapolation of the nonlinear regressions, we believe that under normal subsurface field conditions, LCC will have a minimum long-term degree of saturation of approximately 9.5%. Since LCC is often used as a lightweight fill for settlement mitigation, this total unit weight effect should be accounted for in the total stress calculations (i.e., $\Delta\sigma$ calculations) of the embankment fill.

CT Imaging of Partially Saturated LCC

As previously noted, computed tomography (CT) imaging was used to gain insight into pore water distribution at various degrees of saturation. The identical specimens discussed in Chapter 2, B1-23, B1-24, and B3-24, were subjected to the AD, M5, and D1 treatments and imaged with the Zeiss Xradia 620 Versa micro-CT scanner. The specimens were oven-dried after CT scanning before the subsequent saturation treatment was applied. One additional and final saturation treatment produced higher saturation than the W1 treatment. This extra treatment, V8, was performed by submersion of the specimens in water with a high-vacuum applied for about 8 hours. This treatment produced the highest degree of saturation of all the treatments in the study, averaging 30.2% saturation. The resulting degrees of saturation for the CT scan test program are summarized in Table 10. The CT scan images for the center of specimen B1-23 are shown in Figure 20, Figure 21, Figure 22, and Figure 23. The CT scan images for the center of specimen B1-24 are shown in Figure 24, Figure 25, Figure 26, and Figure 27. Finally, the CT scan images for the center of specimen B3-24 are shown in Figure 28, Figure 29, Figure 30, and Figure 31. Additional images for each specimen located 0.778" above and below the center of the specimen (image 0243 and 0729, respectively) are shown in Appendix B.

As seen in the images shown in Figure 20 through Figure 30, free water is not observable in the voids of the specimens for up to about 11% saturation. Free water was not observed in one specimen up to 16.4% while free water was observed in two of the specimens above 16.4% saturation. Free water was observed in all specimens above 25% saturation. We can conclude from these data that the pore water carrying capacity is

exceeded in the matrix and micropores around 16.4% saturation. For partially saturated states below 16.4%, the pore water is distributed through the matrix and micropores and is likely transported through advective matric suction gradients, osmotic suction, and diffusion.

Where free pore water is observable (above 16.4% saturation) the distribution of the water is observed to be randomly dispersed or clustered around large groups of voids. Viewing the CT slices in sequence allows one to gain insight into the pathways of the water in the specimen. The free water is rarely isolated and flow paths can be roughly traced from void to void. This observation gives a visualization of the mechanisms of fluid flow in the highly saturated or fully saturated state.

Table 7. Summary of the resulting degrees of saturation for each of the saturation treatments.

AD	H100	M5	D1	W1
2.955	4.449	11.907	15.986	17.531
3.091	4.441	9.783	15.504	18.374
3.067	4.275	10.281	15.480	20.368
3.122	4.227	9.679	15.802	19.438
3.620	4.981	10.444	17.123	18.652
3.716	4.647	10.055	17.533	16.078
3.541	4.967	9.884	15.493	15.842
3.455	4.996	9.860	15.764	17.084
3.449	5.033	9.889	17.973	18.536
3.329	5.100	9.389	15.708	18.283
4.014	5.288	9.142	15.832	17.781
3.825	5.112	9.293	17.547	18.503

Table 8. Saturation sample mean and population standard deviation for the treatments. The data listed in the table are the degrees of saturation, in percent, achieved from each of the treatment protocols described above.

Statistic	AD	H100	M5	D1	W1
Sample mean	3.432	4.793	9.967	16.312	18.039
Population standard deviation	0.317	0.349	0.069	0.900	1.235

Table 9. Summary of the nonlinear regression statistics for the long-term saturation model (Equation 9) for the data shown in Figure 19.

Model parameter	Regression value	*p*-value	*p*-value acceptance criterion
a	2.4682	<0.0001	$<\alpha$
b	0.5383	<0.0001	$<\alpha$
c	7.0226	<0.0001	$<\alpha$
d	0.0103	<0.0001	$<\alpha$
R^2	0.9976		
ANOVA		<0.0001	$<\alpha$
Normality		0.8971	$>\alpha$

Table 10. Summary of the resulting degrees of saturation, in percentage, of the specimens undergoing CT scans.

Specimen	AD	M5	D1	V8
B1-23	1.609	10.05	16.86	35.37
B1-24	1.773	9.99	16.35	24.67
B3-24	1.675	10.80	16.43	30.61

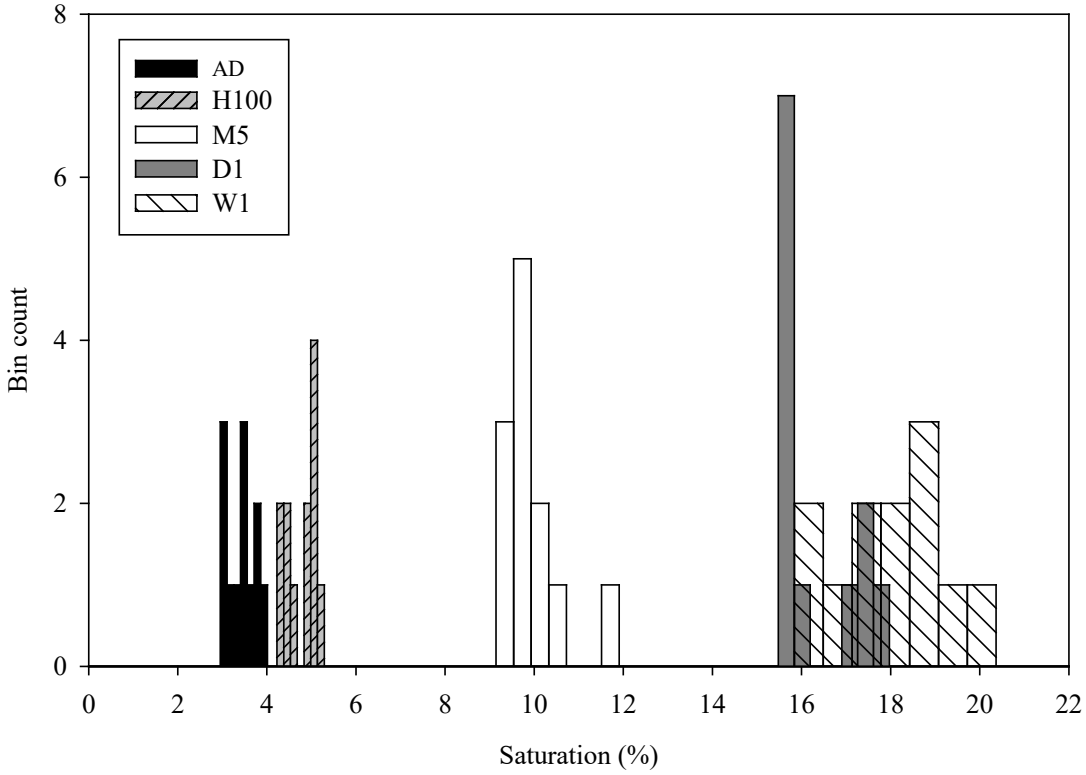

Figure 14. Histograms of the degrees of saturation resulting from each of the treatments.

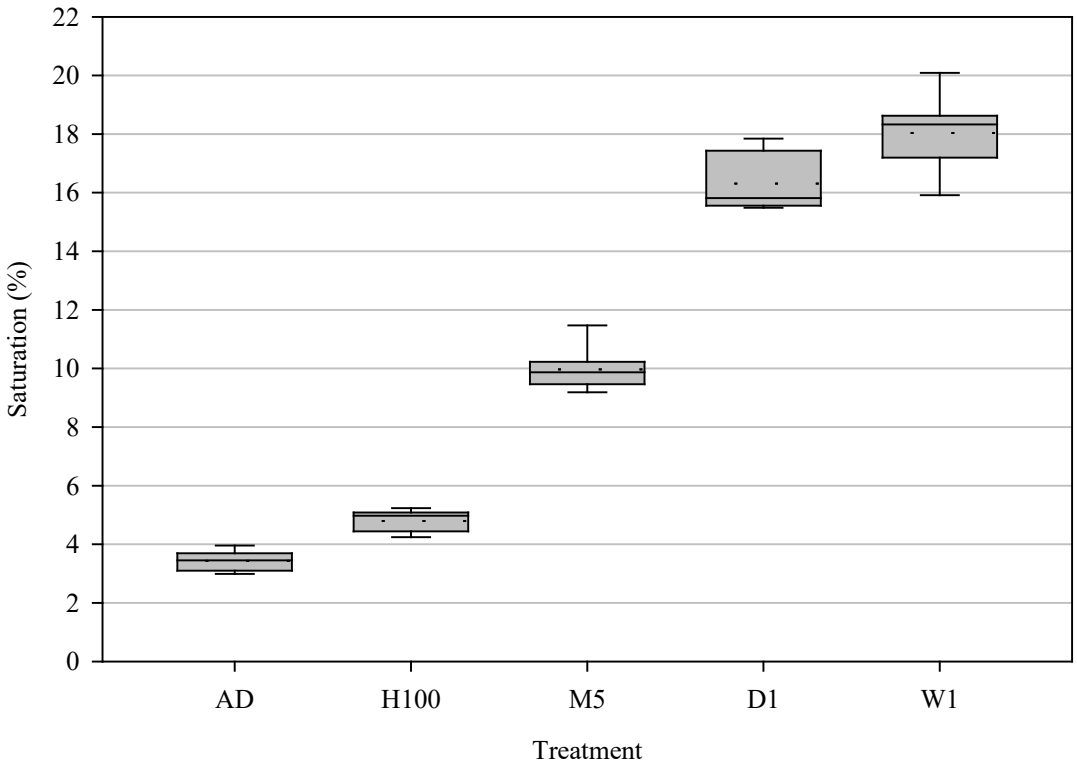

Figure 15. Box plot of the degrees of saturation resulting from each of the treatments.

The dashed line in each box represents the mean of the data set while the solid line within the box represents the median or 50th percentile of the data set. Treatments AD, H100, and M5 indicate an obvious difference between the means. It is not apparent, however, that there is a difference between the means for groups D1 and W1.

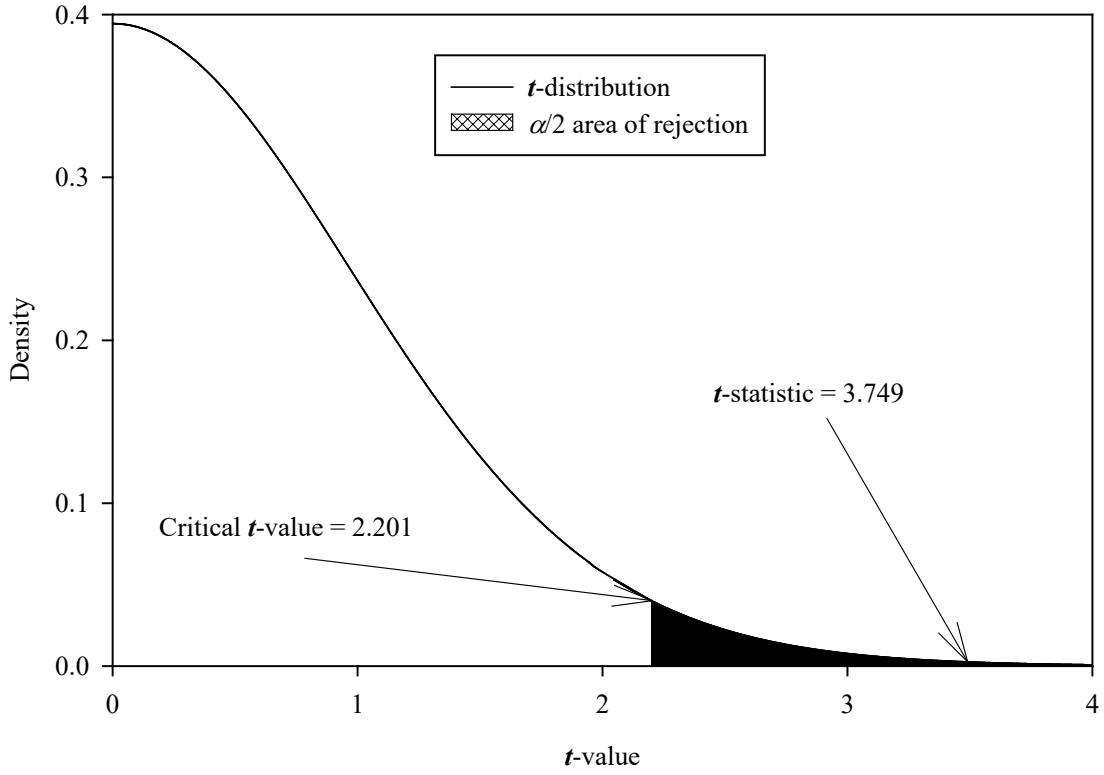

Figure 16. The ***t***-distribution with the ***t***-statistic and critical ***t***-value identified.

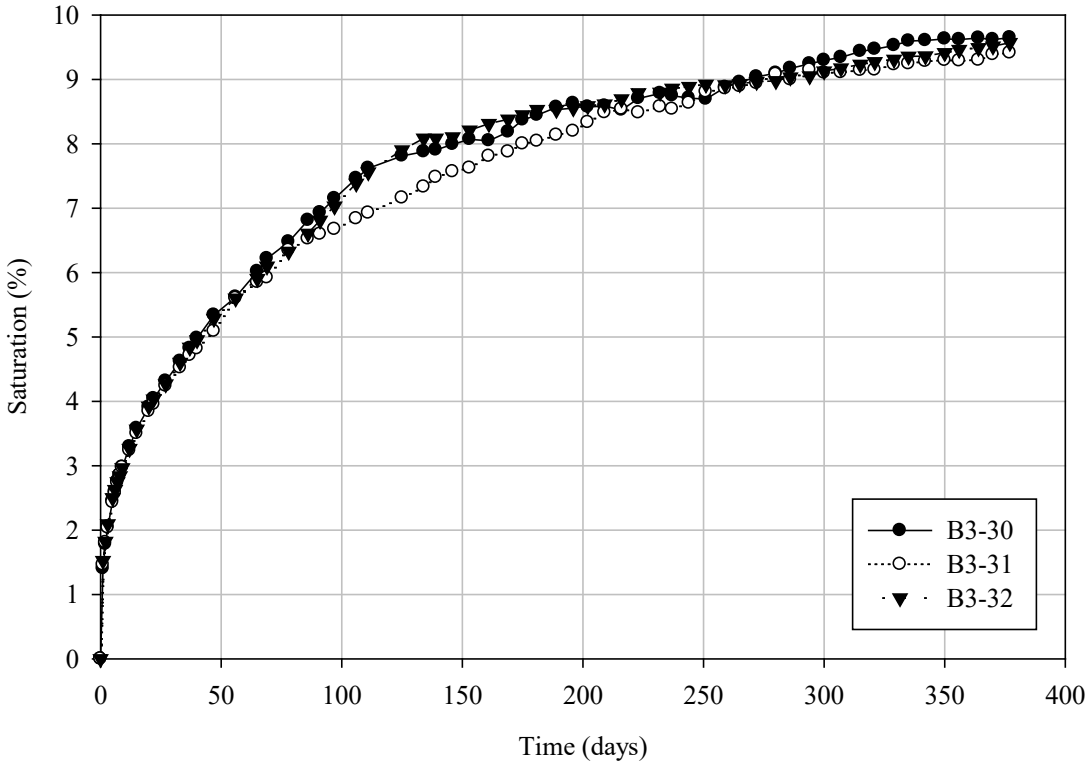

Figure 17. Saturation data as a function of time from the long-term saturation test.

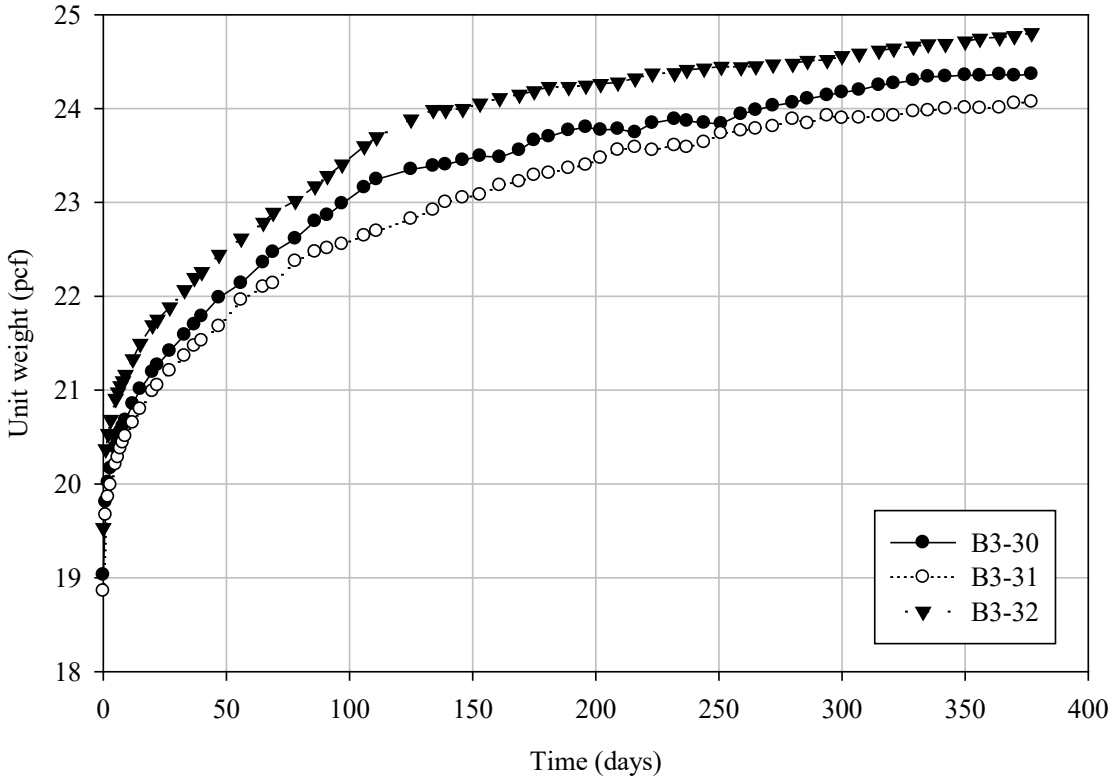

Figure 18. Total unit weight data as a function of time from the long-term saturation test.

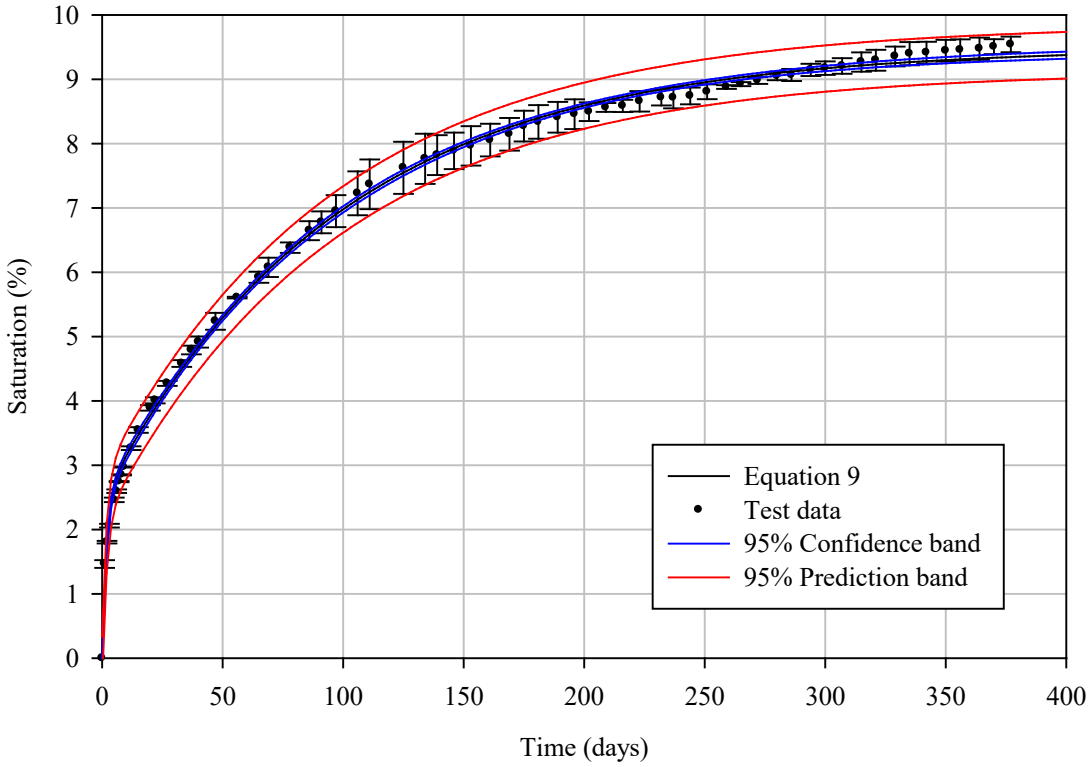

Figure 19. Long-term degree of saturation regression model (Equation 9) for B3-30, B3-31, and B3-32 with confidence and prediction bands.

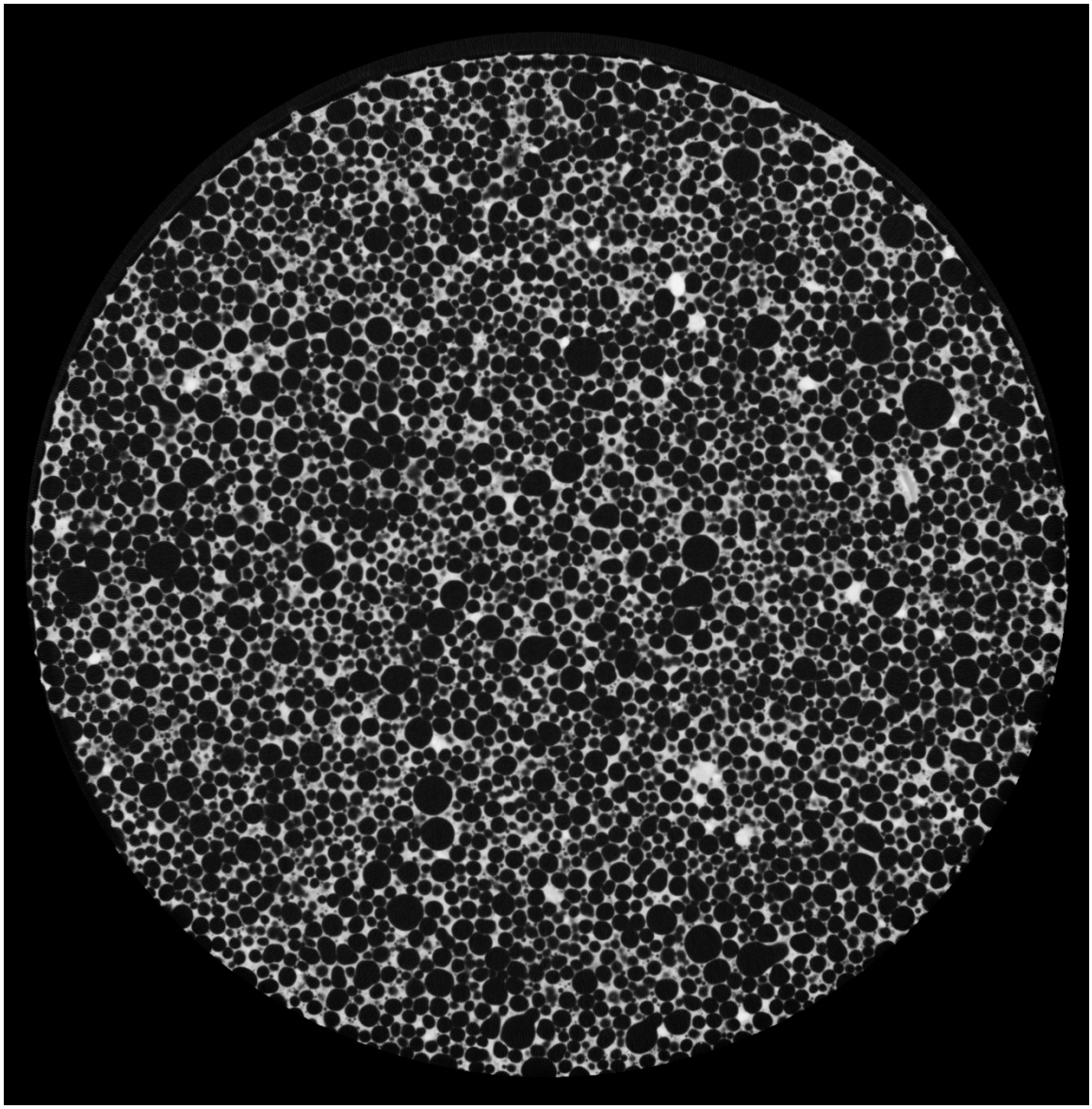

Figure 20. CT scan image of specimen B1-23 after the AD treatment.

B1-23 CT image cross-section for the air-dried state near the center of the specimen. The dark spherical objects are the foamed air voids with the light matrix being the concrete skeleton structure. The degree of saturation is 1.61%. No pore water is discernable from the image.

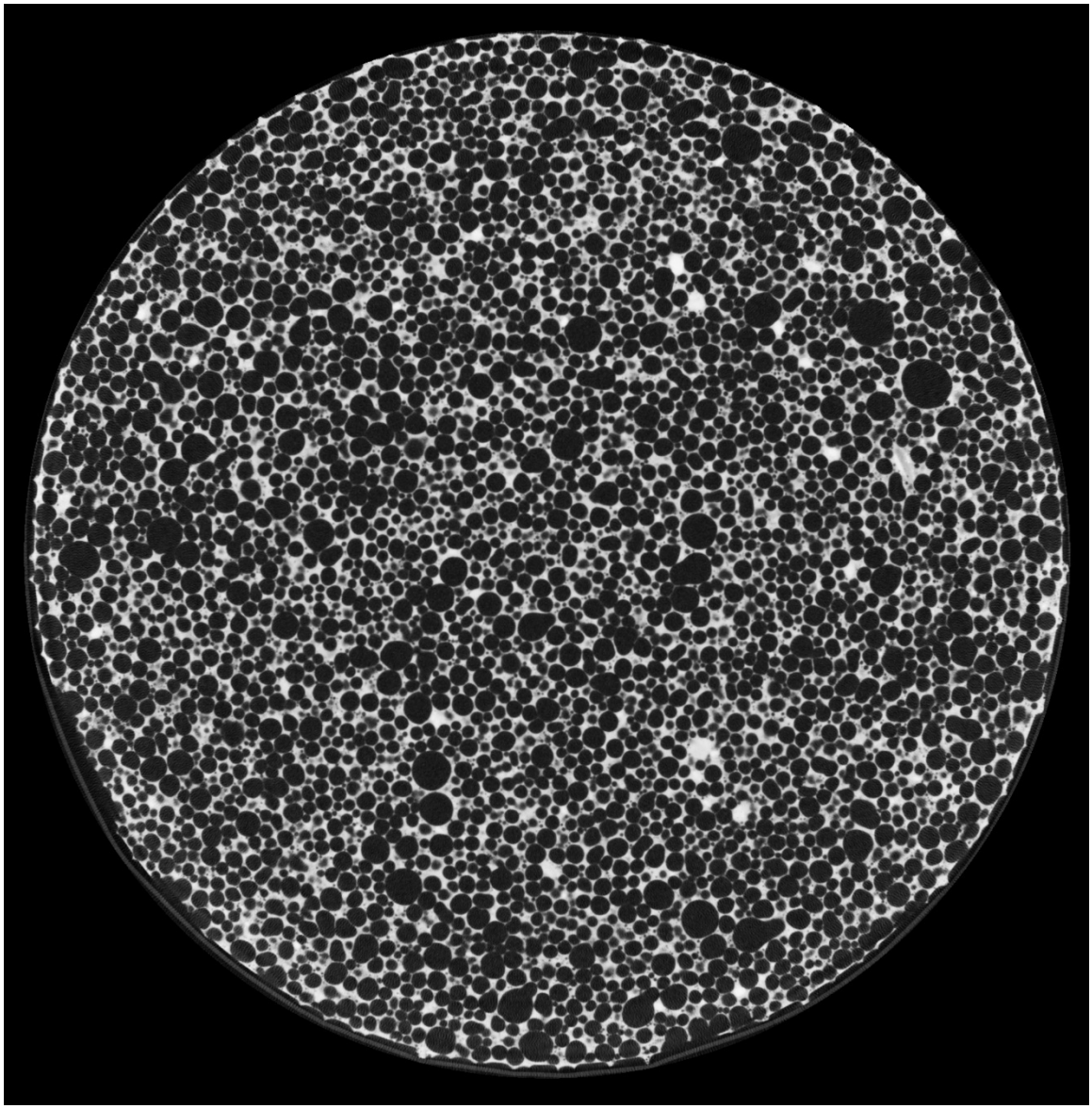

Figure 21. CT scan image of specimen B1-23 after the M5 treatment.

B1-23 CT image cross-section after the M5 treatment near the center of the specimen. The dark spherical objects are the foamed air voids with the light matrix being the concrete skeleton structure. The degree of saturation is 10.05%. No pore water is discernable from the image.

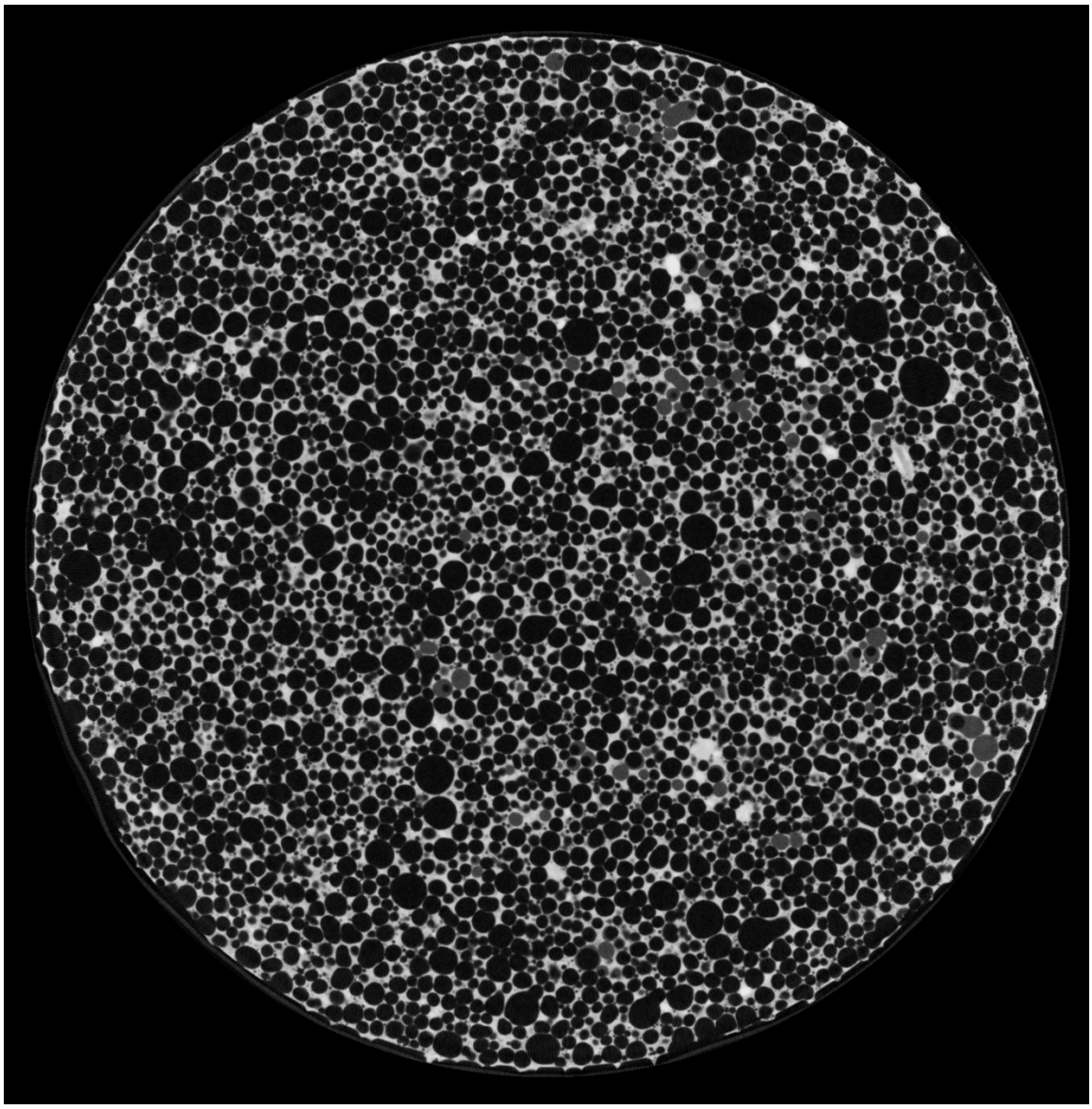

Figure 22. CT scan image of specimen B1-23 after the D1 treatment.

B1-23 CT image cross-section after the D1 treatment near the center of the specimen. The dark spherical objects are the foamed air voids with the light matrix being the concrete skeleton structure. The degree of saturation is 16.86%. Free pore water is visible in the image as grey spheres.

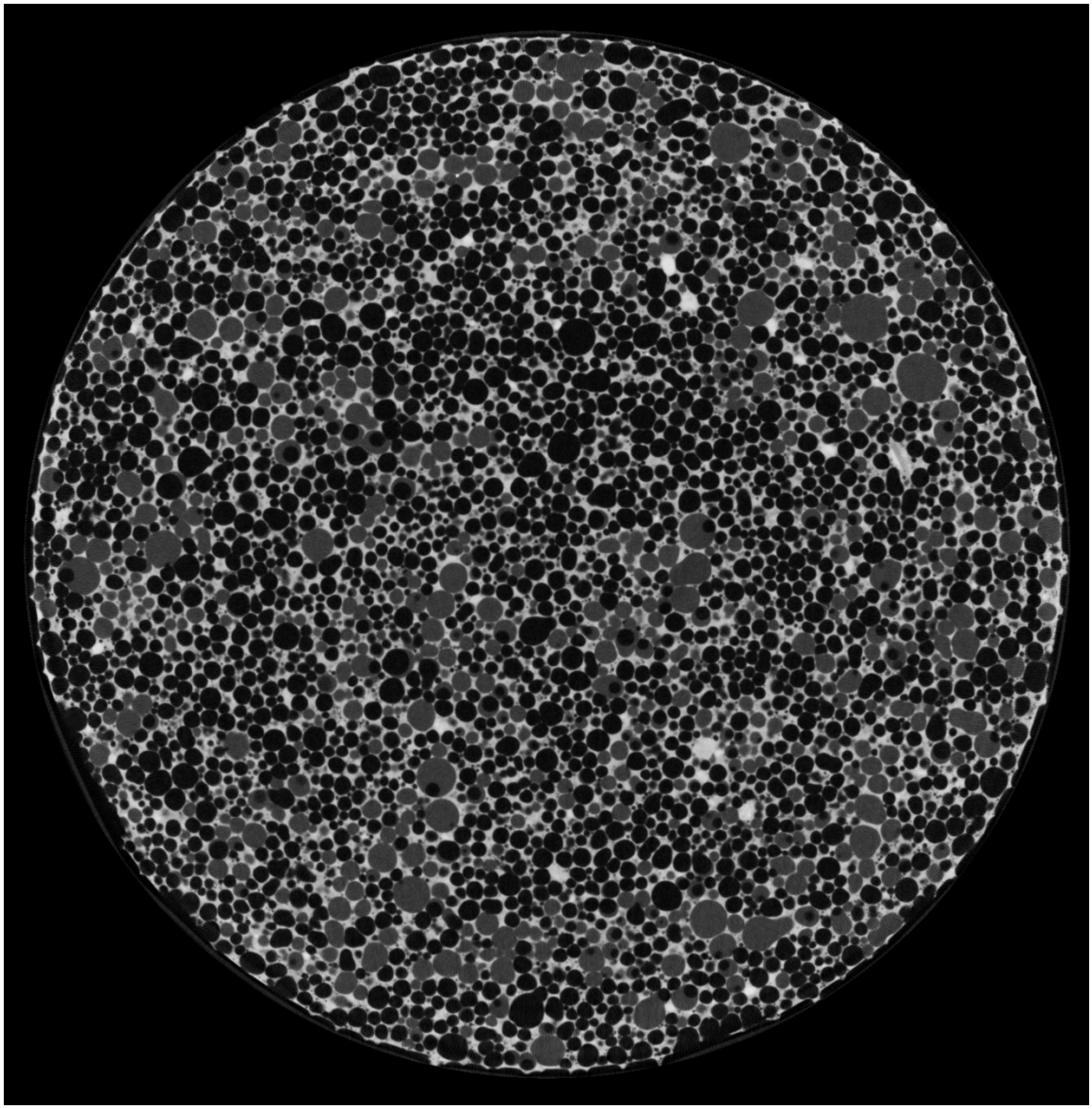

Figure 23. CT scan image of specimen B1-23 after the V8 treatment.

B1-23 CT image cross-section after the V8 treatment near the center of the specimen. The dark spherical objects are the foamed air voids with the light matrix being the concrete skeleton structure. The degree of saturation is 35.37%. Free pore water is visible in the image as grey spheres.

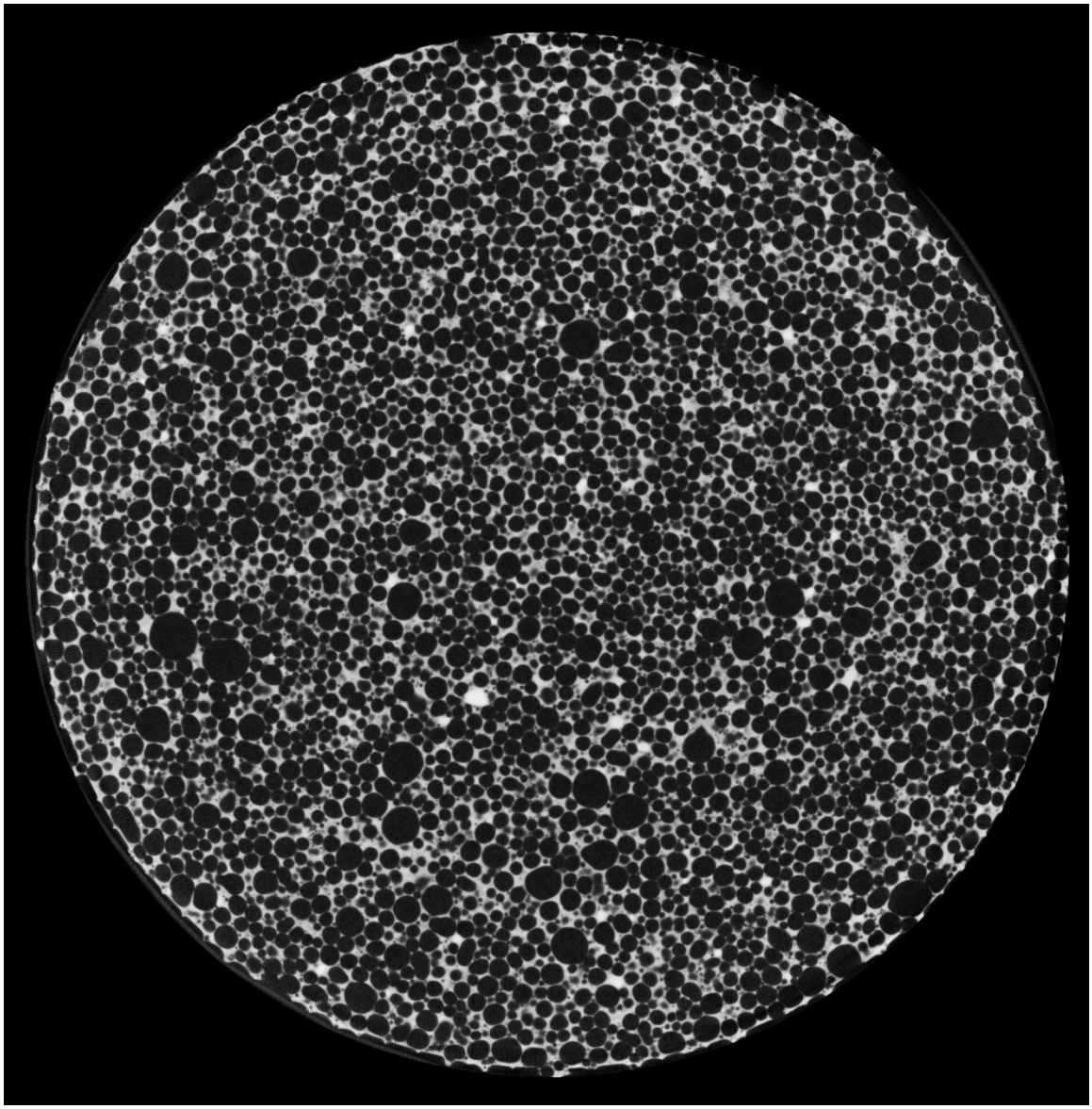

Figure 24. CT scan image of specimen B1-24 after the AD treatment.

B1-24 CT image cross-section for the air-dried state near the center of the specimen. The dark spherical objects are the foamed air voids with the light matrix being the concrete skeleton structure. The degree of saturation is 1.77%. No pore water is discernable from the image.

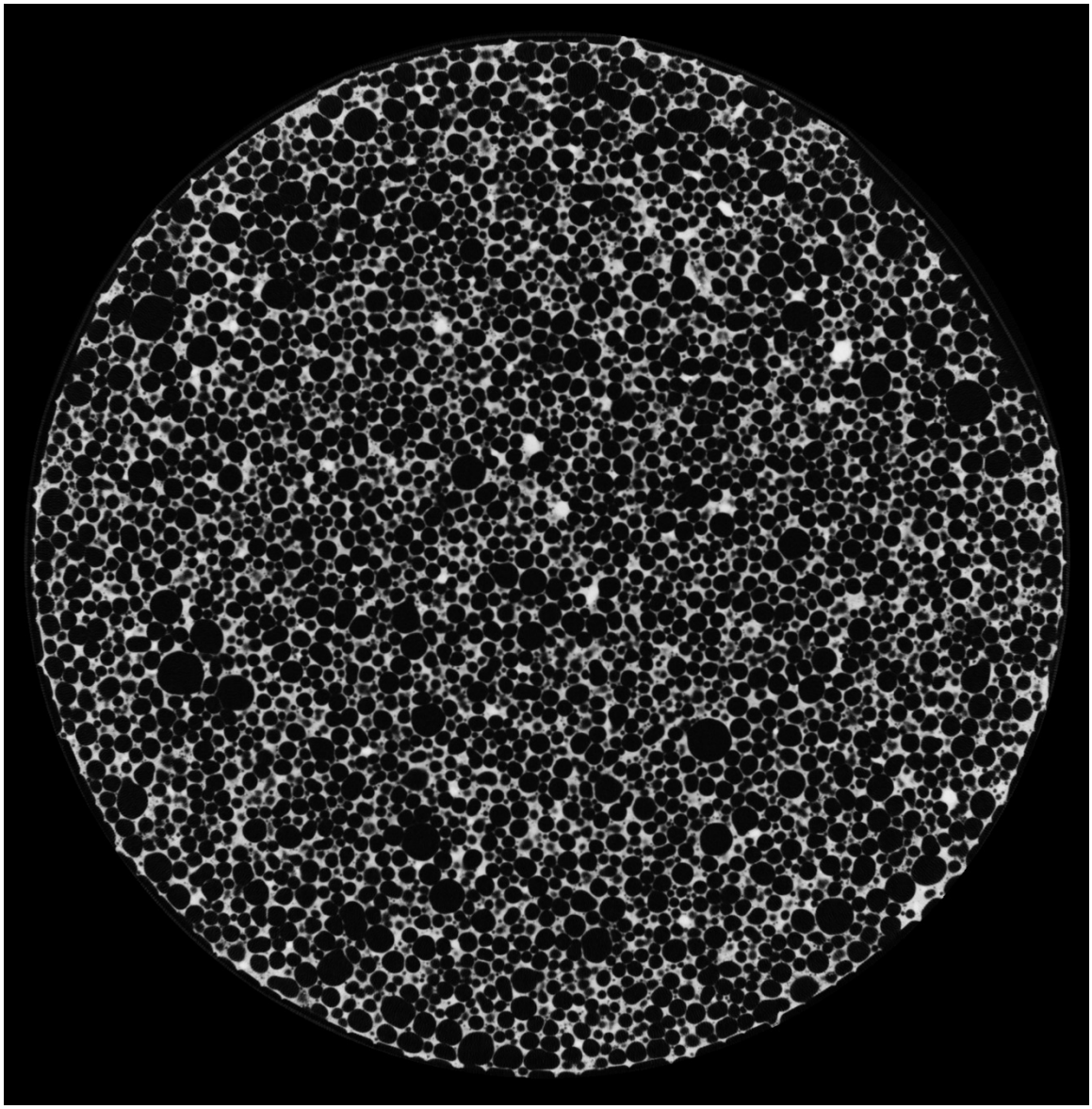

Figure 25. CT scan image of specimen B1-24 after the M5 treatment.

B1-24 CT image cross-section after the M5 treatment near the center of the specimen. The dark spherical objects are the foamed air voids with the light matrix being the concrete skeleton structure. The degree of saturation is 9.99%. No pore water is discernable from the image.

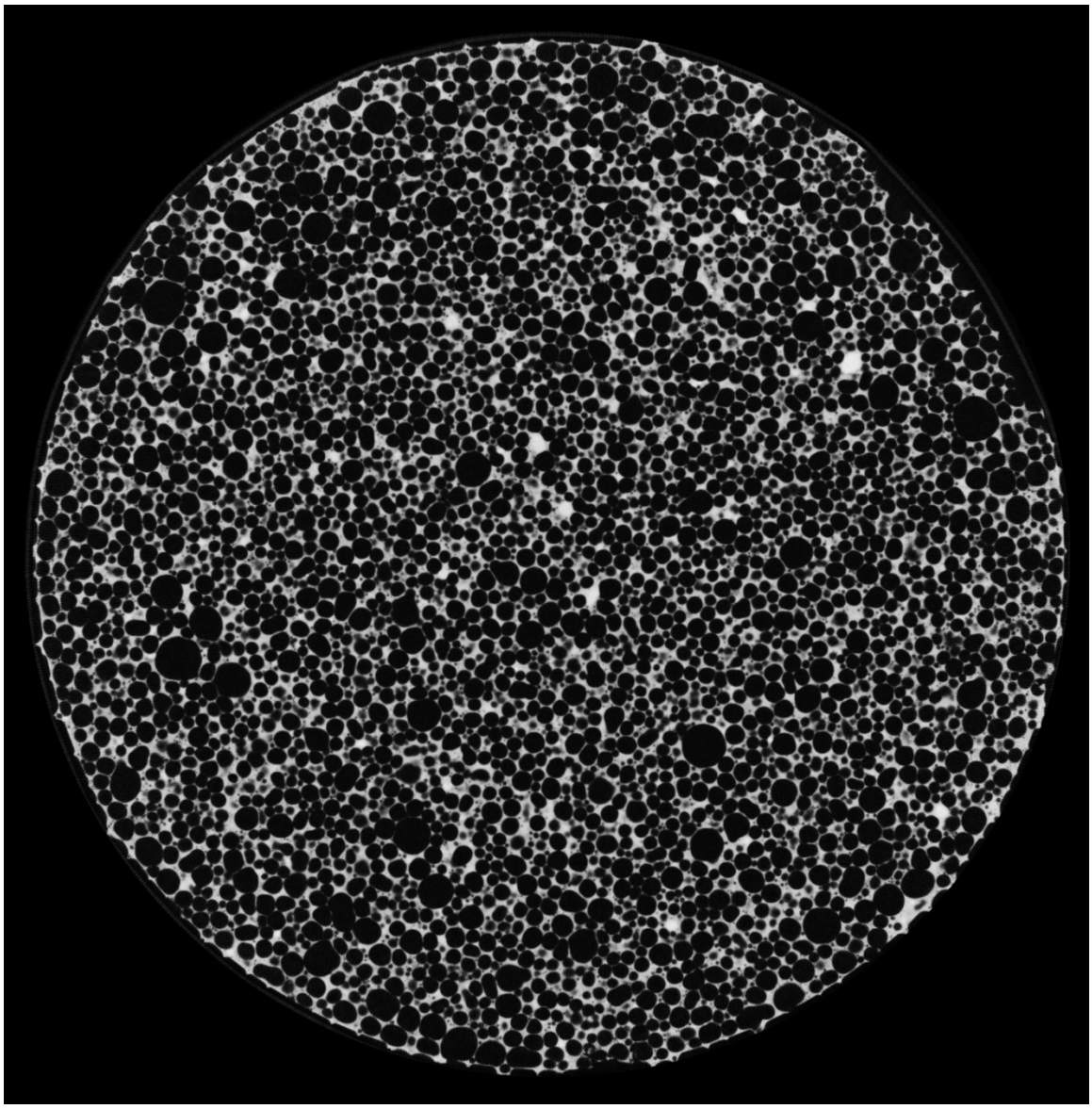

Figure 26. CT scan image of specimen B1-24 after the D1 treatment.

B1-24 CT image cross-section after the D1 treatment near the center of the specimen. The dark spherical objects are the foamed air voids with the light matrix being the concrete skeleton structure. The degree of saturation is 16.35%. No pore water is discernable from the image.

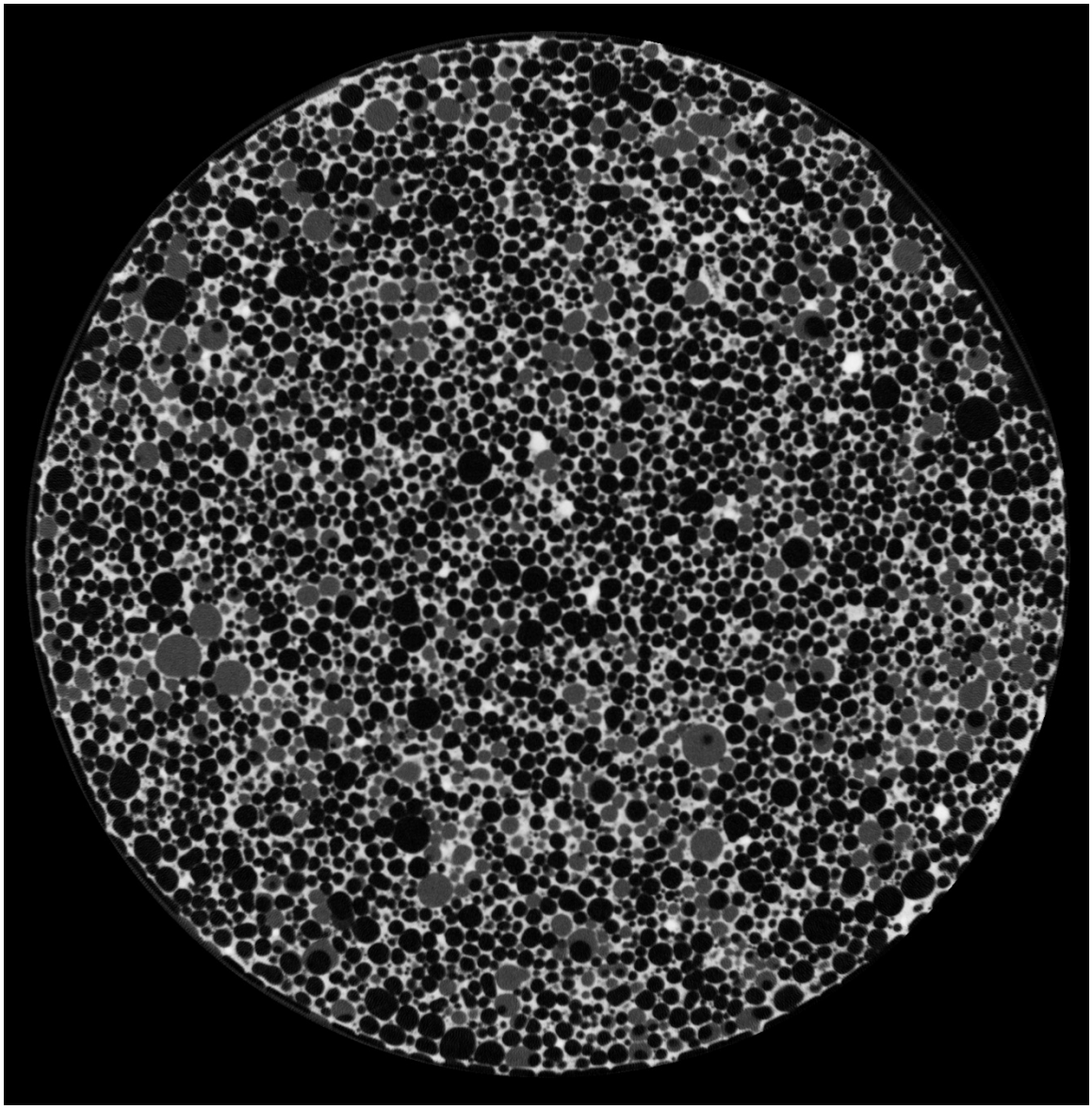

Figure 27. CT scan image of specimen B1-24 after the V8 treatment.

B1-24 CT image cross-section after the V8 treatment near the center of the specimen. The dark spherical objects are the foamed air voids with the light matrix being the concrete skeleton structure. The degree of saturation is 24.67%. Free pore water is visible in the image as grey spheres.

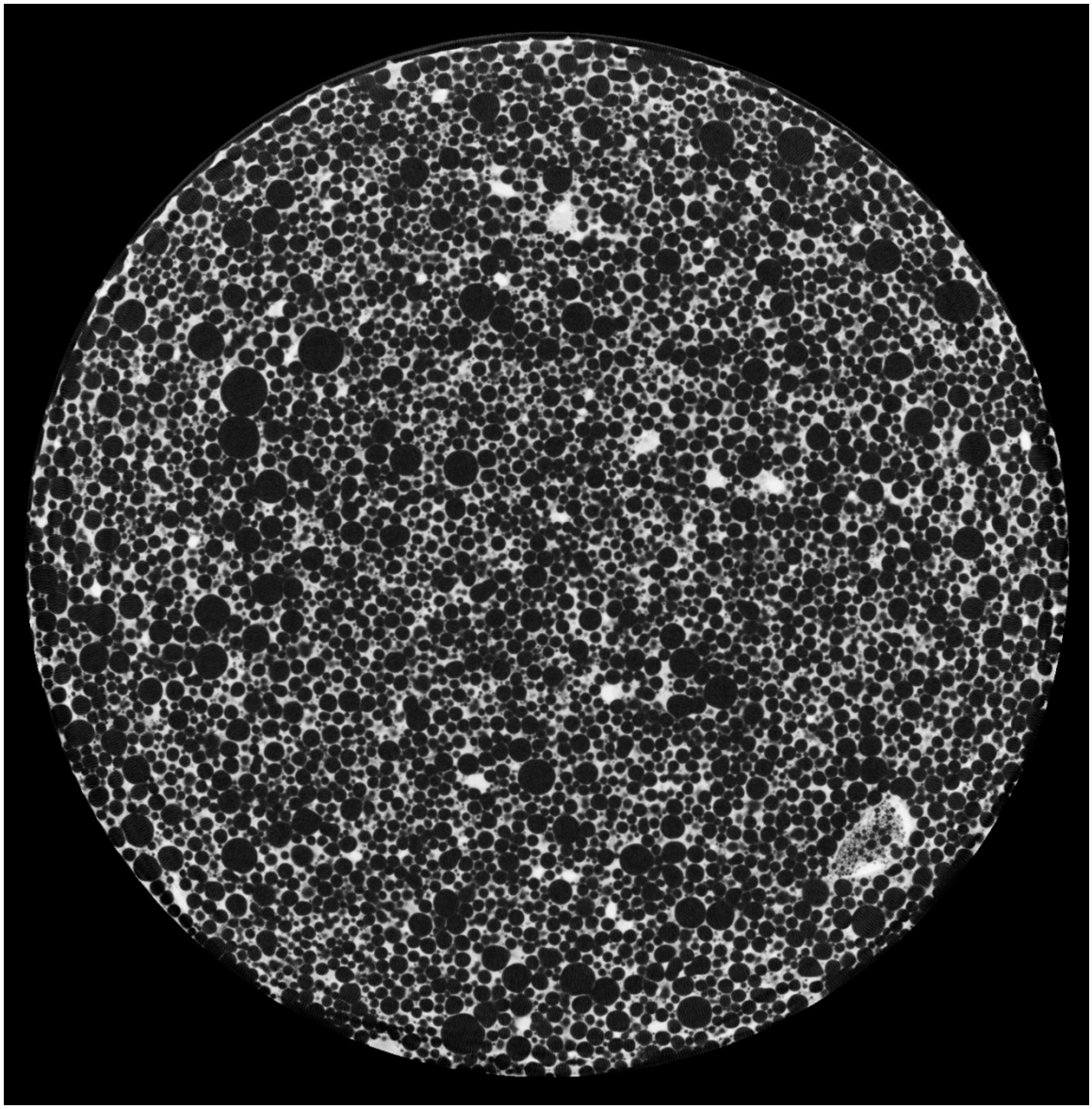

Figure 28. CT scan image of specimen B3-24 after the AD treatment.

B3-24 CT image cross-section for the air-dried state near the center of the specimen. The dark spherical objects are the foamed air voids with the light matrix being the concrete skeleton structure. The degree of saturation is 1.67%. No pore water is discernable from the image.

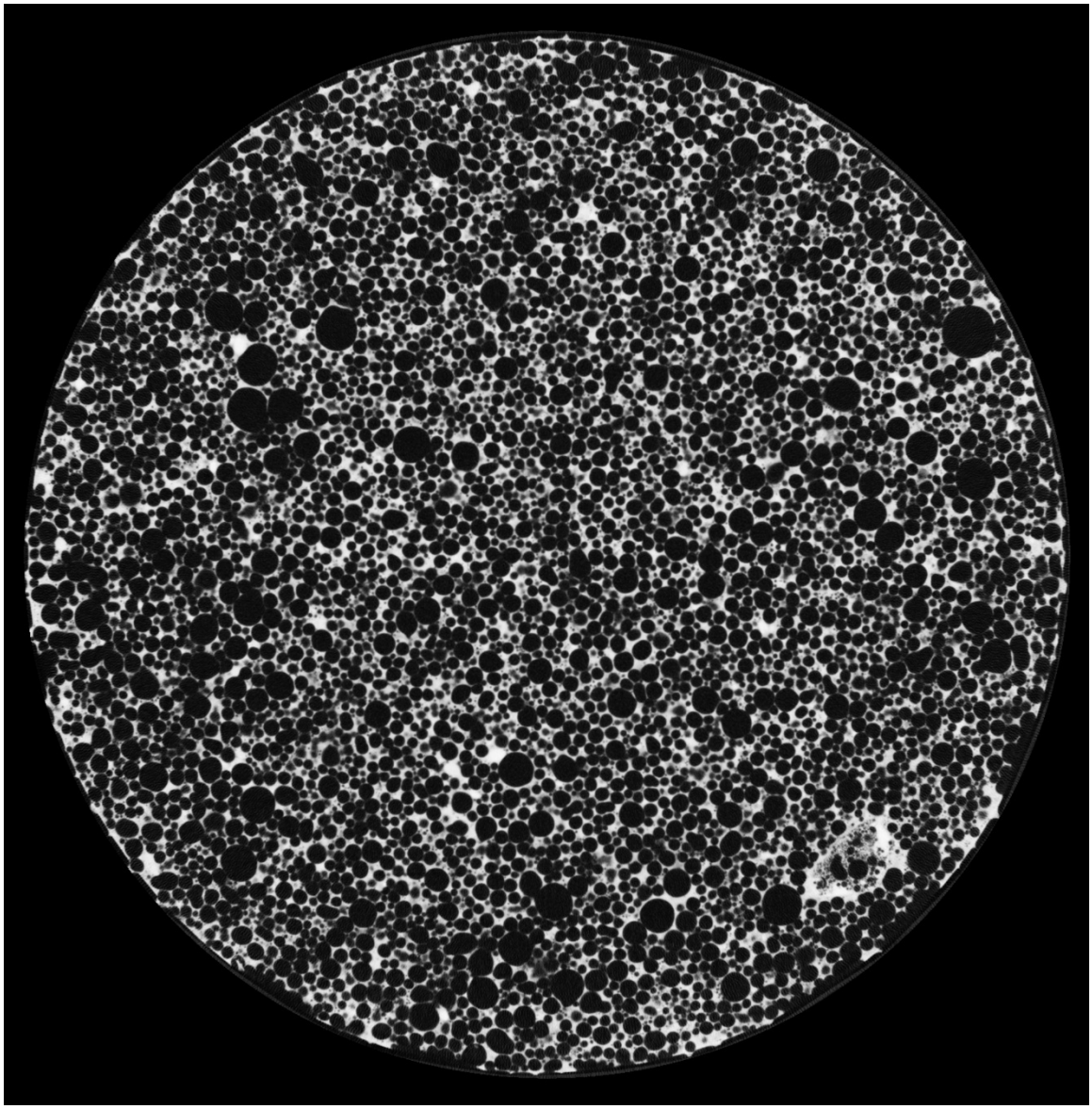

Figure 29. CT scan image of specimen B3-24 after the M5 treatment.

B3-24 CT image cross-section after the M5 treatment near the center of the specimen. The dark spherical objects are the foamed air voids with the light matrix being the concrete skeleton structure. The degree of saturation is 10.80%. No pore water is discernable from the image.

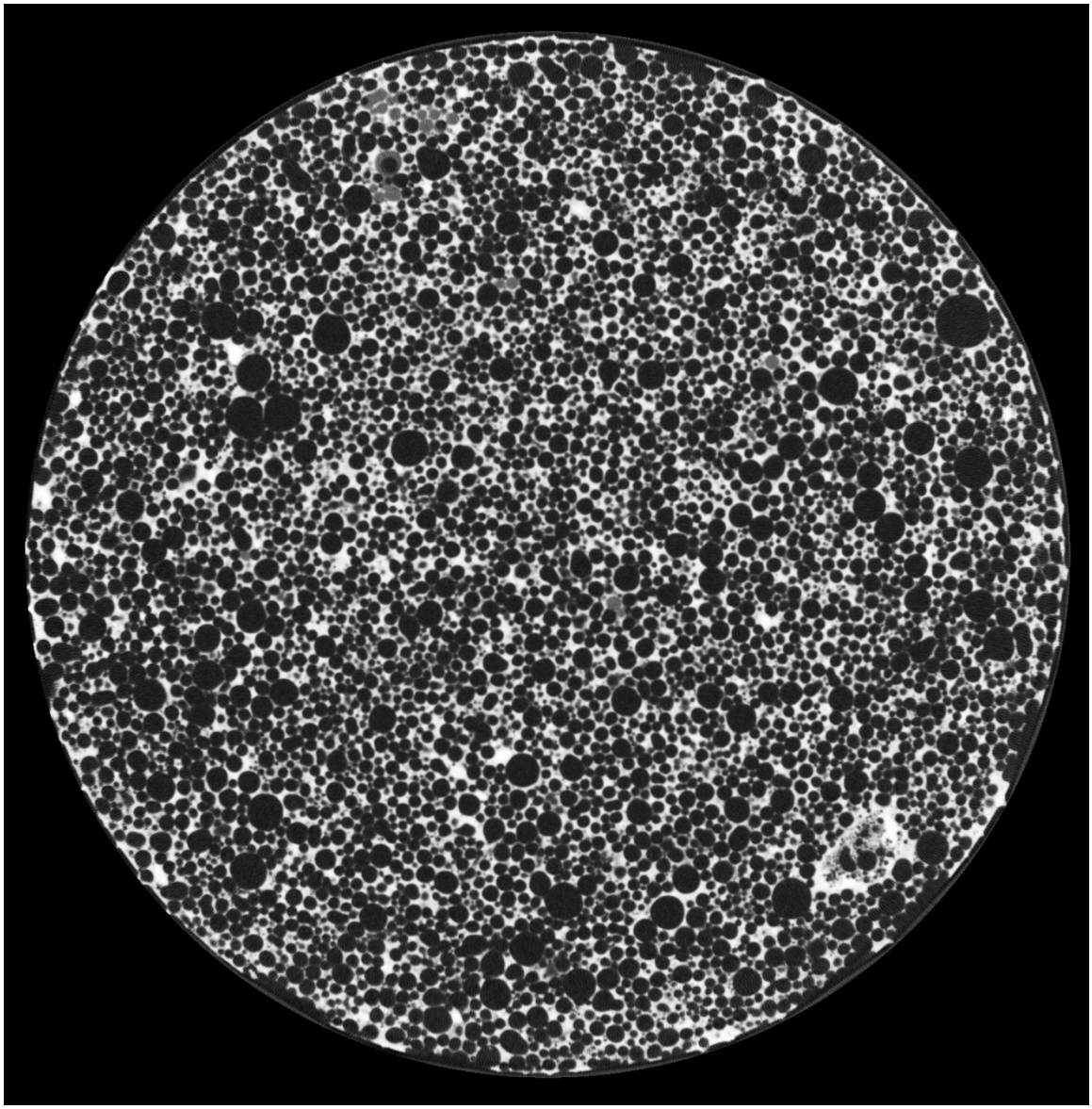

Figure 30. CT scan image of specimen B3-24 after the D1 treatment.

B3-24 CT image cross-section after the D1 treatment near the center of the specimen. The dark spherical objects are the foamed air voids with the light matrix being the concrete skeleton structure. The degree of saturation is 16.43%. Free pore water is visible in the image as grey spheres.

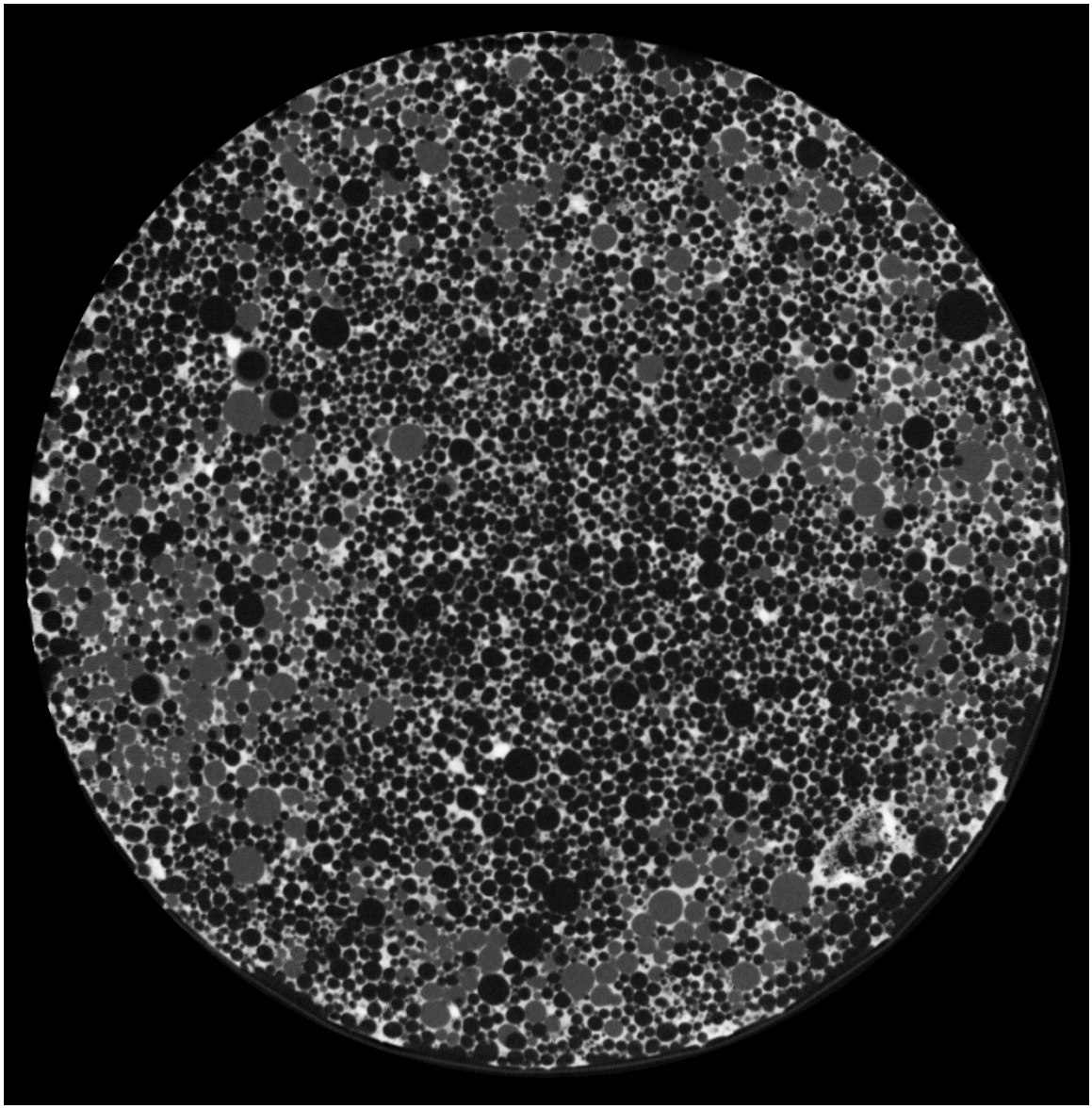

Figure 31. CT scan image of specimen B3-24 after the V8 treatment.

B3-24 CT image cross-section after the V8 treatment near the center of the specimen. The dark spherical objects are the foamed air voids with the light matrix being the concrete skeleton structure. The degree of saturation is 30.61%. Free pore water is visible in the image as grey spheres.

CHAPTER 4

HYDRAULIC CONDUCTIVITY

As discussed by Tiwari et al. (2017), further study of the fluid flow behavior of LCC is warranted. Also addressed by Tiwari et al. (2017) is a lack of knowledge regarding the behavior of the saturated hydraulic conductivity when the LCC is subjected to varying levels of effective confinement. Therefore, a saturated hydraulic conductivity test program was undertaken to explore further and answer these posed research questions.

Methods

Saturated hydraulic conductivity tests are typically performed in general accordance with ASTM D5084 (ASTM D18 Committee 2016a). Three test specimens from batches B1, B2, and B3 were prepared by cutting and surface-grinding the ends to an approximately three-inch finished length.

Previous research has shown that fluid flow bypass may occur between the specimen and the latex membrane when test specimens have a rough or porous surface on the circumference (Seely et al. 2014). LCC exhibits a rough, circumferential surface and has the potential to have a porous structure depending on the amount of adhesion between the cement and the Styrofoam mold during the curing process. This previous experience

led to a sidewall treatment to minimize or preclude fluid flow bypass. The specimen sidewall was treated with a thin paste of hydrated CETCO Super Gel-X bentonite (Figure 32) before the specimen was placed in a latex membrane and into the triaxial cell for testing (Figure 33).

After a curing age of 217 days, each test specimen underwent the hydrated bentonite sidewall treatment and was then placed in a latex membrane and sealed to the top and bottom caps of the triaxial cell. The cell was filled with de-aired water, and a slight pressure head confinement was applied while monitoring for leaks. The specimen was then flooded with de-aired water from the bottom up until the water was seen percolating from the top of the specimen. A minor amount of effective confining stress was maintained while systematically increasing the pore pressure to saturate the test specimen. This method of saturation, termed back-pressure saturation, follows Boyle's law, which describes the relationship between the pressure and volume of gas, ultimately pushing the gas within the specimen into solution of the pore water. As the pore pressure and confinement were incrementally increased, Skempton's *B*-value was computed in an undrained condition,

$$B = \frac{\Delta u}{\Delta \sigma_3} \qquad 10$$

where Δu is the undrained change in pore pressure when subjected to $\Delta \sigma_3$ (i.e., the change in the minor principal stress or confining stress). A *B*-value of 0.95 is commonly accepted as a point at which the test specimen was considered saturated. Upon reaching a *B*-value of 0.95 or greater, the effective confining stress was increased to the desired level of confinement. The volume of the cell and test specimen was monitored with time until consolidation was complete, and no perceptible volume change was observed in the

system. A hydraulic gradient, i, is applied to the test specimen by increasing the head, Δh, at the bottom of the specimen with respect to the top of the specimen,

$$i = \frac{\Delta h}{l} \tag{11}$$

where l is the length of the specimen. The flow rate, q, is measured and recorded and the hydraulic conductivity, k, is estimated following Darcy's law,

$$q = k \cdot i \cdot A \tag{12}$$

where A is the specimen cross-sectional area. Since the apparatus used in this study employed a set of burettes and an air-over water pressure system, the falling-head, rising-tailwater hydraulic conductivity is calculated by,

$$k = \frac{a \cdot l}{2 \cdot A \cdot \Delta t} \cdot \ln\left(\frac{\Delta h_1}{\Delta h_2}\right) \tag{13}$$

where a is the cross-section area of the burettes, Δt is the change in time, $t_2 - t_1$, and Δh_1 and Δh_2 are the head losses across the specimen at times t_1 and t_2, respectively. The temperature of the test system was noted at the time of the test to correct for fluid density and viscosity.

The effective confining stress was increased to the subsequent prescribed pressure after obtaining multiple steady-state readings, followed by consolidation and permeability steps. This method of repeated testing with incremental increases in effective confining pressure is termed a staged test.

Results

A summary of the hydraulic conductivity, corrected for fluid density and viscosity to 20° C, is shown in Table 11. The average hydraulic conductivity from the tests was

$4.9x10^{-5}$ cm/sec, with a maximum of $1.0x10^{-4}$ cm/sec and a minimum of $9.6x10^{-6}$ cm/sec. These values fall within a range typically obtained for silts, karst, and reef limestones (Schwartz and Zhang 2003). On average, the test specimens exhibited a 0.04 order-of-magnitude decrease in hydraulic conductivity per psi of effective confinement increase from 2.5 to 10 psi. In other words, the test data indicates about 25 psi of effective confining stress is required to change the hydraulic conductivity by one order of magnitude. The lowest effect from confinement increase was about 0.01 of an order of magnitude. The highest effect from confinement increase was about 0.08 orders-of-magnitude decrease per psi of effective confinement increase. The results are shown in Figure 34.

Discussion

Although the hydraulic conductivity tests included Skempton's *B*-checks to confirm saturation, it does not guarantee 100% saturation during the test's permeability phase. As shown in Figure 23, Figure 27, and Figure 31, LCC exhibits occluded and continuous (interconnected) void spaces. The continuous void spaces that form upon casting or are later connected through microfractures formed through the curing process. Although the *B*-checks reflect near 100% saturation as pressure equilibrium likely occurs across the thin vesicle walls, the hydraulic conductivity is likely governed by advection flow through the interconnected void spaces and microfractures.

The data generated for this study indicate that confining pressure influences the hydraulic conductivity with an average of 0.04 orders-of-magnitude decrease in hydraulic conductivity per psi of effective confinement increase. In addition, we believe that the

bentonite gel sidewall treatment employed aids in eliminating potential bypass flow and, therefore, potentially erroneous results. Also, increasing the confinement pressure likely affects the microfracture network within the LCC by decreasing the fracture openings and decreasing the effective hydraulic radii of some of the interconnected voids. Lastly, the hydraulic conductivity results reported by Tiwari et al. (2017) for a higher unit weight LCC (lower void ratio) ranged from 1.7×10^{-4} cm/sec to 1.2×10^{-3} cm/sec, about an order of magnitude higher than the values attained in this study. It is presumed that sidewall bypass flow may explain this discrepancy. Because LCC is somewhat variable in its mechanical properties, some differences can be expected in test results. Nonetheless, we recommended that sidewall bypass treatment (bentonite gel, vacuum grease, or other) be employed when testing the hydraulic conductivity of LCC to reduce experimental variability.

Table 11. Summary of the hydraulic conductivity test results.
The hydraulic conductivity values are in cm/sec. The values in the table are corrected to 20° C based on the permeant fluid density and viscosity at the time of the test.

Test Specimen	Effective confining stress (psi) 2.5	5.0	7.5	10.0
B1-20	2.24E-05	1.74E-05	1.53E-05	1.48E-05
B1-21	5.26E-05	4.38E-05	3.95E-05	2.31E-05
B1-22	5.81E-05	5.14E-05	5.09E-05	4.88E-05
B2-20	2.00E-05	1.68E-05	1.33E-05	9.58E-06
B2-21	9.67E-05	9.17E-05	7.26E-05	7.18E-05
B2-22	8.94E-05	7.73E-05	6.71E-05	6.54E-05
B3-20	5.81E-05	4.22E-05	3.56E-05	3.45E-05
B3-21	1.04E-04	5.05E-05	4.09E-05	2.68E-05
B3-22	1.01E-04	6.13E-05	4.19E-05	2.52E-05

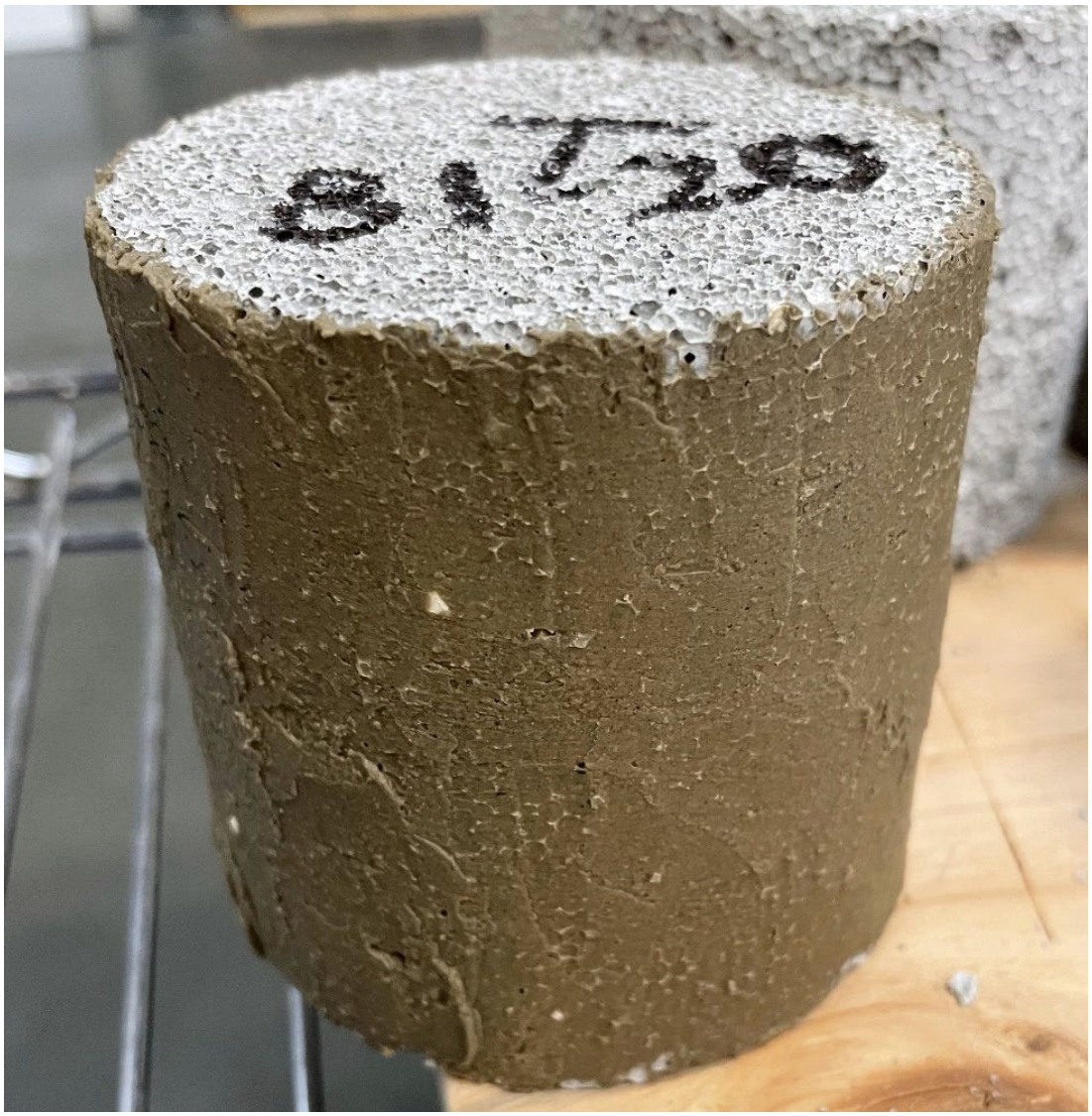

Figure 32. Photo of the LCC specimen with the bentonite gel sidewall treatment.

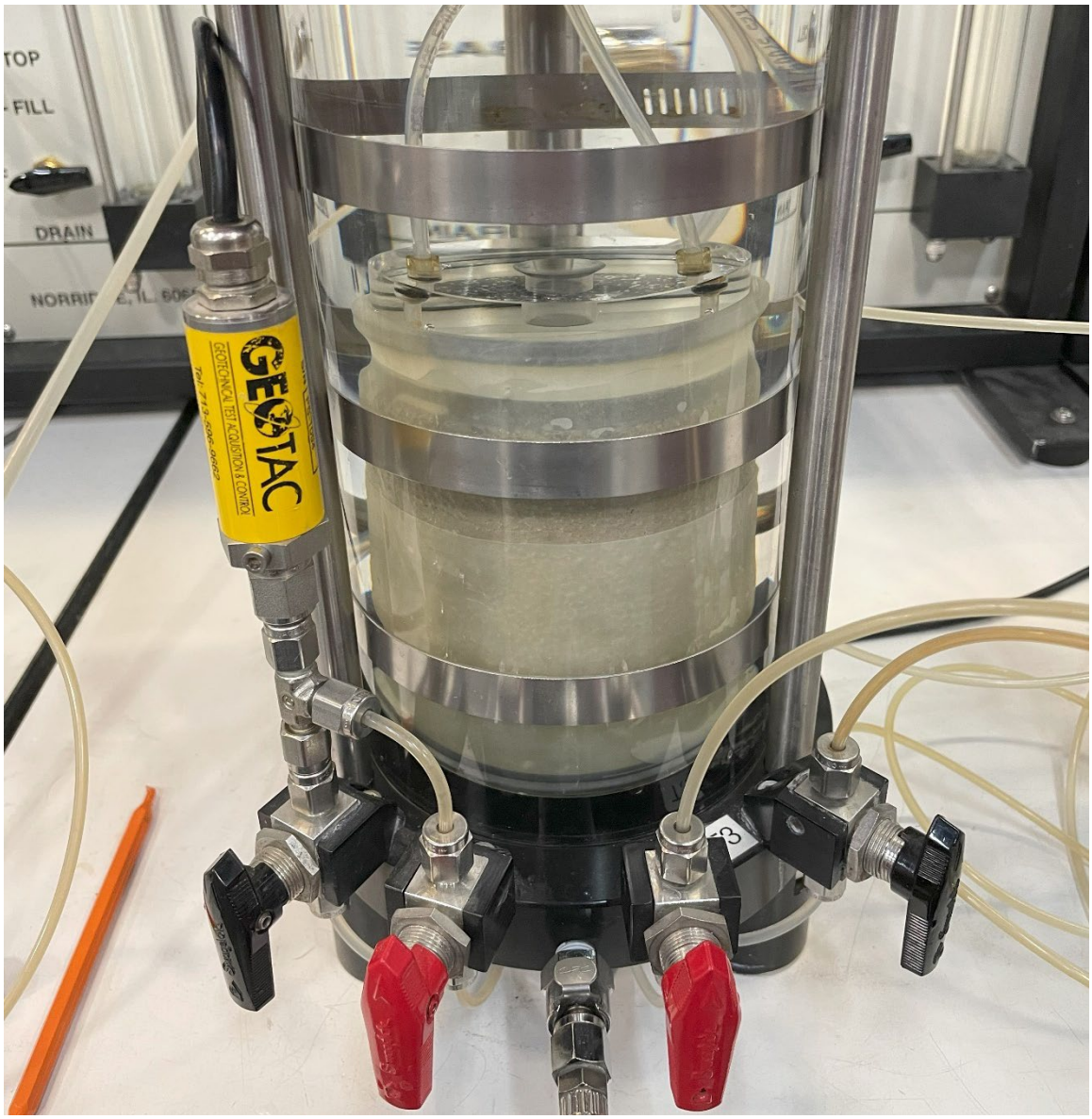

Figure 33. Photo of an LCC specimen in the hydraulic conductivity test cell.

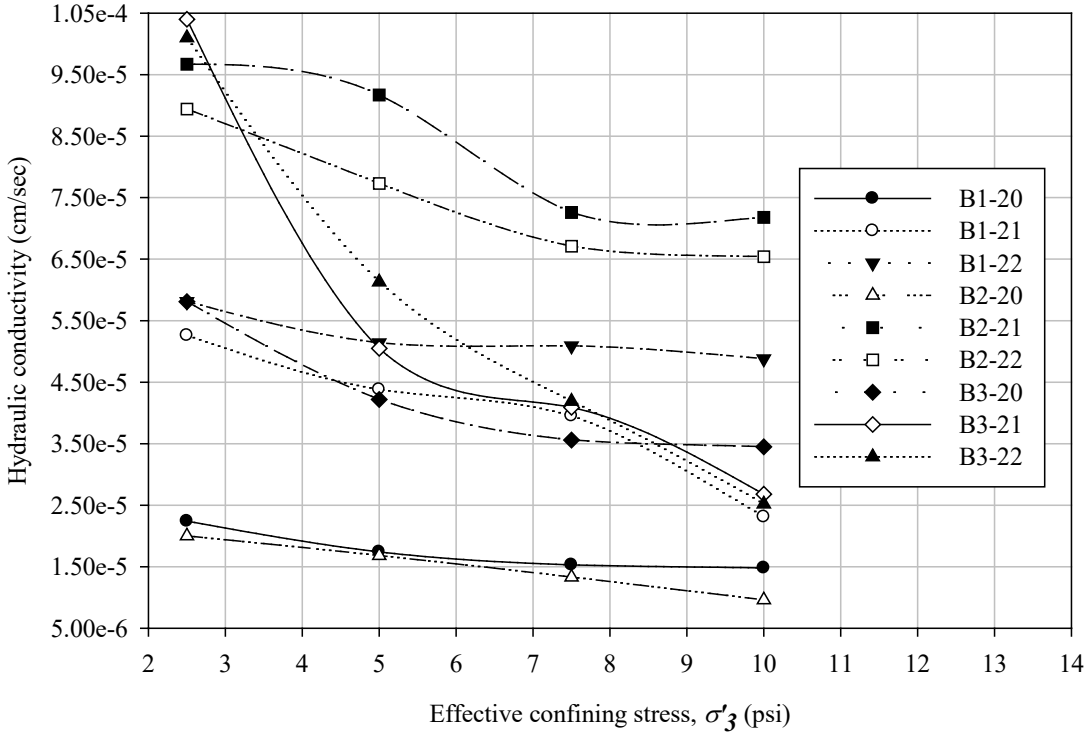

Figure 34. Hydraulic conductivity over a range of effective confining stresses.

CHAPTER 5

RESILIENT MODULUS

The RM test allows for an estimation of the modulus of elasticity of a material when subjected to rapid loading. The state of stress varies throughout the test and is designed to simulate the states of stress when a pavement base and subbase materials experience traffic loads. The material's RM is used to estimate the structural layer coefficients or is used directly in mechanistic-empirical pavement design. The test results of the RM, M_R, are typically fit to one or more of the following four equations (Von Quintus and Killingsworth 1998). (We note that the functional form of the equations is a statistical fit of their data used for convenience and does not imply a mechanistic relationship.)

$$M_R = K_1 \cdot \sigma_B^{K_2} \quad (14)$$

$$M_R = K_3 \cdot \sigma_d^{K_4} \quad (15)$$

$$M_R = K_5 \cdot \sigma_d^{K_6} \cdot (1 + \sigma_3)^{K_7} \quad (16)$$

$$M_R = K_8 \cdot p_a \cdot \left(\frac{\sigma_B}{p_a}\right)^{K_9} \cdot \left(\frac{\sigma_d}{p_a}\right)^{K_{10}} \quad (17)$$

where K_1 through K_{10} are fitting parameters, p_a is one atmosphere, and σ_B is the bulk stress,

$$\sigma_B = (\sigma_d + \sigma_3) + 2 \cdot \sigma_3 \quad 18$$

where σ_d is the deviator stress,

$$\sigma_d = \sigma_1 - \sigma_3 \quad 19$$

where σ_1 is the major principal stress, and σ_3 is the major principal stress or confining stress.

A primary objective of this study was to estimate the possible range of values of the RM of LCC for engineering applications. To our knowledge, this information does not exist in the published literature. This information will improve the profession's understanding of LCC's long-term durability, contributing to its future implementation. Also, as part of this durability study, we will explore the possible effect(s) that water (as measured by saturation degree) has on the RM.

A series of RM tests were performed to achieve these objectives. The series included test specimens treated with the saturation protocols discussed in Chapter 3 with curing ages ranging from 1,051 to 1,077 days. This program included 12 specimens each from the AD, H100, M5, D1, and W1 saturation groups. Also, as discussed in Chapters 6 and 7, each specimen was tested without delay for unconfined or triaxial compressive strength upon completing the RM testing. As such, this allowed a direct comparison of the test results measured in the low-strain, nondestructive RM tests and the high-strain, destructive compressive strength tests.

Methods

The RM tests were performed in accordance with AASHTO T-307 (AASHTO Technical Subcommittee: 1a, Soil and Unbound Recycled Materials 2017). The tests were performed on a calibrated GeoComp LoadTrac II load frame in conjunction with a three-phase stepper motor cyclic actuator and a Cyclic-RM Actuator Controller. The test specimen was placed in a triaxial cell and isolated with a latex rubber membrane, as described in Chapter 4, but without any sidewall treatment. The triaxial cell was placed and centered in a load frame, and the cell pressure was controlled by regulated compressed air through the Cyclic-RM Actuator Controller. The deviator stress was applied from the three-phase stepper motor cyclic actuator, which is also controlled by the Cyclic-RM Actuator Controller (see Figure 35). Displacement measurements are taken with two linear displacement transducers to compute the axial strain from the applied deviatoric stress. The deviator load is a haversine-shaped load pulse for 0.1 seconds followed by a 0.9-second rest period. The confining pressure and deviator stress is varied from an initial conditioning sequence, 0, followed by 15 additional test sequences, as summarized in Table 12. The test is performed in a drained condition with the sample valves vented to atmospheric pressure. The RM results, the applied cyclic stress divided by the axial strain, are reported as the average of the moduli resulting from the final five load pulses for each sequence 1 through 15.

Results

The results from the RM of the LCC specimens as a function of the confining stress, as a function of the deviator stress as a function of the dry unit weight, as a

function of the saturation, and as a function of the height-to-diameter ratio are shown in Figure 36, Figure 37, Figure 38, Figure 39, and Figure 40, respectively. The average RM measured was 70,974 psi, with a maximum of 671,130 psi and a minimum of 19,123 psi. The complete test reports from each of the RM tests are attached in Appendix C, where the data for each test specimen is fit to Equation 14, Equation 15, Equation 16, and Equation 17.

Discussion

The data shown in Figure 36 indicate an increase in measured RM with increased confining stress. This response is expected from a fundamental soil and rock mechanics perspective because confining stress increases the interparticle contact stress, thus increasing the material's stiffness.

The data shown in Figure 37 indicate an increase in RM with increasing deviator stress. Experience has shown that soils behave similarly when subjected to RM testing. Also, as expected, the data shown in Figure 38 indicate an increase in RM with an increase in the dry unit weight. We conclude that an increase in dry unit weight provides more solids (cement) to the specimen's skeletal structure, increasing its stiffness.

However, the data shown in Figure 39 does not provide a strong relationship between the degree of saturation and its possible influence on the stiffness of LCC under the loading schedule shown in Table 12. The data may indicate a slight increase in RM as the saturation increases. We believe that the inclusion of the water, whether absorbed or adsorbed in the skeletal matrix, behaves in an undrained condition due to the rapid loading of the RM test protocol. This effect may have a minor contribution to the

stiffness of the LCC specimen due to the included water's relative incompressibility. However, this independent variable has a minor contribution to LCC's stiffness within the range of saturation treatments explored.

Lastly, the data indicate a decrease in stiffness as the specimen's length (or height-to-diameter ratio) increases. However, this effect is an artifact of the specimen preparation and an uncontrolled variable in the study. This effect and its removal from the correlation evaluations are further addressed in Chapter 8.

In summary, the independent variables with the highest statistically significant correlations with RM are the confining stress, deviator stress, dry unit weight, and the specimen's height-to-diameter ratio. Therefore, the data shown in Figure 36, Figure 37, Figure 38, Figure 39, and Figure 40 are used in model generation using multilinear regression presented in Chapter 8.

Table 12. Resilient modulus testing sequence for base/subbase materials.

Sequence No.	Confining pressure (psi)	Max. axial stress (psi)	Cyclic stress (psi)	Constant stress (psi)	No. of load applications
0	15	15	13.5	1.5	500–1000
1	3	3	2.7	0.3	100
2	3	6	5.4	0.6	100
3	3	9	8.1	0.9	100
4	5	5	4.5	0.5	100
5	5	10	9.0	1.0	100
6	5	15	13.5	1.5	100
7	10	10	9.0	1.0	100
8	10	20	18.0	2.0	100
9	10	30	27.0	3.0	100
10	15	10	9.0	1.0	100
11	15	15	13.5	1.5	100
12	15	30	27.0	3.0	100
13	20	15	13.5	1.5	100
14	20	20	18.0	2.0	100
15	20	40	36.0	4.0	100

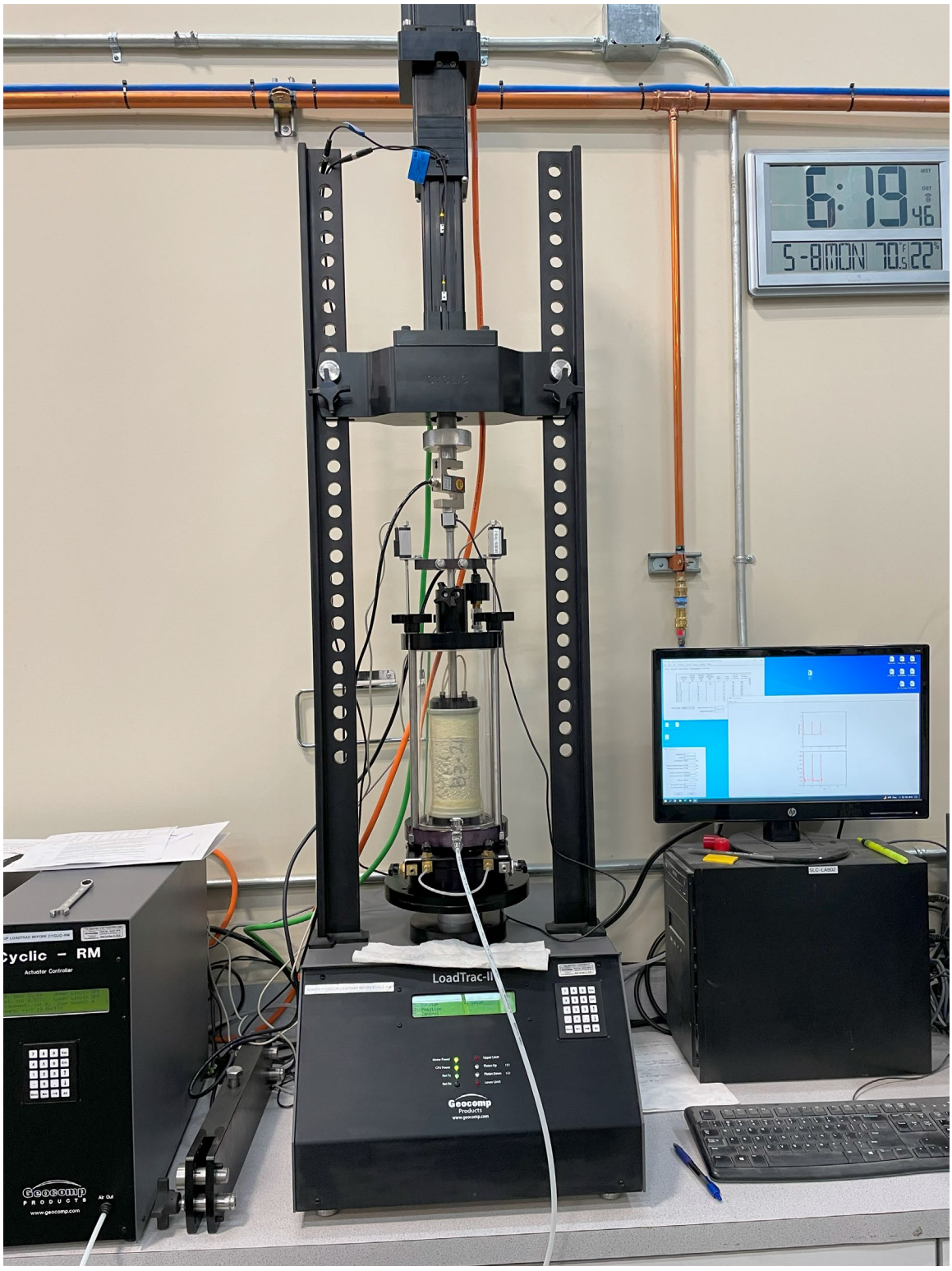

Figure 35. Photo of the resilient modulus testing apparatus.

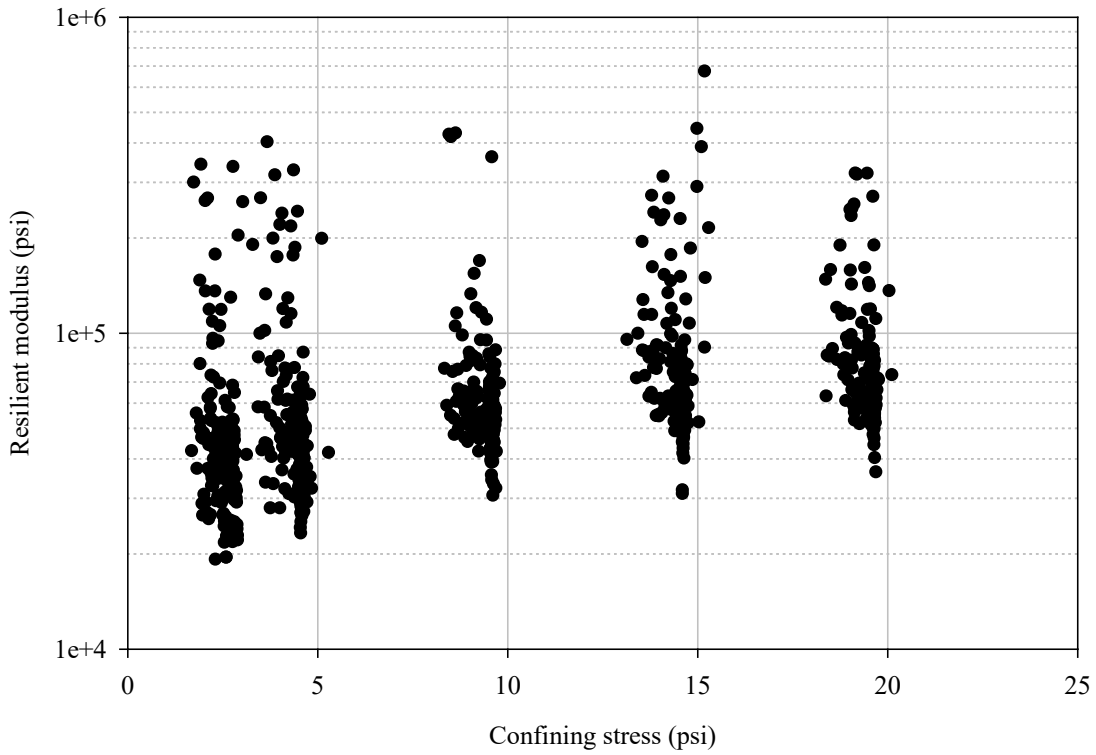

Figure 36. Resilient modulus of the LCC specimens as a function of confining stress.

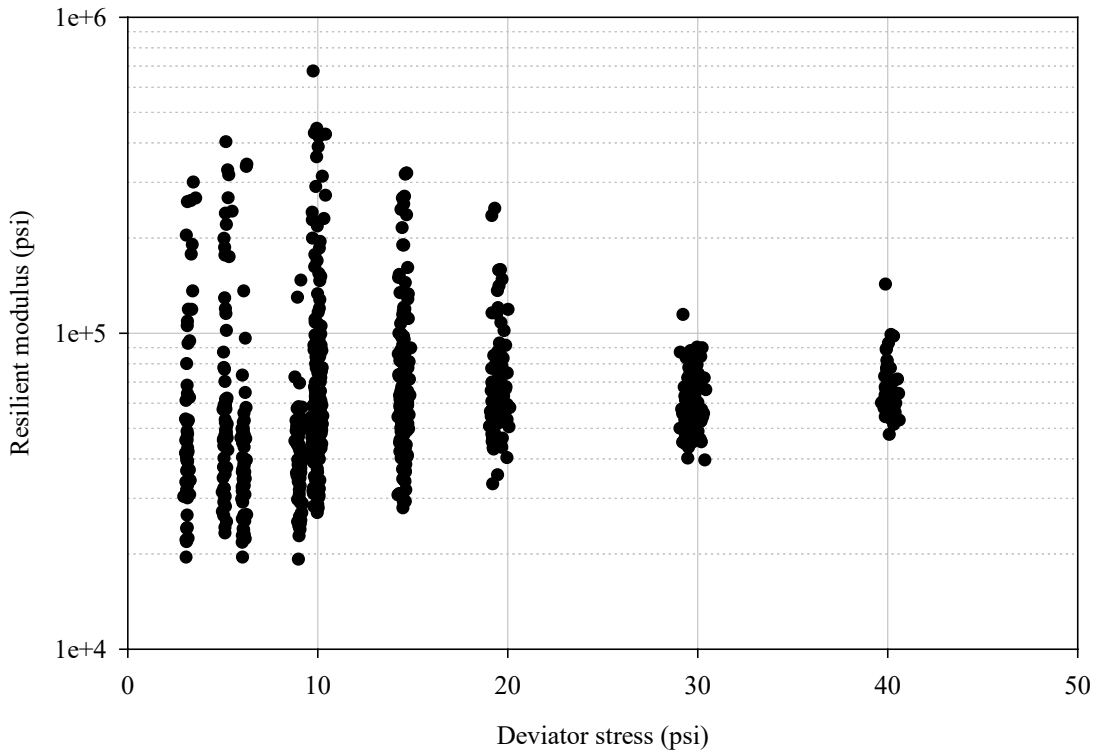

Figure 37. Resilient modulus of the LCC specimens as a function of the applied deviator stress.

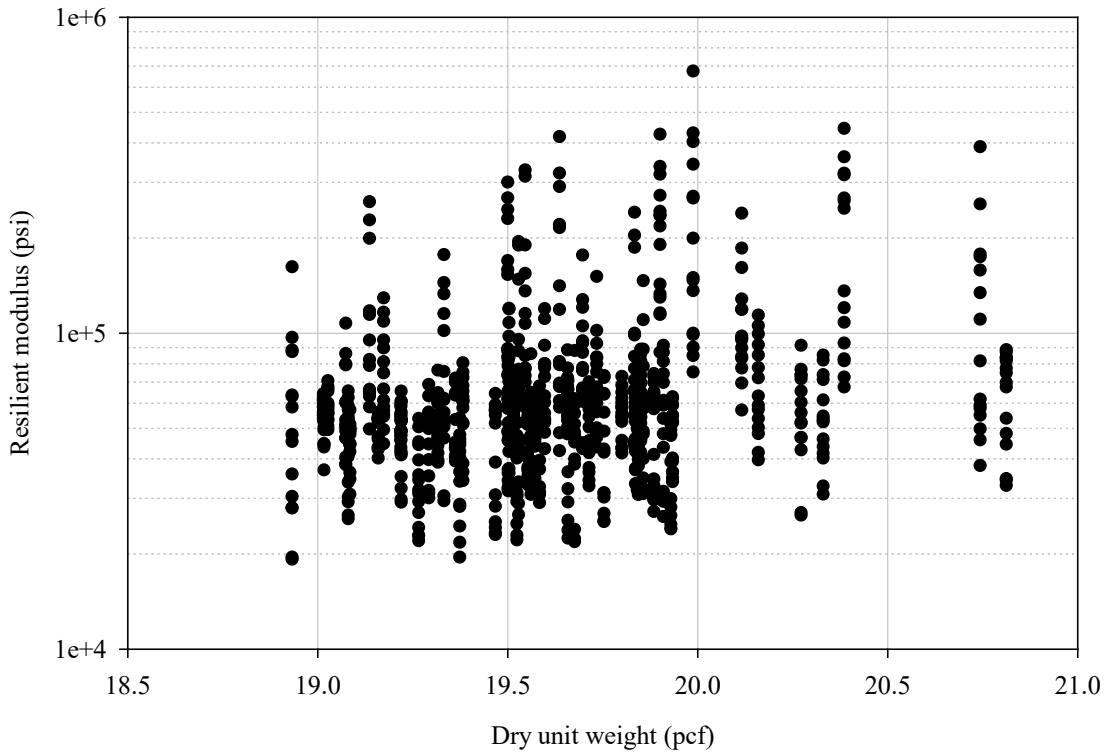

Figure 38. Resilient modulus of the LCC specimens as a function of the dry unit weight.

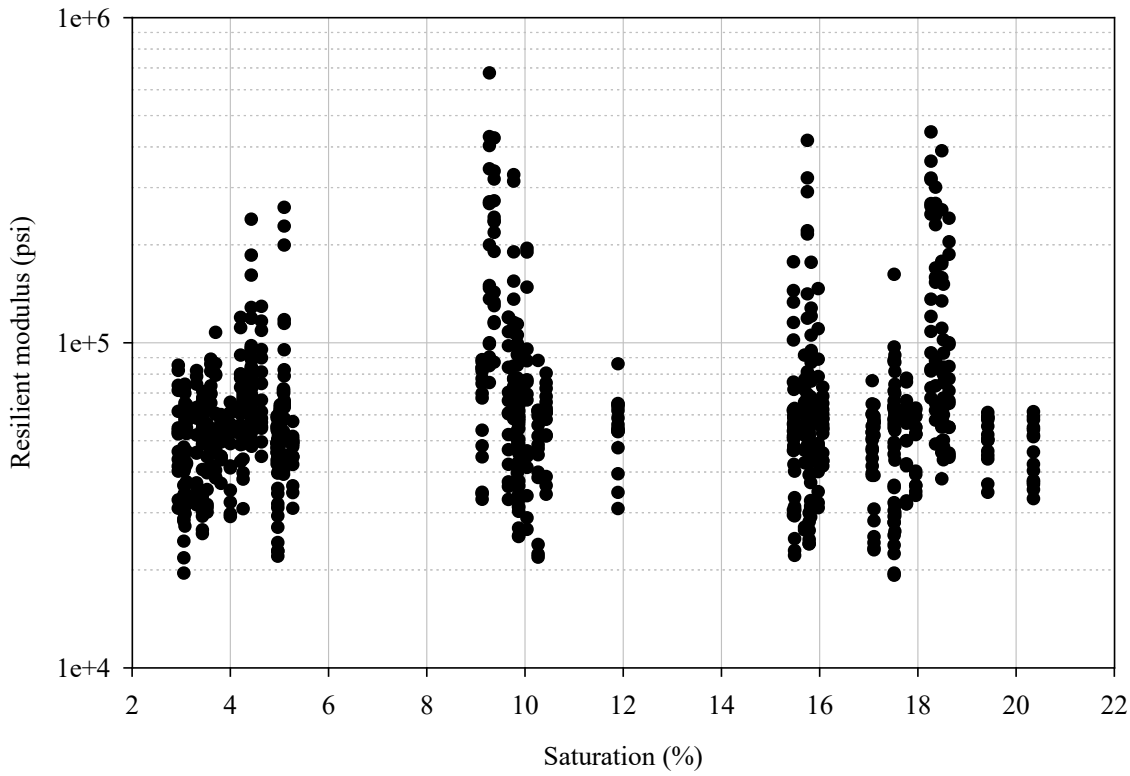

Figure 39. Resilient modulus of the LCC specimens as a function of saturation.

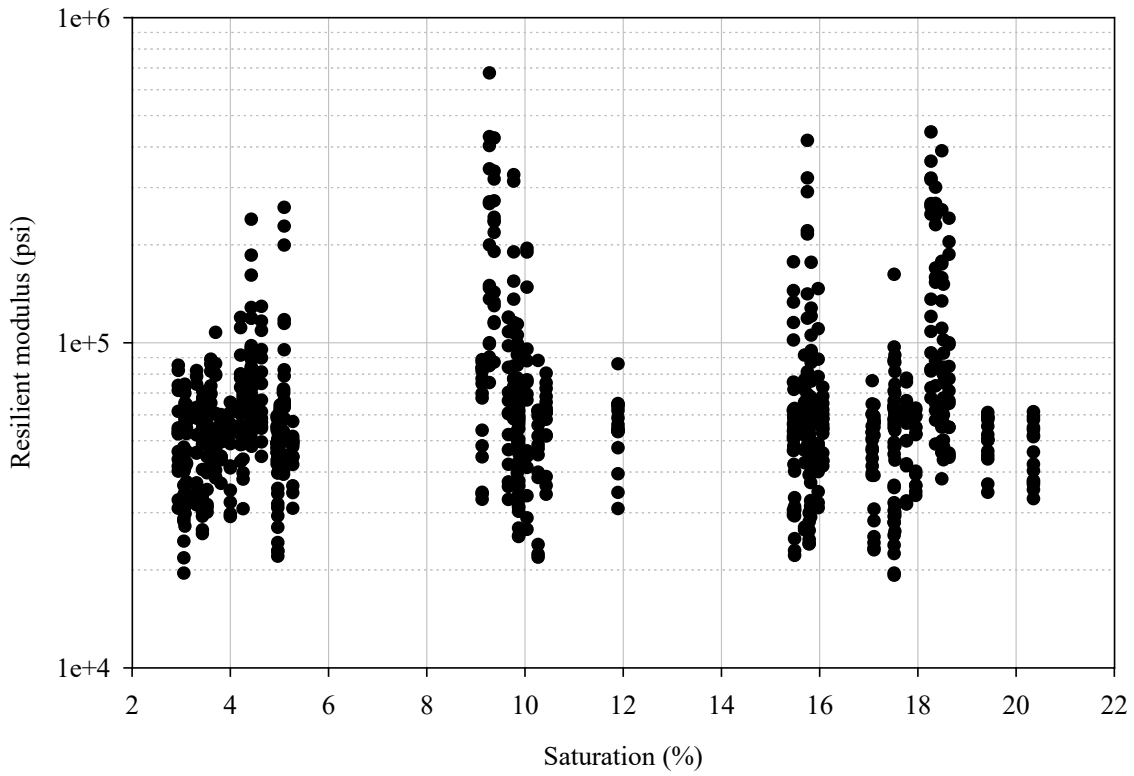

Figure 40. Resilient modulus of the LCC specimens as a function of the height-to-diameter ratio.

CHAPTER 6

UNCONFINED COMPRESSIVE STRENGTH

The UCS test is relatively quick, inexpensive, and requires no specialized equipment beyond what is found in a typical material testing laboratory. Because of this, the current state of practice in engineering design primarily utilizes the UCS for LCC quality control testing.

One objective of this study was to determine the lapsed time when the mechanical behavior of LCC no longer has appreciable change from the curing reaction. It is likely that, in practice, equipment availability constraints are encountered, and tests will be performed sequentially and at different curing times. Therefore, it will be important when performing suites of tests (e.g., UCS and three-point triaxial tests) and correlating the results with the results from other tests (e.g., RM tests) that the effect of curing time is controlled or accounted for in the experimental design and interpretation of the results. Therefore, UCS tests were performed on air-dried specimens throughout the curing process to understand LCC's strength gain with time. The test program included 57 UCS tests with curing ages ranging from seven days to 99 days. The series was subsequently supplemented with five additional UCS tests that extended beyond 1,050 days of curing.

Another primary objective of this study was to determine the effects of the degree of saturation on the UCS of LCC. As such, a series of UCS tests were performed to

achieve this objective. The series included test specimens with ages ranging from 1,051 to 1,075 days and at various saturation treatments, as discussed in Chapter 3. These treatments included five specimens each from the AD, H100, M5, D1, and W1 saturation groups, respectively. Additionally, all UCS tests in this series were performed promptly after the completion of RM testing so that the specimens' water content and curing time remained unchanged between the execution of the UCS and RM testing.

Methods

The specimens for UCS testing were prepared as described in Chapter 2. The tests were performed on a calibrated GeoComp LoadTrac II load frame. The system compliance was accounted for in all strain computations by measuring the system displacements as a function of force using a 7075-aluminum calibration disc (see Figure 41). The calibration disc was machined from 3-inch diameter stock on a Grizzly G7075 metal lathe with an end parallelism of less than 0.001" across the diameter.

Testing in unconfined compression was performed in general accordance with ASTM C495 and ASTM D2166 (ASTM C09 Committee 2012; ASTM D18 Committee 2016b). The initial 27 tests were performed on surface-ground-only test specimens against the end platens (Figure 42). Following conversations with Aerix Industries, the method was modified to utilize Forney end caps with 50-durometer pads. This capping treatment allowed a consistent comparison against industry methods (Figure 43). All tests were initiated by applying a seating load of 5 lbs. The loading strain rate varied from 0.5%/min to 0.75%/min, where the most consistent results were found to be at 0.75%/min, with the specimens typically reaching failure within one minute. Initially, it

was observed that the specimens tended to fail from the bottom up, indicating the weakest material is likely located at the bottom of the specimens. Subsequently, the test specimens were prepared by removing 1/8" to ¼" of the bottom of the samples before testing. After testing, the failed specimens were placed in a convection oven at 230° F for water content determinations.

Results

The results from the initial UCS testing with the peak axial stress as a function of time are shown in Figure 44. Most of the test specimens exhibited either an initial reduction in strength before reaching the ultimate UCS stress or a substantial deviation from the initial straight-line portion of the stress-strain curve. This strength loss (i.e., deviation from Young's modulus line) was recorded and identified as the initial yield. The initial yield of the test specimens as a function of time is also shown in Figure 44.

Figure 45 shows the results of the initial yield and UCS for the cured specimens (older than 10,50 days) as a function of the dry unit weight in pcf. The results of the initial yield and UCS as a function of saturation are shown in Figure 46. The results of Young's modulus as a function of dry unit weight are shown in Figure 47. Finally, Figure 48 displays a plot of Young's modulus of the test specimens as a function of saturation. The complete test reports from each of the UCS tests are attached in Appendix D.

Discussion

The data from Figure 44 were used to estimate the time at which the engineering behavior of LCC no longer has appreciable effects from the curing reaction. This point in time was calculated by performing a nonlinear regression on the data and evaluating these results. The nonlinear regressions were performed using SigmaPlot version 11.0.0.77 in the manner described in Chapter 2. Several hyperbolic and exponential forms were regressed through an iterative process with a best-fit mean line and a 95% confidence interval band (i.e., $\alpha = 0.05$). The functional form given in Equation 20 provided the best fit with satisfactory *p*-values. Summaries of the regression statistics for each test specimen are presented in Table 10. A plot of the fitted model (Equation 20) from the regression is shown in Figure 49.

$$U = a(1 - e^{-b \cdot t}) \tag{20}$$

To estimate the time at which the engineering behavior of LCC no longer has appreciable effects from the curing reaction, we chose a 1% change in slope as a reasonable (i.e., non-zero) criterion. Calculating the first derivative of Equation 20 yields,

$$\frac{dU}{dt} = a \cdot b \cdot e^{-b \cdot t} \tag{21}$$

and solving for *t*, in Equation 21 gives,

$$t = \frac{-\ln\left(\frac{\frac{dU}{dt}}{a \cdot b}\right)}{b} \tag{22}$$

Given the one-percent slope criteria above and the nonlinear regression constants from Table 13, the UCS for the LCC reaches a point where negligible effects from the curing are achieved after 70 days.

As expected, the data shown in Figure 45 and Figure 47 indicate an increase in compressive strength and Young's modulus with increasing dry unit weight. However, this study's data range for unit weight is relatively small because we sought to have cast specimens of the same unit weight. Nonetheless, the increase in dry unit results from more solids (i.e., cement) forming the specimen's skeletal structure, contributing to increases in strength and stiffness.

The data shown in Figure 46 and Figure 48 indicate a slight decrease in the compressive strength and stiffness as the saturation increases. The matric suction within the specimen is decreased as the degree of saturation increases by increasing the radii of the water-mineral interface menisci and reducing the water tensile forces and generation of localized excess pore pressure. This decrease in matric suction contributes to decreased stiffness and strength measured in the LCC.

The independent variables with the highest correlations are the dry unit weight and the degree of saturation. Therefore, the data shown in Figure 45, Figure 46, and Figure 48 are used in model generation using multilinear regression, as discussed in Chapter 8.

Table 13. Summary of the nonlinear regression statistics for the unconfined compressive strength as a function of curing time (Equation 20).

Model parameter	Regression value	*p*-value	*p*-value acceptance criterion
a	143.6342	<0.0001	$<\alpha$
b	0.1043	<0.0001	$<\alpha$
R^2	0.3073		
ANOVA		<0.0001	$<\alpha$
Normality		0.4379	$>\alpha$

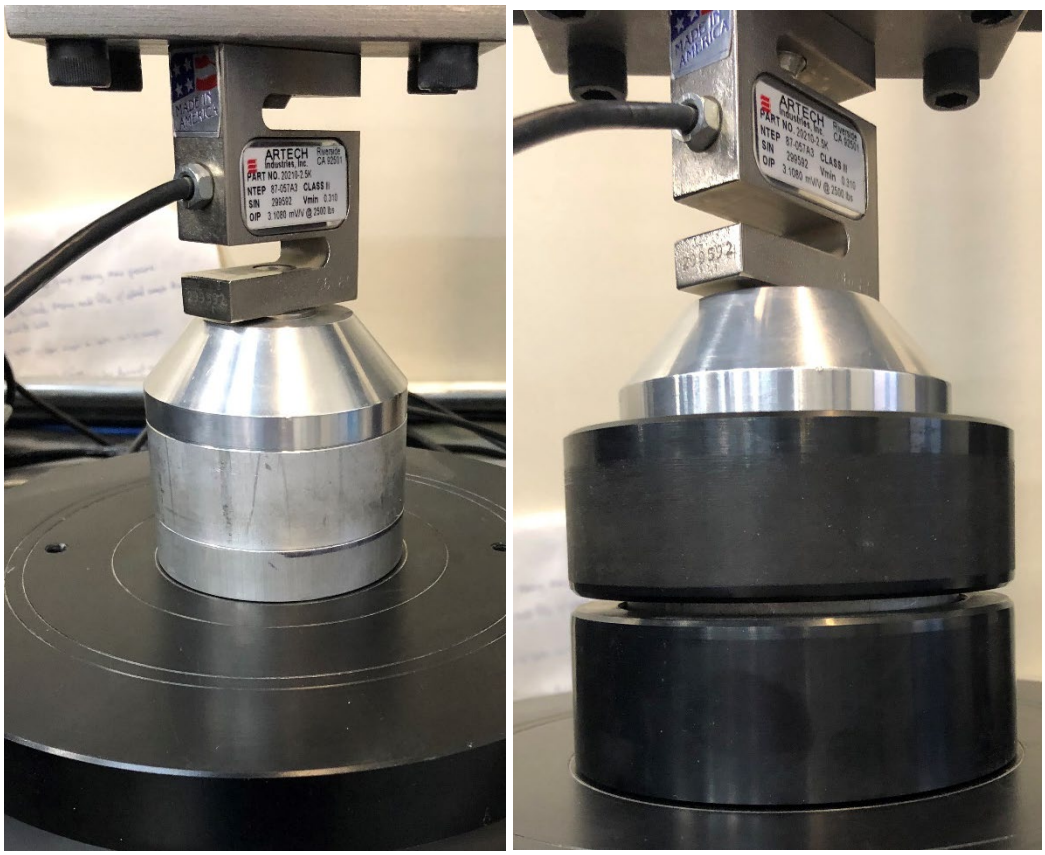

Figure 41. Photo of the 7075-aluminum system compliance calibration disc.

Figure 42. Photo of a specimen prepared for UCS testing in the load frame without padded end caps.

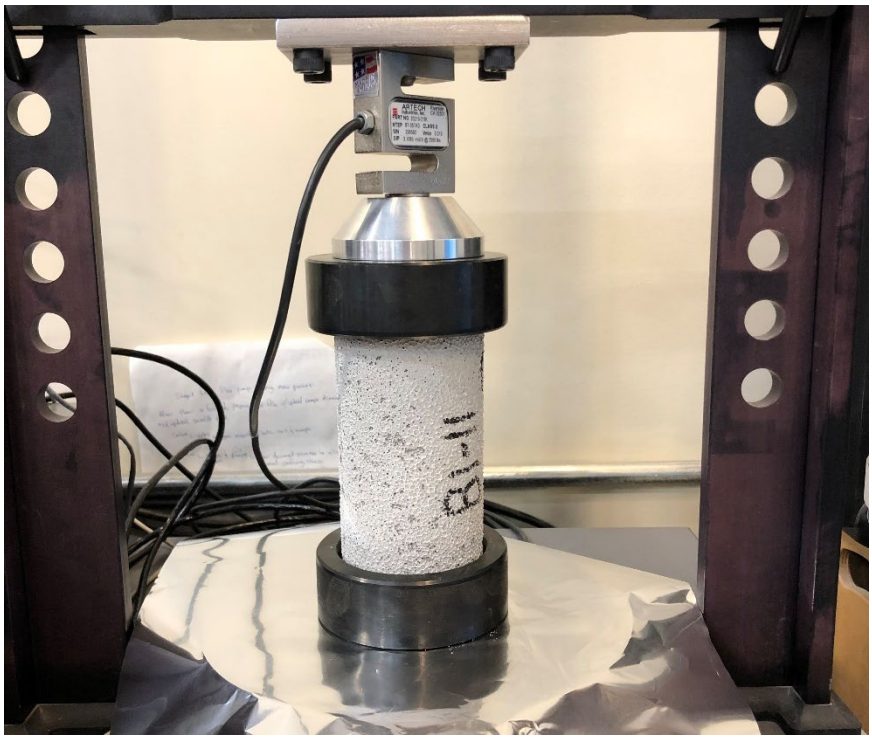

Figure 43. Photo of a specimen prepared for UCS testing in the load frame with padded end caps.

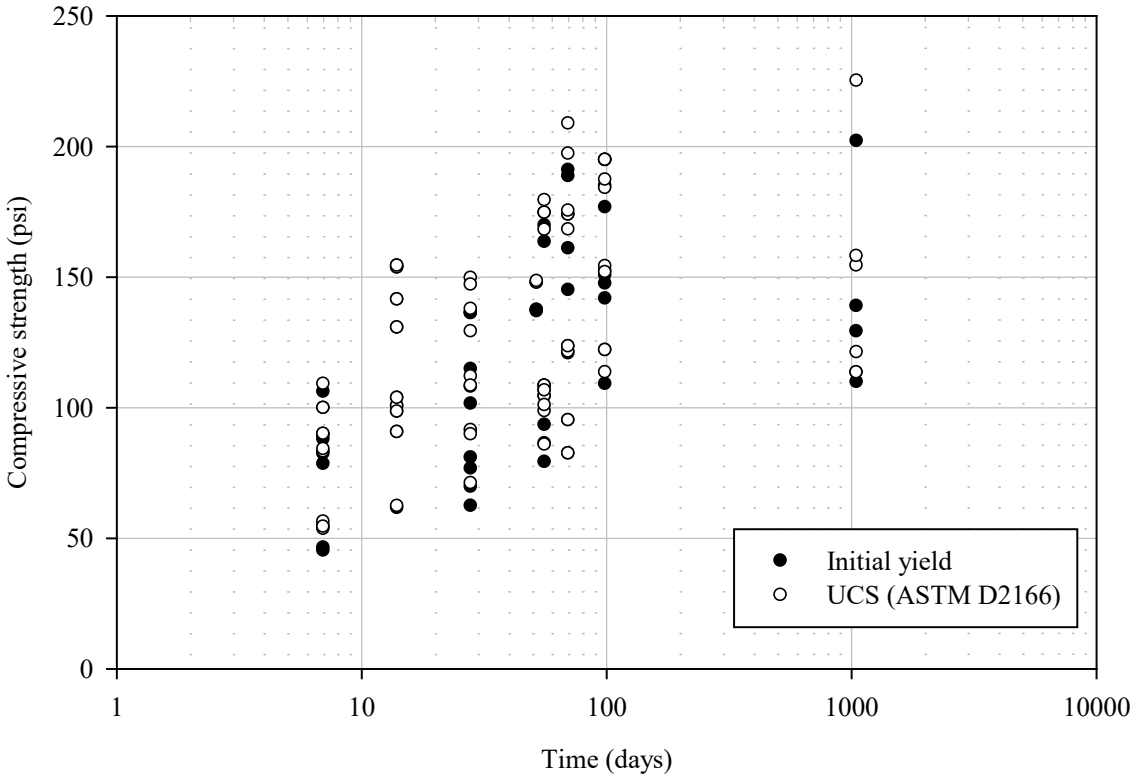

Figure 44. Initial yield and the UCS of the air-dried LCC specimens as a function of time.

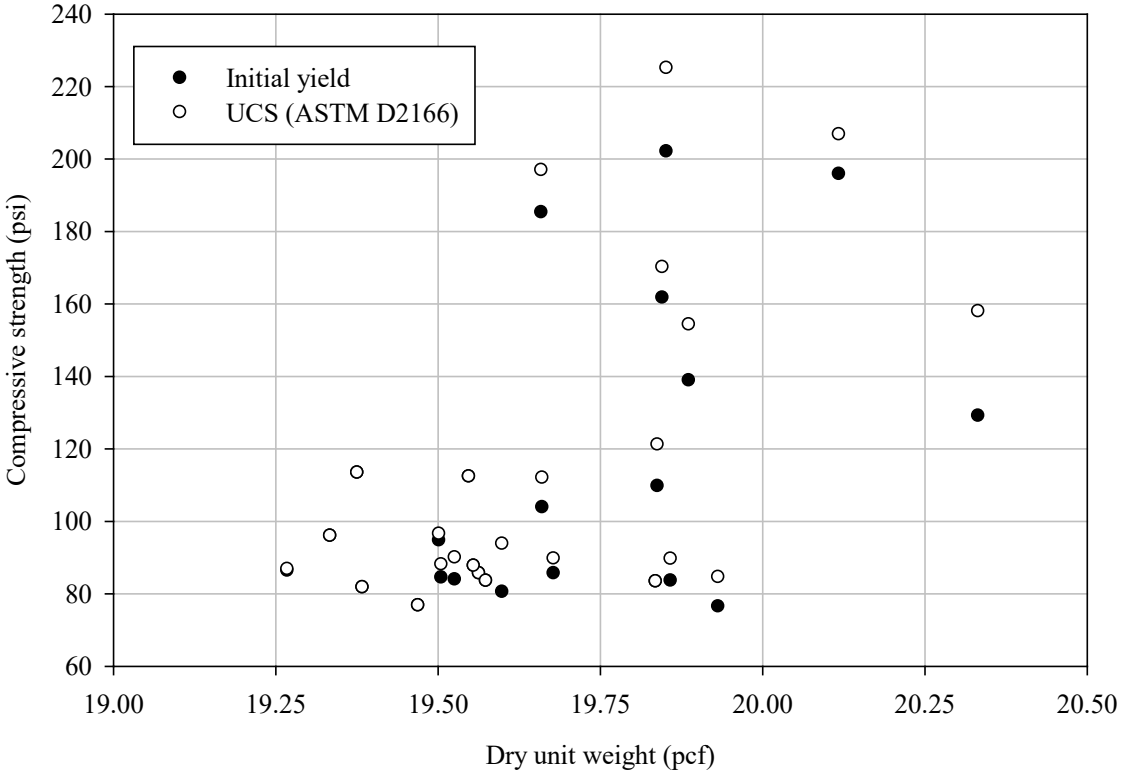

Figure 45. Initial yield and the UCS of the cured LCC specimens as a function dry unit weight.

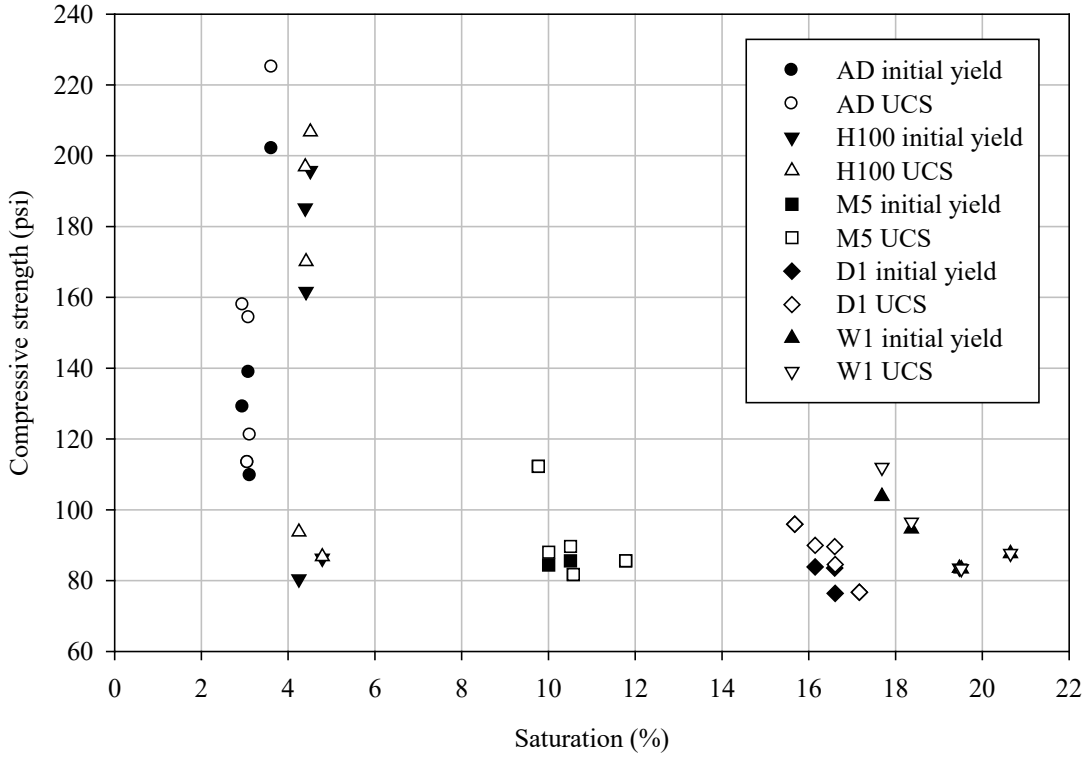

Figure 46. Initial yield and the UCS of the LCC specimens as a function of saturation.

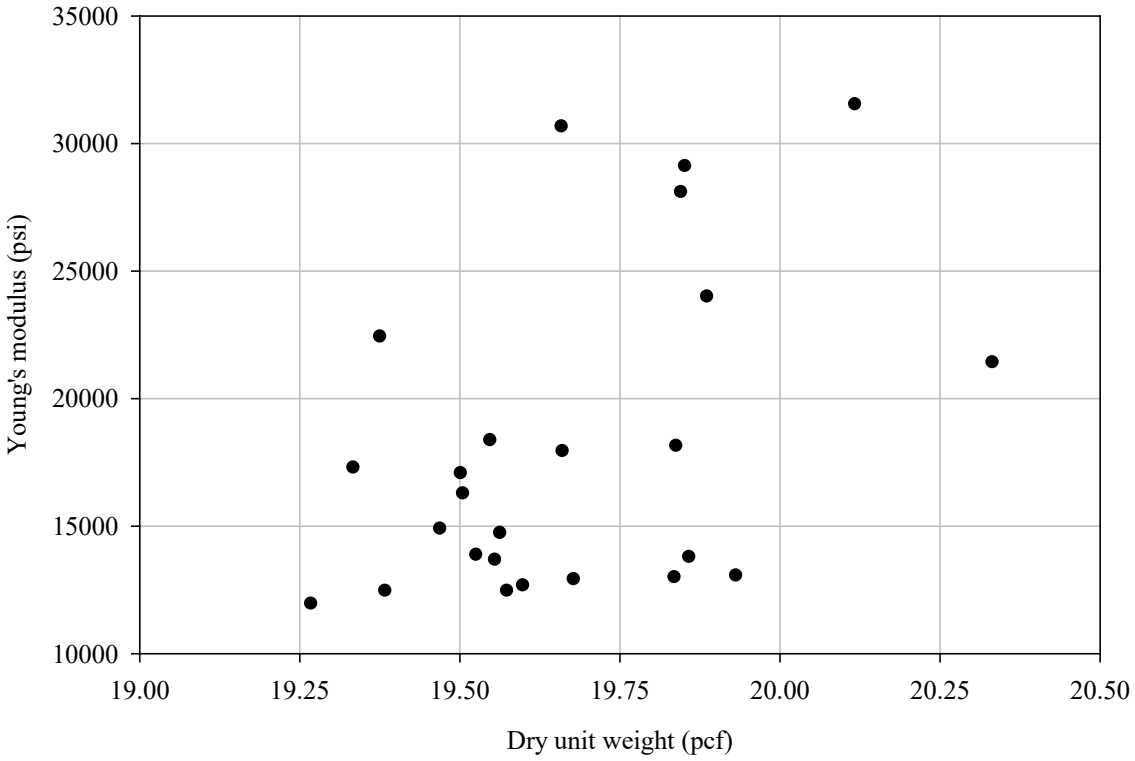

Figure 47. Young's modulus of the LCC specimens as a function of dry unit weight.

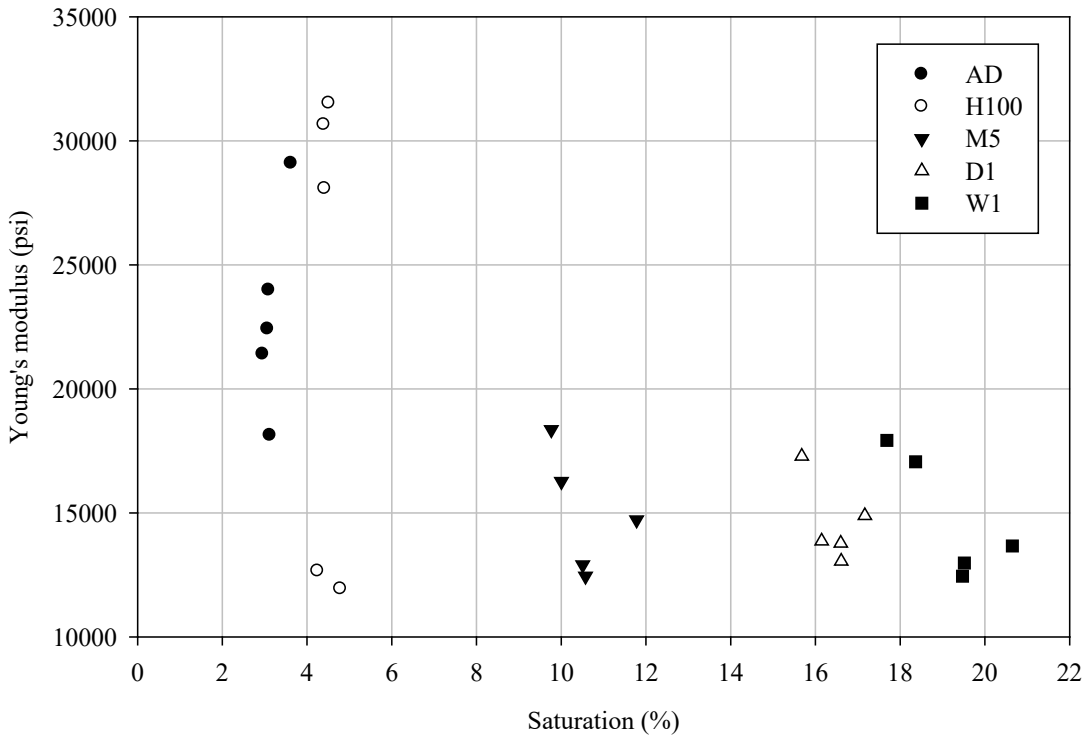

Figure 48. Young's modulus of the LCC specimens as a function of saturation.

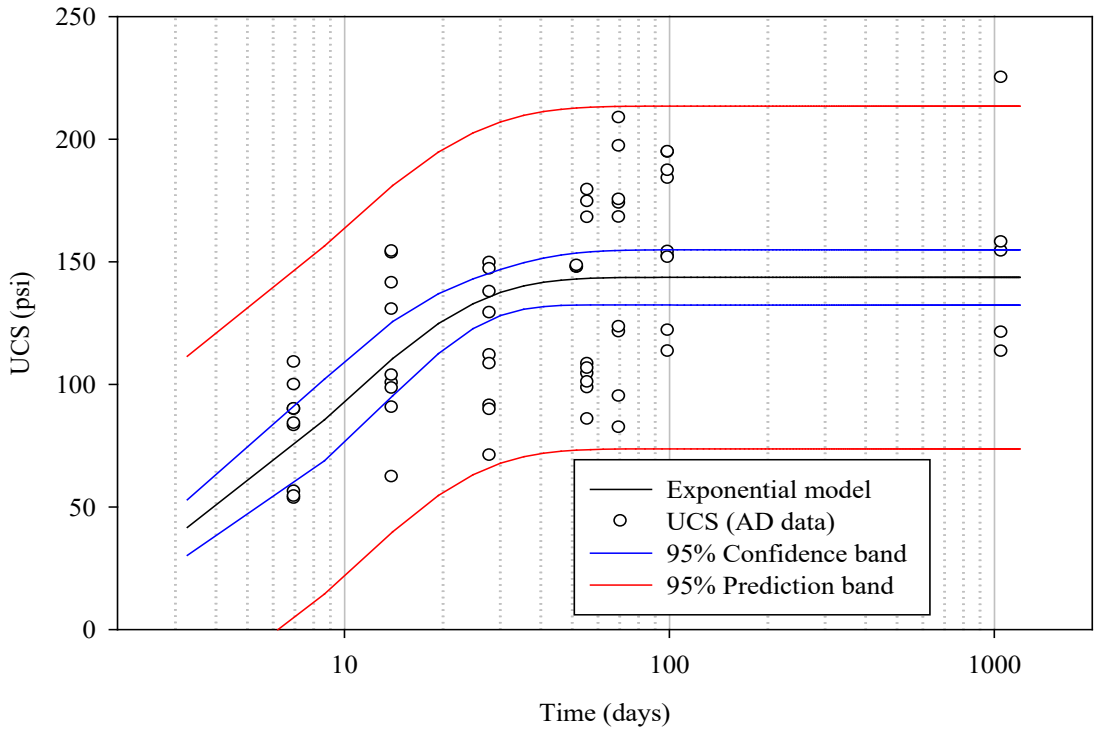

Figure 49. Unconfined compressive strength as a function of curing time and the regression model (Equation 20) with confidence and prediction bands.

CHAPTER 7

DRAINED TRIAXIAL COMPRESSIVE STRENGTH

Some advantages of the triaxial strength tests include allowance for back-pressure saturation (as discussed in Chapter 4), consolidation of the test specimen, and both drained and undrained conditions during the shearing phase. The consolidation conditions can closely replicate field conditions and be in isotropic, anisotropic, or K_0 configurations. Shearing of the test specimen can mimic most field conditions encountered in engineering projects, such as axial compression, axial extension, lateral compression, or lateral extension. The equipment required to perform the tests is much less ubiquitous than the UCS test equipment but is relatively common in specialized geotechnical testing laboratories. Proper test performance requires more advanced training and time than the UCS test and, therefore, is more costly.

One objective of this study was to estimate the strength of LCC in terms of the Mohr-Coulomb strength envelope derived from the CIDTx. The triaxial data are also utilized to correlate to the RM as a surrogate test. Another objective of this study was to determine the effects of the degree of saturation on the triaxial compressive strength of LCC. A series of CIDTx were performed to achieve this objective. The series included test specimens with ages ranging from 1,052 to 1,077 days and at various saturation treatments, as discussed in Chapter 3. This program included seven specimens from the

AD, H100, M5, D1, and W1 saturation groups, respectively. The range of nominal effective confinement ranged from three to 12 psi. All triaxial tests in this series were performed promptly after the completion of RM testing without removing the test specimen from the triaxial cell.

Methods

The specimens for triaxial testing were prepared as described in Chapter 2. The tests were performed on a calibrated GEOTAC triaxial system comprising a triaxial cell, a DigiFlow flow pump, and a Sigma-1 load frame, as shown in Figure 50. The CIDTx compression testing was performed in general accordance with ASTM D7181 (ASTM D18 Committee 2020). The test specimens were previously prepared in a triaxial cell for RM testing. The triaxial cell was filled with de-aired water and placed in the triaxial load frame. The typical saturation phase was omitted from the testing protocol, and the prescribed effective confining stress was applied. During consolidation, the volumetric and axial strain data are logged and plotted for a time-rate of strain analysis to determine an appropriate strain rate. Both Taylor and Casagrande's methods were used to analyze the time rate data. It was found that t_{90}, the time at which 90% of the consolidation occurred, was reached in less than two minutes for the consolidation phase. The strain rate, $\dot{\varepsilon}$, for the shearing phase of the tests was estimated at 0.2%/minute by:

$$\dot{\varepsilon} = \frac{4\%}{10 \cdot t_{90}} \qquad 23$$

The specimens were sheared in a drained condition with the specimen valves open to the atmosphere. Volumetric strain during shearing was determined by the axial displacement, the known area of the loading piston, and the volume change in the cell.

The specimens were sheared to 15% axial strain before termination of the test. Following testing, the failed specimens were placed in a convection oven at 230° F for water content determination.

Results

The results from the triaxial Young's modulus of the LCC specimens as a function of saturation, as a function of the effective confining stress, and as a function of the dry unit weight are shown in Figure 51, Figure 52, and Figure 53, respectively. Like the UCS tests results, most of the test specimens exhibited either an initial reduction in strength before the peak stress or a strong deviation from the initial straight-line portion of the stress-strain curve. At this initial yield stress, the mean Poisson's ratio for all test specimens was 0.231 with a standard deviation of 0.0412. The mean axial strain to reach the initial yield stress was 0.268% with a standard deviation of 0.0847%. At the peak yield stress, which is beyond the elastic range and into the plastic deformation range, the mean ratio of the axial strain to the lateral strain (the pseudo-Poisson's ratio) for all test specimens was 0.0814 with a standard deviation of 0.0635. The mean axial strain to reach the peak yield stress was 4.27% with a standard deviation of 3.27%. The results of the initial yield stress and peak yield stress in triaxial compression of the LCC specimens as a function of the effective confining stress and as a function of saturation are shown in Figure 54 and Figure 55, respectively.

The Mohr's circles for the initial yield and the peak stress are plotted in Figure 56 and Figure 57, respectively. The complete test reports from each of the triaxial tests are attached in Appendix E.

Discussion

The Young's modulus in triaxial compression, as seen in Figure 51, Figure 52, and Figure 53, is affected by the saturation, the dry unit weight, and to a lesser effect, the effective confining stress. The data shown in these figures are used in model generation using multilinear regression and are discussed in Chapter 8.

The increase in modulus with an increase in dry unit weight is expected as previously discussed in Chapter 6. The effect on the modulus from saturation indicates a greater influence than the minimal impact observed from the effective confining stress. This is partially explained by the effects on the matric suction and localized excess pore pressure within the specimen as the degree of saturation increases, as discussed in Chapter 6. This decrease in matric suction contributes to the decrease in stiffness measured in the LCC by reducing internal tensile stresses. Also, due to the increased strain rate (compared to the RM testing), the large deformation (again, compared to the RM testing), and the distortion of the fabric, there is likely an effect from the increase in pore water pressure in the occluded or tightly bound water-filled voids (see Figure 31, for example). Although the test is performed in a drained condition during shearing, the localized excess pore water pressure is a result of a partially drained state, resulting in a complex distribution of effective stress during shearing.

The strength in triaxial compression, as seen in Figure 54 and Figure 55 has a minor effect from the effective confining stress and a more pronounced effect from the degree of saturation. The trends from these to independent variables follow those seen for the triaxial Young's modulus.

The effective friction angles, as shown in Figure 56 and Figure 57 are 65.0° and 67.1° for the initial yield stress state and the peak strength, respectively. The effective cohesion intercept for each case is zero. This indicates a purely frictional material in the range of stresses tested in this study, which is relatively low. Tiwari et al. (2017) have suggested a conservative value for the effective friction angle of 35° be used for saturated design purposes. The authors have also reported that the partially saturated friction angle of 40° was obtained through direct shear testing, but the degree of saturation for this test is unknown. The authors suggest that the effective friction angle for design may be increased to 40° for Class-II or Class-IV LCC when subjected to normal stresses less than 1,000 kPa (145 psi). Considering the range of effective confining stresses for this study (three to 12 psi), and considering the findings from Tiwari et al. (2017), the use of the effective friction angle of 65.0° is reasonable for partially saturated conditions in the low range of stresses used in this study.

The mean Poisson's ratio, ν, of 0.231 results in an at-rest lateral earth pressure, K_0, of 0.3 by the following relationship,

$$K_0 = \frac{\nu}{1-\nu} \qquad 24$$

Figure 50. Photo of the triaxial testing apparatus with a test specimen in the triaxial cell.

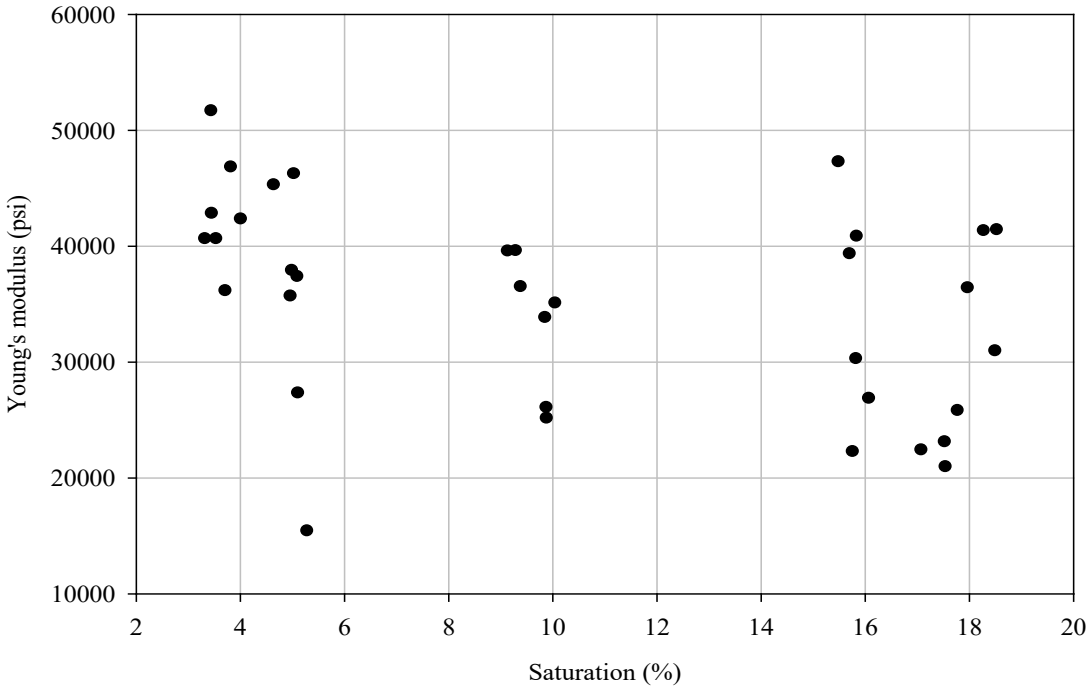

Figure 51. Triaxial Young's modulus of the LCC specimens as a function of saturation.

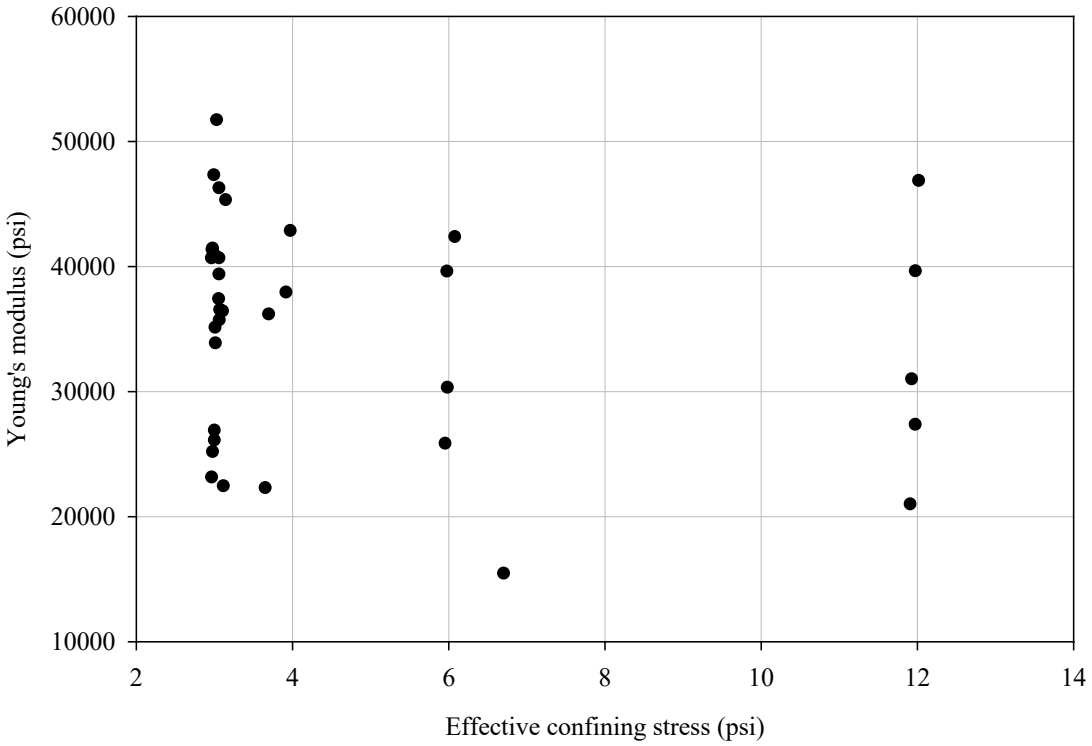

Figure 52. Triaxial Young's modulus of the LCC specimens as a function of the effective confining stress.

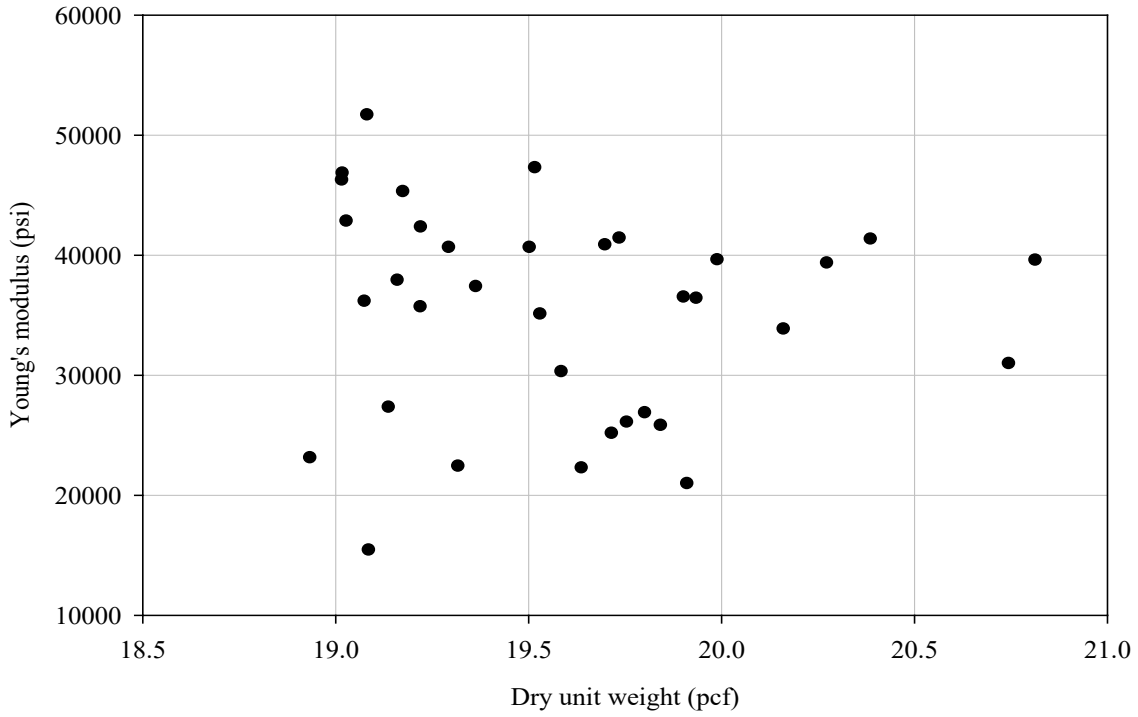

Figure 53. Triaxial Young's modulus of the LCC specimens as a function of the dry unit weight.

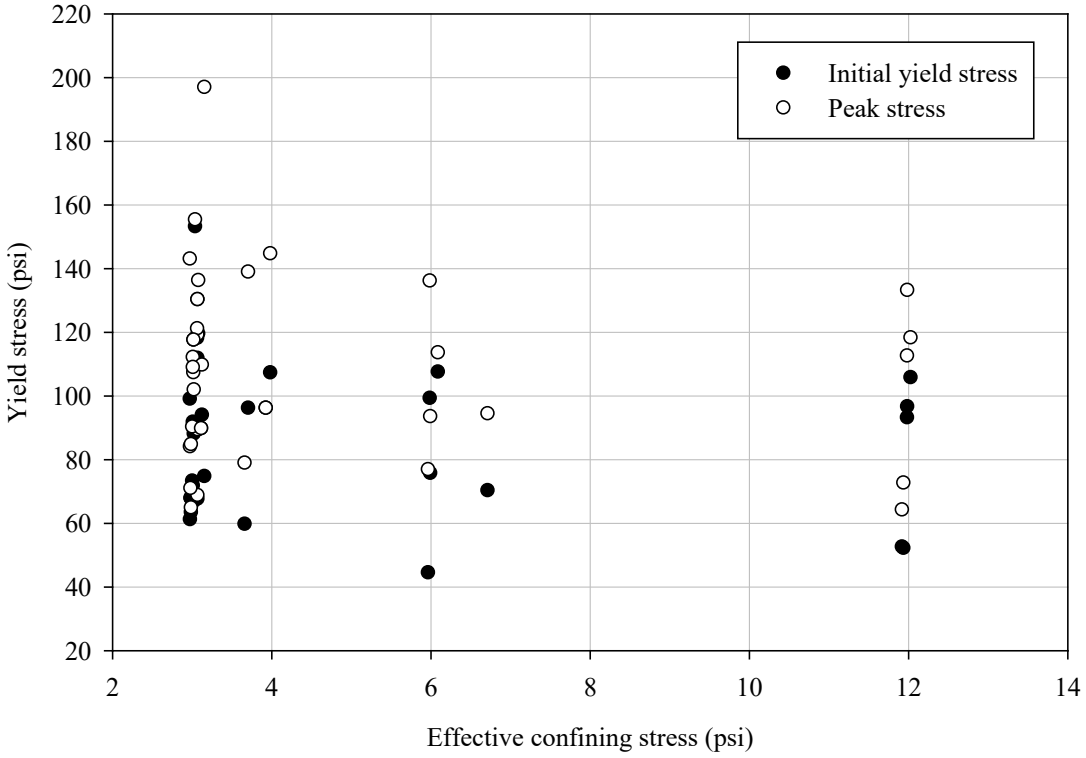

Figure 54. Yield stresses in triaxial compression of the LCC specimens as a function of the effective confining stress.

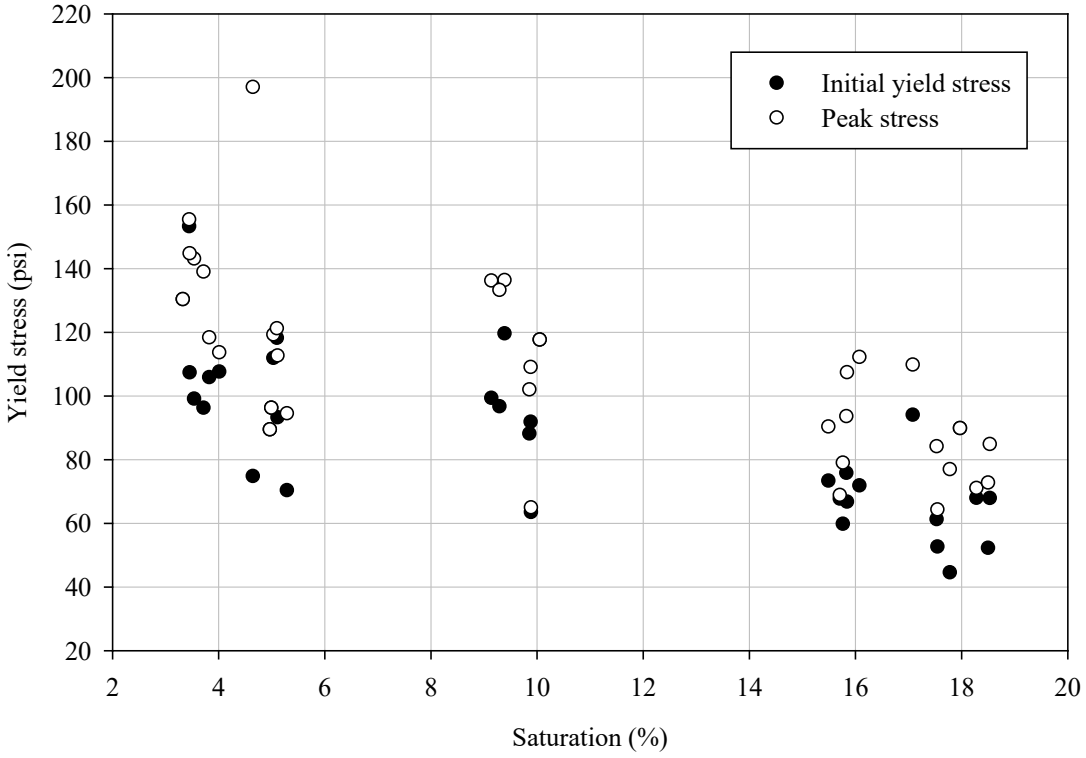

Figure 55. Yield stresses in triaxial compression of the LCC specimens as a function of saturation.

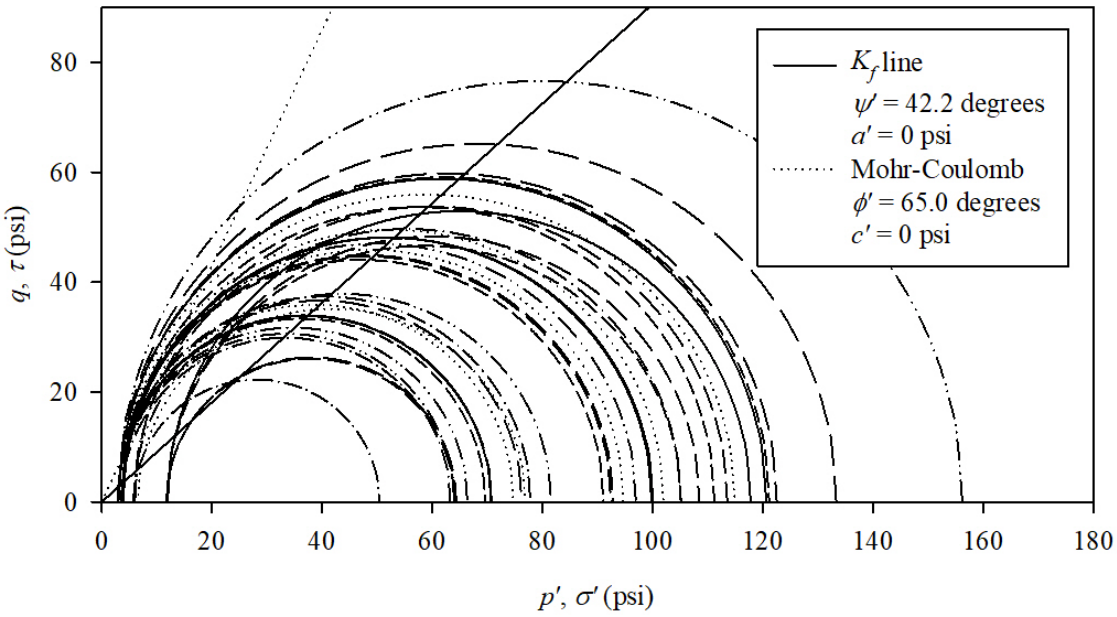

Figure 56. Mohr's circles, K_f line, and Mohr-Coulomb failure envelope for the initial yield points for all triaxial tests.

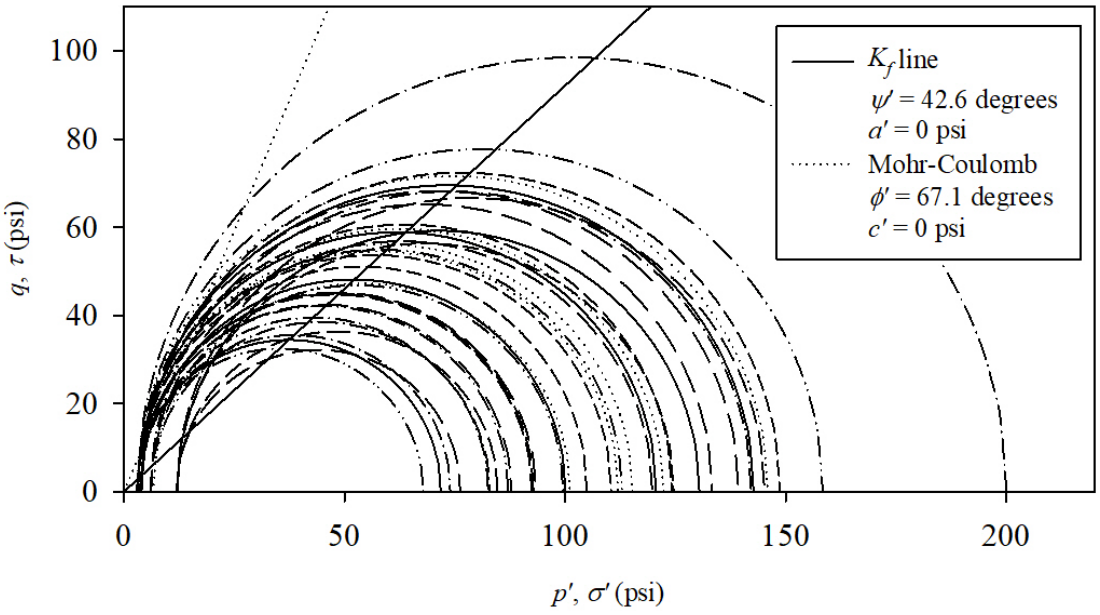

Figure 57. Mohr's circles, K_f line, and Mohr-Coulomb failure envelope for the peak stress points for all triaxial tests.

CHAPTER 8

LCC PREDICTIVE MODELS

One objective of the current research was to develop predictive models for estimating the engineering behavior of LCC and the effects of the degree of saturation. In addition, multiple linear regression analysis (MLR) models were developed to assess the potential correlation of RM test results with those obtained from the UCS and CIDTx compression tests. These latter models were correlated with the RM test results using paired UCS and CIDTx compression tests performed on the same respective specimens. If successful, these correlations will enable the estimation of RM results using relatively straightforward, less expensive, and ready-available UCS and CIDTx compression tests.

The data presented in the previous chapters were used to perform statistical analyses to evaluate the relationship between the independent variables (i.e., predictor variables) and the dependent variable (i.e., variable to be estimated) using MLR and simple linear regression (SLR). Regression analysis aims to develop a predictive best-fit statistical model that may be used to calculate the value of a dependent variable from one or more independent variables (Levine et al. 2001).

This chapter used two regression methods: SLR (i.e., regression using a single independent variable) and MLR (i.e., regression using multiple independent variables). The SLR and MLR regression analyses were performed using Microsoft Excel with the

Analysis ToolPak, which uses the least-square method to minimize the sum of the squares (i.e., variance) between the dependent and independent variables using linear relationships or relationships that can be linearized by transformation of the dependent or independent variables, or both. Closed-form matrix operations are used to solve for the best-fit coefficients of the system of linear equations. The general form of the SLR model is,

$$Y_i = \beta_0 + \beta_1 \cdot X_i + \varepsilon_i \qquad 25$$

where Y_i is the predictive value of the dependent variable, Y, for observation, i, β_0 is the Y-intercept parameter, β_1 is the slope parameter, and X_i represents the independent variables, X. The value of ε_i is the random error in Y for observation i (Levine et al. 2001). The general form of the MLR model is,

$$Y_i = \beta_0 + \beta_1 \cdot X_{1i} + \beta_2 \cdot X_{2i} + \beta_3 \cdot X_{3i} + \cdots + \beta_k \cdot X_{ki} + \varepsilon_i \qquad 26$$

where $\beta_1 \ldots \beta_k$ are the partial slopes (i.e., partial derivatives) for their respective X variables (Levine et al. 2001).

Three essential assumptions are needed for valid SLR and MLR regression analyses. The first assumption, normality of error, requires the error values to be normally distributed and centered around the best-fit regression line in n^{th} dimensional space. The second assumption, homoscedasticity, requires the variation about the best-fit line to be constant across all values of X_i. The final assumption, independence of errors, requires the errors to be independent (i.e., not correlated) with all values of X_i (Levine et al. 2001).

Residual error plots can be used to judge the validity of the above assumptions. The residual error is plotted by the difference from the best-fit Y values for each X_i value. This plotting is done separately for each independent variable. The overall quality of the regression model is generally judged by the magnitude of the coefficient of determination, $R^{2,}$ and the magnitude of the standard error, s_e, as well as an inspection of the analysis of variance (ANOVA) table. For example, an R^2 value of 1.00 means that the X_i values explain 100 percent of the variability in the Y value (i.e., a "perfect" fit).

Similarly, an R^2 value of 0.60 means that 60 percent of the variability is explained by the X_i values, etc. The value of s_e measures the standard deviation of the errors in a regression model. The model's standard error is a measure of the average deviation or dispersion of the points on the residual error scatter plot around the best-fit line. An ANOVA table is used to judge if the partial slopes ($\beta_1 \ldots \beta_k$) are statistically significant using the F-statistic and its corresponding p-value. For this test, the null hypothesis is that β_i is zero (i.e., not significant). For this research, an acceptance criterion of the alternative hypothesis that β_i is non-zero was a 95% confidence with a p-value < α = 0.05.

Unconfined Compressive Strength Models

The data shown in Figure 45 and Figure 46 in Chapter 6 were used to generate the following model to estimate the UCS of LCC as a function of the dry unit weight, γ_d, in pcf, and the degree of saturation, S, in percent,

$$UCS = \frac{1}{\beta_0 + \beta_1 \cdot \gamma_d^2 + \beta_2 \cdot \ln(S)} \qquad 27$$

The range of use with statistical significance for γ_d and S in Equation 27 is limited to 18.9 pcf to 20.8 pcf and 2.9% to 20.5%, respectively. A summary of the regression results for Equation 27 are shown in Table 14. The regression statistics and ANOVA results for Equation 27 are shown in Table 15.

The data shown in Figure 45 and Figure 46 in Chapter 6 were used to generate the following model to estimate the initial yield for the UCS test, IY_{UCS}, of LCC as a function of γ_d in pcf, and S in percent,

$$IY_{UCS} = min\left(\begin{array}{c}(\beta_3 + \beta_4 \cdot \ln(\gamma_d) + \beta_5 \cdot S)^2, \\ \frac{1}{\beta_0 + \beta_1 \cdot \gamma_d^2 + \beta_2 \cdot \ln(S)}\end{array}\right) \quad 28$$

As with Equation 27, the range of use with statistical significance for γ_d and S in Equation 28 is limited to the ranges of 19.3 pcf to 20.3 pcf and 2.9% to 20.5%, respectively. A summary of the regression results for Equation 28 are shown in Table 16. The regression statistics and ANOVA results for Equation 28 are shown in Table 17. No statistically significant correlation was found for the UCS or IY_{UCS} with the height-to-diameter ratio, $R_{H:D}$, for the test specimens.

The data shown in Figure 46 in Chapter 6 were used to generate the following model to estimate the modulus of elasticity, E_{UCS}, of LCC as a function of the degree of saturation, S, in percent,

$$E_{UCS} = \left(\beta_6 + \beta_7 \cdot \ln(S)\right)^2 \quad 29$$

The range of use with statistical significance for S in Equation 29 is limited to the range of 2.9% to 20.5%. A summary of the regression results for Equation 29 are shown in Table 18. The regression statistics and ANOVA results for Equation 29 are shown in

Table 19. No statistically significant correlation was found for the E_{UCS} with γ_d or $R_{H:D}$ for the test specimens.

Drained Triaxial Compressive Models

The data shown in Figure 52 and Figure 53 in Chapter 7 were used to generate the following model to estimate the modulus of elasticity in triaxial compression, E_{TX}, of LCC as a function of the effective confining stress, σ'_3, in psi and γ_d, in pcf,

$$E_{TX} = e^{\frac{\beta_8 \cdot \sigma'_3 + \beta_9 \cdot \sigma'_3 \cdot \ln(S) + \beta_{10} + \beta_{11} \cdot \sigma'_3 \cdot \sqrt{\gamma_d}}{\sigma'_3}} \quad (30)$$

The range of use with statistical significance for σ'_3 and γ_d, in Equation 30 is limited to 3.0 psi to 12.0 psi to 18.9 pcf to 20.8 pcf, respectively. A summary of the regression results for Equation 30 are shown in Table 20. The regression statistics and ANOVA results for Equation 30 are shown in Table 21. No statistically significant correlation was found for the E_{TX} with S or $R_{H:D}$ for the test specimens.

The data shown in Figure 54 and Figure 55 in Chapter 7 were used to generate the following models to estimate the initial yield of the deviator stress, $\sigma_{d.i}$, and the maximum deviator stress, $\sigma_{d.max}$ for the triaxial compression test, of LCC as a function of σ'_3 in psi and S in percent,

$$\sigma_{d.i} = e^{\frac{\beta_{12} \cdot \ln(\sigma'_3) + \beta_{13} \cdot \ln(\sigma'_3) \cdot \ln(S) + \beta_{14}}{\ln(\sigma'_3)}} \quad (31)$$

$$\sigma_{d.max} = \beta_{15} + \beta_{16} \cdot \frac{1}{\sigma_{d.i}} \quad (32)$$

where $\sigma_{d.i}$ in Equation 32 is the prediction obtained from Equation 31. The range of use with statistical significance for, σ'_3, and S, in Equation 31 and Equation 32 are limited to

the ranges of 3.0 psi to 12.0 psi to 13.3% to 18.5%, respectively. A summary of the regression results for Equation 31 are shown in Table 22. The regression statistics and ANOVA results for Equation 31 are shown in Table 23. A summary of the regression results for Equation 32 are shown in Table 24. The regression statistics and ANOVA results for Equation 32 are shown in Table 25. No statistically significant correlation was found for the $\sigma_{d.i}$ or $\sigma_{d.max}$ with γ_d or $R_{H:D}$ for the test specimens.

Resilient Modulus Models

The residual plots from the regression process revealed a testing artifact in the data attributed to the test specimens' height-to-diameter ratio, $R_{H:D}$, which is also shown in Figure 40. Because the goal of the predictive model was to be used to estimate RM sans the test procedure, a decision was made to remove the effects from the testing artifact from the data for the standalone MR model.

Regression analysis can eliminate specific artifact effects from estimates of our independent variable by adjusting the *Y* values (Ostle and Malone 1988). In this case, a linear regression was performed with the independent variable in the desired transformation, 1/*MR*, and with the dependent variable, which is the source of the artifact effect, $R_{H:D}$. The regression is in the form of Equation 33, where b_{17} is the intercept (not used in the correction) and b_{18} is the slope of the line. The independent variable is adjusted as follows,

$$M_{R.adjusted} = \frac{1}{\frac{1}{M_{R.raw}} - b_{18}(R_{H:D} - \overline{R_{H:D}})} \qquad 33$$

where $\overline{R_{H:D}}$ is the mean height-to-diameter ratio. A summary of the regression results for Equation 33 are shown in Table 26. The regression statistics and ANOVA results for Equation 33 are shown in Table 27.

The data shown in Figure 36, Figure 37, and Figure 38 in Chapter 5 were used to generate the following model to estimate the RM, M_R, of LCC as a function of the confining stress, σ_3, in psi and γ_d, in pcf and deviator stress, σ_d, in psi,

$$M_R = \frac{1}{\beta_{19} + \beta_{20} \cdot \ln(\sigma_3) + \beta_{21} \cdot \gamma_d^2 + \beta_{22} \cdot \ln(\sigma_d)} \quad 34$$

The range of use with statistical significance for σ_3, γ_d, and σ_d in Equation 34 is limited to 1.7 psi to 20.1 psi, 18.9 pcf to 20.8 pcf, and 2.9 psi to 40.7 psi, respectively. A summary of the regression results for Equation 34 are shown in Table 28. The regression statistics and ANOVA results for Equation 34 are shown in Table 29. No statistically significant correlation was found between *MR* and *S* for the test specimens.

Surrogate Test Models

The UCS and CIDTx compression tests were performed following the RM tests, providing a direct test comparison without introducing specimen effects. The data from the RM tests and the subsequent UCS test were used to generate the following model to estimate the RM, M_R, of LCC as a function of the confining stress, σ_3, in psi, γ_d, in pcf, modulus of elasticity from the UCS test, E_{UCS}, in psi, and the degree of saturation, S, in percent,

$$M_R = \frac{1}{\beta_{23} + \beta_{24} \cdot \ln(\sigma_3) + \beta_{25} \cdot \gamma_d^2 + \beta_{26} \cdot E_{UCS}^2 + \beta_{27} \cdot \ln(S)} \quad 35$$

The range of use with statistical significance for σ_3, γ_d, E_{USC}, and S in Equation 35 is limited to the ranges of 1.7 psi to 20.1 psi, 19.3 pcf to 20.3 pcf, 11,940 psi to 31,520 psi, and 2.9% to 20.5%, respectively. A summary of the regression results for Equation 35 is shown in Table 30. The regression statistics and ANOVA results for Equation 35 are shown in Table 31.

The data from the RM tests and the subsequent CIDTx compression tests were used to generate the following model to estimate the RM, M_R, of LCC as a function of the confining stress, σ_3, in psi, modulus of elasticity from the UCS test, E_{TX}, in psi, the effective confining stress from the triaxial test, $\sigma'_{3.TX}$, in psi and γ_d, in pcf,

$$M_R = \frac{1}{\beta_{28} + \beta_{29} \cdot \ln(\sigma_3) + \beta_{30} \cdot \ln(E_{TX}) + \beta_{31} \cdot \ln(\sigma'_{3.TX}) + \beta_{32} \cdot \sqrt{\gamma_d}} \quad 36$$

The range of use with statistical significance for σ_3, E_{TX}, $\sigma'_{3.TX}$, and γ_d, in Equation 36, is limited to 1.7 psi to 20.1 psi, 15,410 psi to 51,660 psi, 3.0 psi to 12.0 psi, 18.9 pcf to 20.8 pcf, respectively. A summary of the regression results for Equation 36 are shown in Table 32. The regression statistics and ANOVA results for Equation 36 are shown in Table 33.

Table 14. Summary of the regression results for Equation 27.

Statistic	Regression coefficient	Standard Error	*t*-statistic	*p*-value
b_0	4.035E-02	1.438E-02	2.805	0.01032
b_1	-9.181E-05	3.609E-05	-2.544	0.01850
b_2	2.229E-03	4.997E-04	4.461	0.00020

Table 15. Regression statistics and ANOVA results of Equation 27.

Multiple R	0.8017
R square	0.6428
Adjusted R square	0.6103
Standard error	0.001643
Observations	25

Variation source	Degrees of freedom	Sum of squares	Mean square	*F*-statistic	*p*-value
Regression	2	1.07E-04	5.343E-05	19.79	1.209E-05
Residual	22	5.94E-05	2.700E-06		
Total	24	1.66E-04			

Table 16. Summary of the regression results for Equation 28.

Statistic	Regression coefficient	Standard Error	*t*-statistic	*p*-value
b_3	-118.3	62.85	-1.882	0.0732
b_4	43.66	21.05	2.074	0.0499
b_5	-0.1419	0.04243	-3.345	0.002931

Table 17. Regression statistics and ANOVA results of Equation 28.

Multiple R	0.7017
R square	0.4924
Adjusted R square	0.4463
Standard error	1.258
Observations	25

Variation source	Degrees of freedom	Sum of squares	Mean square	*F*-statistic	*p*-value
Regression	2	33.79	16.90	10.67	5.760E-04
Residual	22	34.83	1.583		
Total	24	68.63			

Table 18. Summary of the regression results for Equation 29.

Statistic	Regression coefficient	Standard Error	*t*-statistic	*p*-value
b_6	173.8	10.91	15.93	6.412E-14
b_7	-19.150	4.843	-3.954	6.300E-04

Table 19. Regression statistics and ANOVA results of Equation 29.

Multiple R	0.6362
R square	0.4047
Adjusted R square	0.3788
Standard error	17.06
Observations	25

Variation source	Degrees of freedom	Sum of squares	Mean square	*F*-statistic	*p*-value
Regression	1	4549	4549	15.64	6.300E-04
Residual	23	6691	290.9		
Total	24	1.124E+04			

Table 20. Summary of the regression results for Equation 30.

Statistic	Regression coefficient	Standard Error	*t*-statistic	*p*-value
b_8	1.687	4.249	0.3969	6.941E-01
b_9	-0.2835	0.08385	-3.381	1.966E-03
b_{10}	0.9402	0.4511	2.084	4.549E-02
b_{11}	2.059	0.9798	2.102	4.381E-02

Table 21. Regression statistics and ANOVA results of Equation 30.

Multiple R	0.5568
R square	0.3100
Adjusted R square	0.2433
Standard error	0.2438
Observations	35

Variation source	Degrees of freedom	Sum of squares	Mean square	*F*-statistic	*p*-value
Regression	3	0.8276	0.2759	4.643	8.557E-03
Residual	31	1.842	0.05942		
Total	34	2.670			

Table 22. Summary of the regression results for Equation 31.

Statistic	Regression coefficient	Standard Error	*t*-statistic	*p*-value
b_{12}	4.860	0.1716	28.327	3.119E-24
b_{13}	-0.3204	0.05223	-6.135	7.348E-07
b_{14}	0.3563	0.1730	2.060	4.758E-02

Table 23. Regression statistics and ANOVA results of Equation 31.

Multiple R	0.7475
R square	0.5587
Adjusted R square	0.5311
Standard error	0.1947
Observations	35

Variation source	Degrees of freedom	Sum of squares	Mean square	*F*-statistic	*p*-value
Regression	2	1.536	0.7680	20.26	2.067E-06
Residual	32	1.213	0.03791		
Total	34	2.749			

Table 24. Summary of the regression results for Equation 32.

Statistic	Regression coefficient	Standard Error	*t*-statistic	*p*-value
b_{15}	208.1	20.60	10.10	1.249E-11
b_{16}	-8498	1717	-4.948	2.151E-05

Table 25. Regression statistics and ANOVA results of Equation 32.

Multiple R	0.6526
R square	0.4259
Adjusted R square	0.4085
Standard error	22.61
Observations	35

Variation source	Degrees of freedom	Sum of squares	Mean square	*F*-statistic	*p*-value
Regression	1	1.251E+04	1.251E+04	24.48	2.151E-05
Residual	33	1.687E+04	511.2		
Total	34	2.938E+04			

Table 26. Summary of the regression results for Equation 33.

Statistic	Regression coefficient	Standard Error	*t*-statistic	*p*-value
b_{17}	-6.449E-05	2.118E-05	-3.045	2.394E-03
b_{18}	4.459E-05	1.133E-05	3.937	8.889E-05

Table 27. Regression statistics and ANOVA results of Equation 33.

Multiple R	0.1303
R square	0.0170
Adjusted R square	0.0159
Standard error	8.384E-06
Observations	900

Variation source	Degrees of freedom	Sum of squares	Mean square	*F*-statistic	*p*-value
Regression	1	1.089E-09	1.089E-09	15.50	8.889E-05
Residual	898	6.312E-08	7.029E-11		
Total	899	6.421E-08			

Table 28. Summary of the regression results for Equation 34.

Statistic	Regression coefficient	Standard Error	*t*-statistic	*p*-value
b_{19}	6.718E-05	5.760E-06	11.66	2.316E-29
b_{10}	-6.565E-06	4.502E-07	-14.58	2.171E-43
b_{21}	-1.016E-07	1.476E-08	-6.886	1.077E-11
b_{22}	1.702E-06	5.119E-07	3.325	9.206E-04

Table 29. Regression statistics and ANOVA results of Equation 34.

Multiple R	0.5397
R square	0.2912
Adjusted R square	0.2889
Standard error	7.066E-06
Observations	900

Variation source	Degrees of freedom	Sum of squares	Mean square	*F*-statistic	*p*-value
Regression	3	1.838E-08	6.127E-09	122.7	1.364E-66
Residual	896	4.473E-08	4.933E-11		
Total	899	6.312E-08			

Table 30. Summary of the regression results for Equation 35.

Statistic	Regression coefficient	Standard Error	*t*-statistic	*p*-value
b_{23}	8.576E-05	1.711E-05	5.012	8.382E-07
b_{24}	-6.471E-06	5.005E-07	-12.93	8.208E-32
b_{25}	-1.097E-07	4.392E-08	-2.497	1.295E-02
b_{26}	-1.021E-14	1.984E-15	-5.145	4.343E-07
b_{27}	-2.894E-06	6.955E-07	-4.161	3.941E-05

Table 31. Regression statistics and ANOVA results of Equation 35.

Multiple R	0.6044
R square	0.3653
Adjusted R square	0.3584
Standard error	7.380E-06
Observations	375

Variation source	Degrees of freedom	Sum of squares	Mean square	*F*-statistic	*p*-value
Regression	4	1.160E-08	2.899E-09	53.2	2.064E-35
Residual	370	2.015E-08	5.446E-11		
Total	374	3.174E-08			

Table 32. Summary of the regression results for Equation 36.

Statistic	Regression coefficient	Standard Error	*t*-statistic	*p*-value
b_{28}	2.184E-04	2.870E-05	7.612	1.275E-13
b_{29}	-2.648E-06	4.721E-07	-5.609	3.309E-08
b_{30}	-3.885E-06	1.170E-06	-3.320	9.623E-04
b_{31}	-1.560E-06	6.631E-07	-2.352	1.905E-02
b_{32}	-3.411E-05	5.860E-06	-5.820	1.032E-08

Table 33. Regression statistics and ANOVA results of Equation 36.

Multiple R	0.3702
R square	0.1371
Adjusted R square	0.1304
Standard error	7.228E-06
Observations	525

Variation source	Degrees of freedom	Sum of squares	Mean square	*F*-statistic	*p*-value
Regression	4	4.314E-09	1.079E-09	20.65	8.300E-16
Residual	520	2.716E-08	5.224E-11		
Total	524	3.148E-08			

CHAPTER 9

CONCLUSIONS

LCC is increasingly utilized in geotechnical applications, particularly in roadway projects. Typical LCC applications for these projects include use as flowable fill, retaining wall backfill, and vertical stress reduction as large inclusions in earthen embankments. The data presented in the literature for LCC is relatively sparse and is based mainly on the unconfined compression test in a dry state or, in some limited cases, a confined state and either dry or fully saturated. Observations from the dry vs. saturated test data indicate a transition from a brittle failure behavior in the dry state to an elastoplastic failure behavior at full saturation. Additionally, increasing confinement has shown (1) no conclusive effect on the hydraulic conductivity, and in some cases, (2) a decrease in the initial yield stress has been observed. In addition, no studies or data are presented in the literature on the use of LCC in pavement sections as a base or subbase material for roadways. LCC is typically deployed in a buried configuration in roadway and other applications where partial saturation is inevitable. Therefore, the in-situ LCC will experience partial saturation and significant differences in the principal stresses resulting from the applied live and dead loads.

This study's experimental findings and evaluations are based on a Type I LCC using an extensive laboratory testing program with various partial saturation treatments,

resulting in partial saturation degrees ranging from 2.8% to 20.4%. A high-humidity environment experiment yielded a minimum of 9.5% long-term saturation to represent field conditions above the water table.

We found that an initial curing period of approximately 70 days is required for the LCC to reach a reasonable steady state condition. This finding is based on a series of dry UCS tests carried out as a function of curing time. Normalizing our data to the 70-day strength allowed for reasonable comparisons, thus preventing erroneous comparisons and interpretations and providing a long-term strength value for design.

The RM tests were performed under a nominal range of confinement from three psi to 20 psi and a nominal deviatoric stress range from three psi to 40 psi, which are typical test ranges for base and subbase materials. The average RM was 71 ksi, which is comparable to the compacted granular materials results of Davich et al., (2004). We note that the RM results were somewhat affected by sample confinement but not significantly affected by increasing saturation. From these data, we developed an RM regression model for estimating the RM as a function of the confining stress, deviatoric stress, and dry unit weight. Our favorable RM results suggest that LCC can be used as a base or subbase material over the range of saturation and stress conditions explored in this study.

The UCS results ranged from about 80 to 200 psi at or after the 70-day cure time. This relatively high variability was seen across all saturation ranges and cure times. We believe that the source of the UCS is complex and primarily results from a combination of chemical bonding of the cement achieved during cement hydration and curing and a minor component from matric and osmotic suction. The UCS test results show that the unconfined strength and its modulus are reduced by increasing the degree of saturation,

but the effect is relatively minor. Nonetheless, we developed predictive models for estimating (1) the peak UCS, (2) initial yield stress, and (3) unconfined Young's modulus for LCC as a function of the dry unit weight and the degree of saturation.

However, we found that the degree of saturation significantly influences the strength and modulus in CIDTx compression, more so than the confinement effect. Previous research suggests that LCC should be viewed as a cohesionless material with an effective friction angle of up to 40° for normal stresses up to 145 psi. However, our data suggest zero cohesion and an effective friction angle of 65° for partially saturated conditions as a reasonable mean estimate for cases below 12 psi confinement. Further, we found a mean Poisson's ratio of 0.231 (i.e., at-rest lateral earth pressure coefficient of 0.3). These mean values are recommended for all degrees of saturation.

Predictive models were developed to estimate the confined-drained Young's modulus, initial yield, and peak deviatoric stresses. The confined Young's modulus for LCC is a function of the effective confining stress, the dry unit weight, and the degree of saturation. The yield stress models are a function of the effective confining stress and the degree of saturation.

We developed UCS and CIDTx compression test data to make a "surrogate" estimate of the RM for engineering practice. This development incorporated a height-to-diameter ratio correction. The UCS-RM surrogate model is a function of confining stress, dry unit weight, unconfined Young's modulus, and the degree of saturation. The CIDTx compression surrogate model is a function of the pavement confining stress, the confined Young's modulus, the triaxial effective confining stress, and the dry unit weight. The predictive models are suggested for preliminary engineering estimations and

are limited to the ranges presented for this study. For the final design, we encourage RM testing, as applicable, due to the variability of the LCC material and the relative importance of the project.

CHAPTER 10

IMPLEMENTATION AND FUTURE WORK

Implementation

The data set generated for this study is limited to Type I (Table 1) LCC of a particular mix design using the foaming agent and specimens provided by Aerix Industries (Figure 2). The reported Poisson ratio was 0.231, and the resulting K_0 was 0.3. The recommended effective friction angle of 65° with zero cohesion is a reasonable mean design estimate for confining pressures (i.e., σ'_3) at or below 12 psi. The drained friction angle and Poisson's ratio are essential for designing retaining walls, buried structures, culverts, tunnels, and slope stabilization projects.

Implementation and reliance on the MLR models presented for this study have limitations. The first and most narrow limitation is the cured dry unit of the LCC, which ranges from 18.9 pcf to 20.8 pcf. LCC mixes with higher densities have the potential to be stiffer and stronger, and our work may not produce representative design values for these mixes. The second limitation of the MLR models is the degree of saturation, which ranges from 2.8% to 20.4%. However, we believe that short of the complete inundation of the LCC for an extended period, the range of saturation we tested will likely cover the partially saturated conditions encountered in many, if not most, roadway and field applications. In addition, the RM testing was limited to the stress ranges shown in Table

12. The data from the CIDTx compression tests are limited to nominal effective confining stress from 2.5 psi up to 12 psi. However, these stress ranges are typical for base/subbase materials and moderately high retaining systems and embankments.

Further details of the limitations of each model are presented in Chapter 8, but the guidelines above are a reasonable summary. Lastly, engineering judgment should be exercised when utilizing the models and extrapolating beyond these limitations or for other uses and applications of LCC.

The RM and other engineering parameters change due to several factors, including water content, cyclic and static stress levels, volume change from freeze-thaw cycles, or temperature variations (Elliott and Thornton 1988). Thus, seasonal variations in the pavement sections or other engineered systems have the potential to impact the performance of LCC. Additionally, the interaction of LCC with adjacent materials possessing variability in engineering behavior resulting from (1) the imperfect repeatability of standardized laboratory test methods, (2) inherent variability in site soils, (3) differences in the individually constructed components, and (4) system variability including the loading variability will affect the design of the system (Yoder and Witczak 1975).

The models we presented in this dissertation describe the correlation between the dependent and independent variables and represent the best estimate fit (i.e., mean regression line) for the data collected. Although the utmost care was taken in specimen preparation, specimen mounting, and test methods, with the author having over 20 years of geotechnical laboratory testing experience, the results suggest a relatively high variability in RM results. From a pragmatic standpoint, the models allow designers to

evaluate the preliminary feasibility of utilizing Type I LCC in designing a pavement or other system. However, we recommend performing project-specific LCC testing for large projects or other critical applications or situations.

Methods to estimate the pavement's service life sensitivity to the inputted material properties and other potential variations (e.g., average annual daily traffic (AADT) and Equivalent Single Axle Load (ESALS) could formally be evaluated using Monte Carlo simulations combined with the concepts of reliability index and reliability analysis. These evaluations will provide the probability of failure (i.e., not meeting a serviceability limit state) during the desired service life of the pavement system.

Less formally, life-cycle evaluations could be completed using sensitivity analysis that evaluates the change in the projected service life of the pavement as a function of the capacity and demand input variables. For the case of the RM, the sensitivity evaluations might include the 70, 85, and 95 percent lower confidence intervals from the regression model estimate. These confidence intervals correspond to a 30, 15, and 5 percent probability that the input RM value is less than the actual, i.e., the true RM value. Estimates of these "lower bound" confidence intervals can be obtained by applying the Student's one-tailed *t*-test with alpha values corresponding to 0.30, 0.15, and 0.05, respectively. Further details of how to do this for multiple linear regression models are found in Draper and Smith (1998). The required statistic is the standard error of the RM regression model, s_e, calculated from the mean square error (MSE) of the residuals from the regression model. (The value of s_e from an MLR model is analogous to the standard deviation used in point statistics). As an example from this study, s_e is 7.066e-6 for Equation 34 (see Table 29).

Ultimately, based on this evaluation, the designer must decide what lower confidence interval to select as a "conservative" estimate RM and whether the projected service life is acceptable. If unacceptable performance is possible, then changes in the subbase, base, and pavement thickness or stiffness may be needed, or using a higher density of LCC with corresponding higher RM values may be warranted.

Future Work

Although the data set generated for this study is comprehensive, future work should include expansion of the data set based on the cured dry unit weight of the LCC to cover the spectrum of values presented in Table 1. Further investigation is also warranted to advance understanding of the role of excess pore pressure and matric suction for partially saturated LCC during monotonic and cyclic loading.

Regarding pavement systems, future work should include an instrumented field demonstration project for roadways or bridge approaches. Possible application(s) include LCC underneath a roadway pavement or a concrete bridge approach slab. Instrumentation of the project should consist of measurements of stress and strain and monitoring of permanent distress within the LCC and manifestations at the pavement surface. Since LCC is susceptible to freeze/thaw damage yet has good insulation properties, instrumentation should also include monitoring the temperature within the LCC to estimate long-term freeze/thaw performance. Also, the field demonstration project could consist of sections that cover the full range of LCC types.

Industry Standards

As the use of LCC increases in geotechnical applications, a standardized testing program should be established for LCC design. This standardization should include test specimen preparation procedures and expansion beyond UCS testing of air-dried samples. This study contributes significantly to developing methods for evaluating the effects of partial saturation and confinement on LCC's low and high-strain stiffness and strength properties.

As mentioned in this study, cast test specimens for LCC typically exhibit a "soft bottom," which may significantly affect laboratory testing results. Complete removal of this material is imperative for reasonable test result evaluation and comparison. The current standard Styrofoam molds create a nominal three-inch diameter by six-inch long specimen, which must be trimmed and squared. As discussed previously, the $R_{H:D}$ may affect the results from laboratory tests. It is recommended that the LCC industry employ a longer cast length of seven inches, allowing for the complete removal of the "soft bottom" and yielding a test specimen with an $R_{H:D}$ of at least two.

APPENDIX A

PARTIALLY SATURATED STATISTICAL ANALYSIS

See Appendix_A_Partially_Saturated_Statistics.pdf

APPENDIX B

CT IMAGES OF PARTIALLY SATURATED LCC

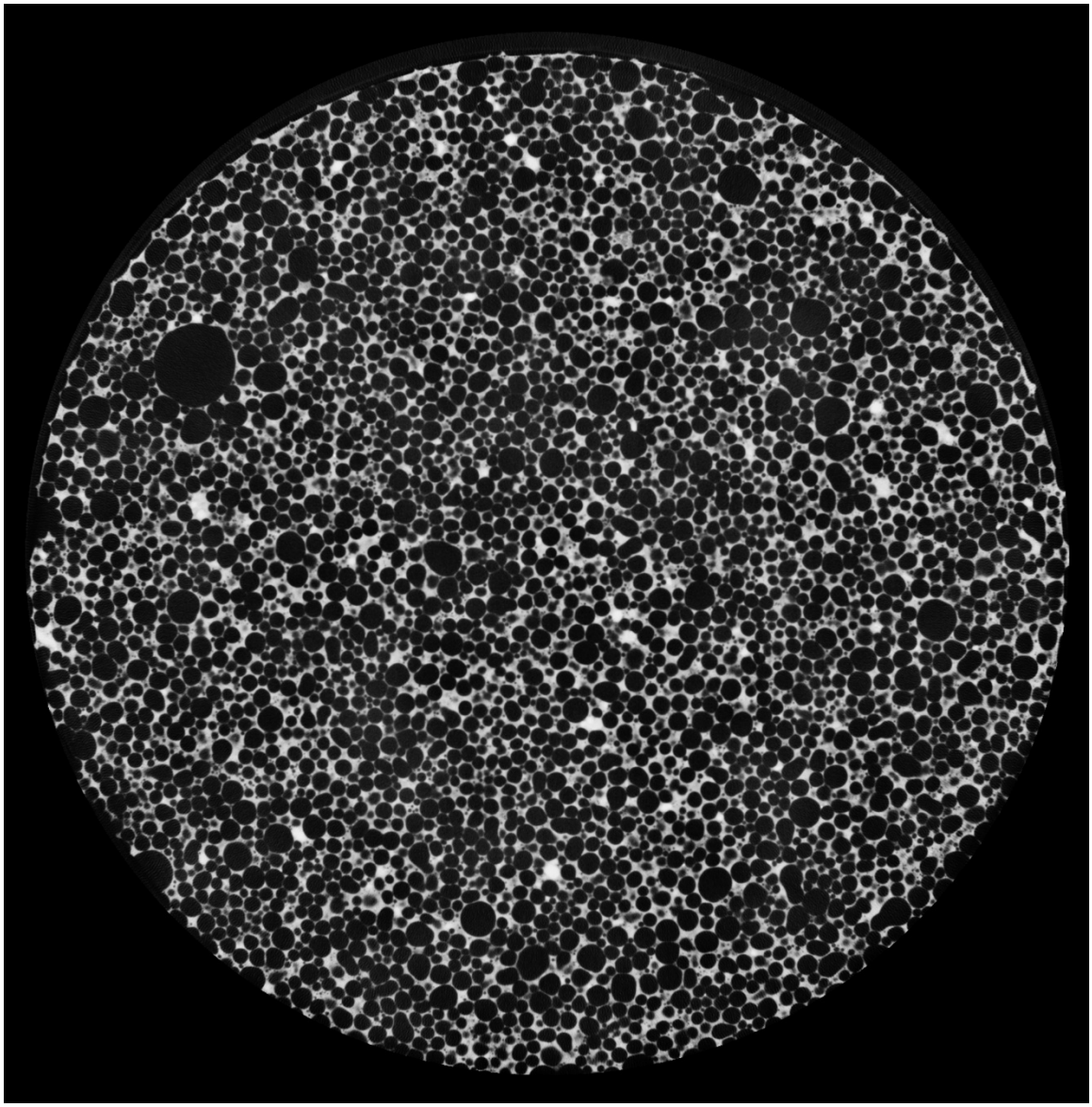

Figure 58. CT scan image of specimen B1-23 after the AD treatment, No. 0243.

The image cross-section is located 0.778” above the center of the specimen. The dark spherical objects are the foamed air voids, and the light matrix being the concrete skeleton structure. The degree of saturation is 1.61%. No free pore water is visible in the image.

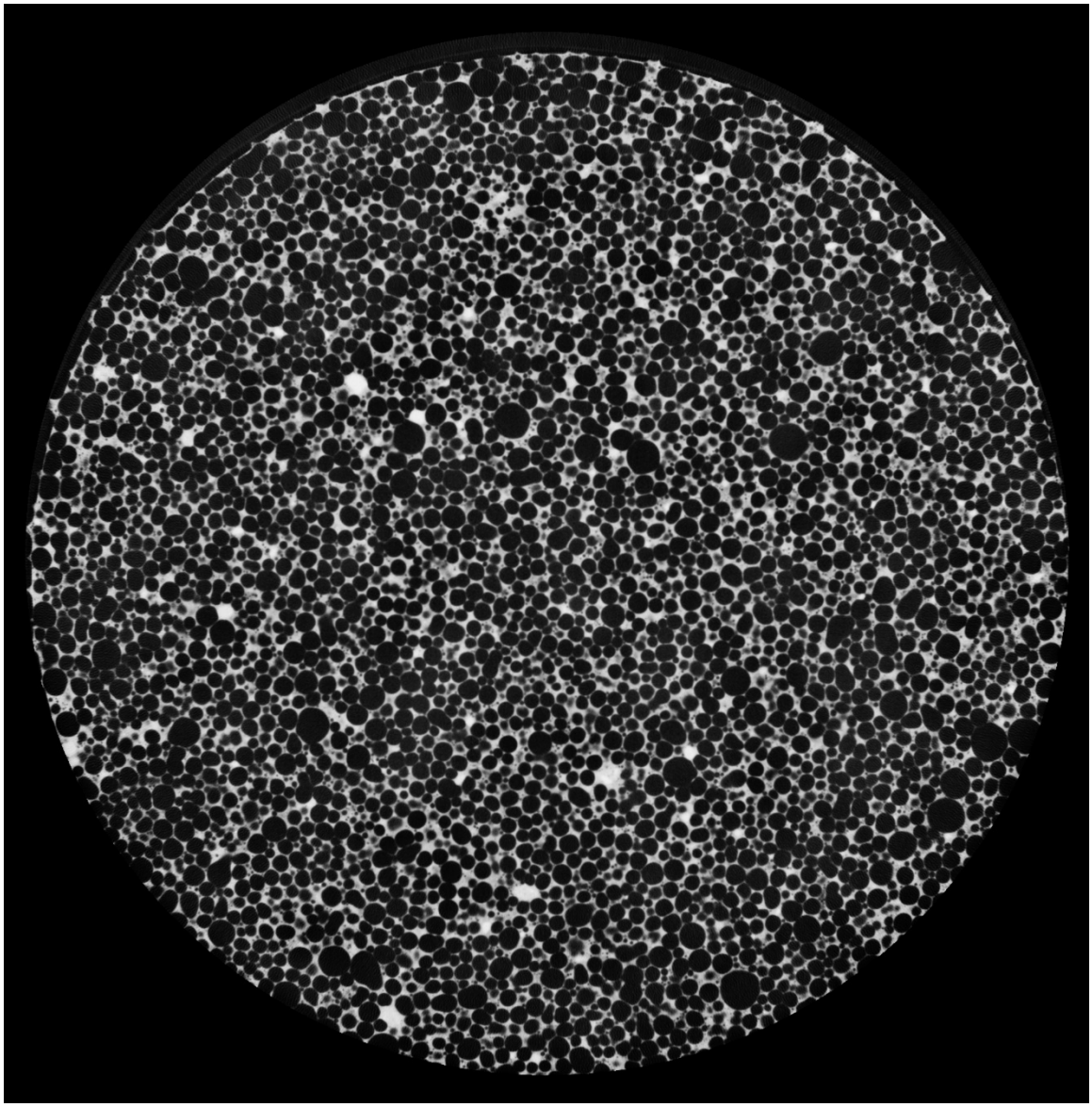

Figure 59. CT scan image of specimen B1-23 after the AD treatment, No. 0729.

The image cross-section is located 0.778” below the center of the specimen. The dark spherical objects are the foamed air voids, and the light matrix being the concrete skeleton structure. The degree of saturation is 1.61%. No free pore water is visible in the image.

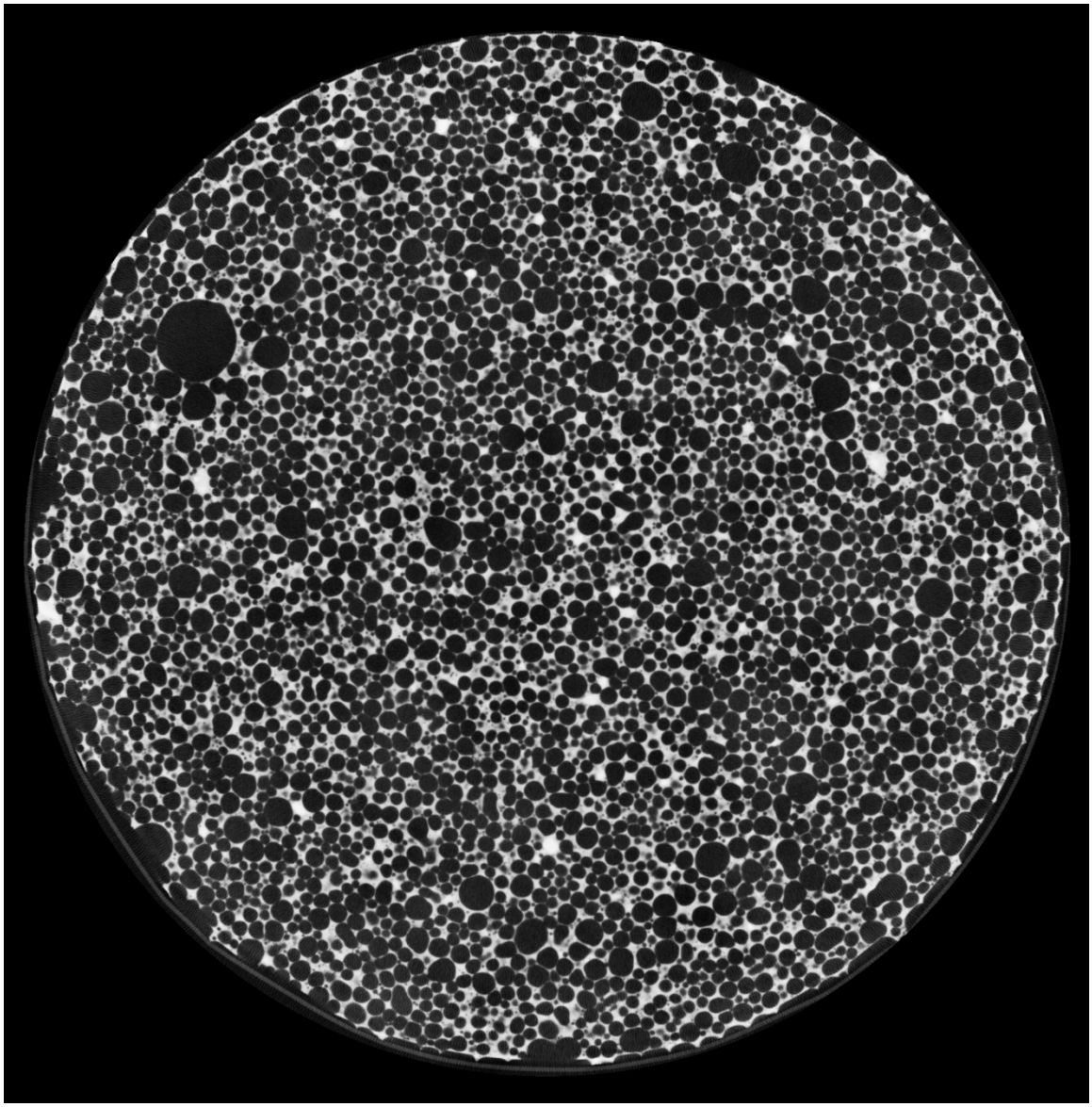

Figure 60. CT scan image of specimen B1-23 after the M5 treatment, No. 0243.

The image cross-section is located 0.778” above the center of the specimen. The dark spherical objects are the foamed air voids, and the light matrix being the concrete skeleton structure. The degree of saturation is 10.05%. No free pore water is visible in the image.

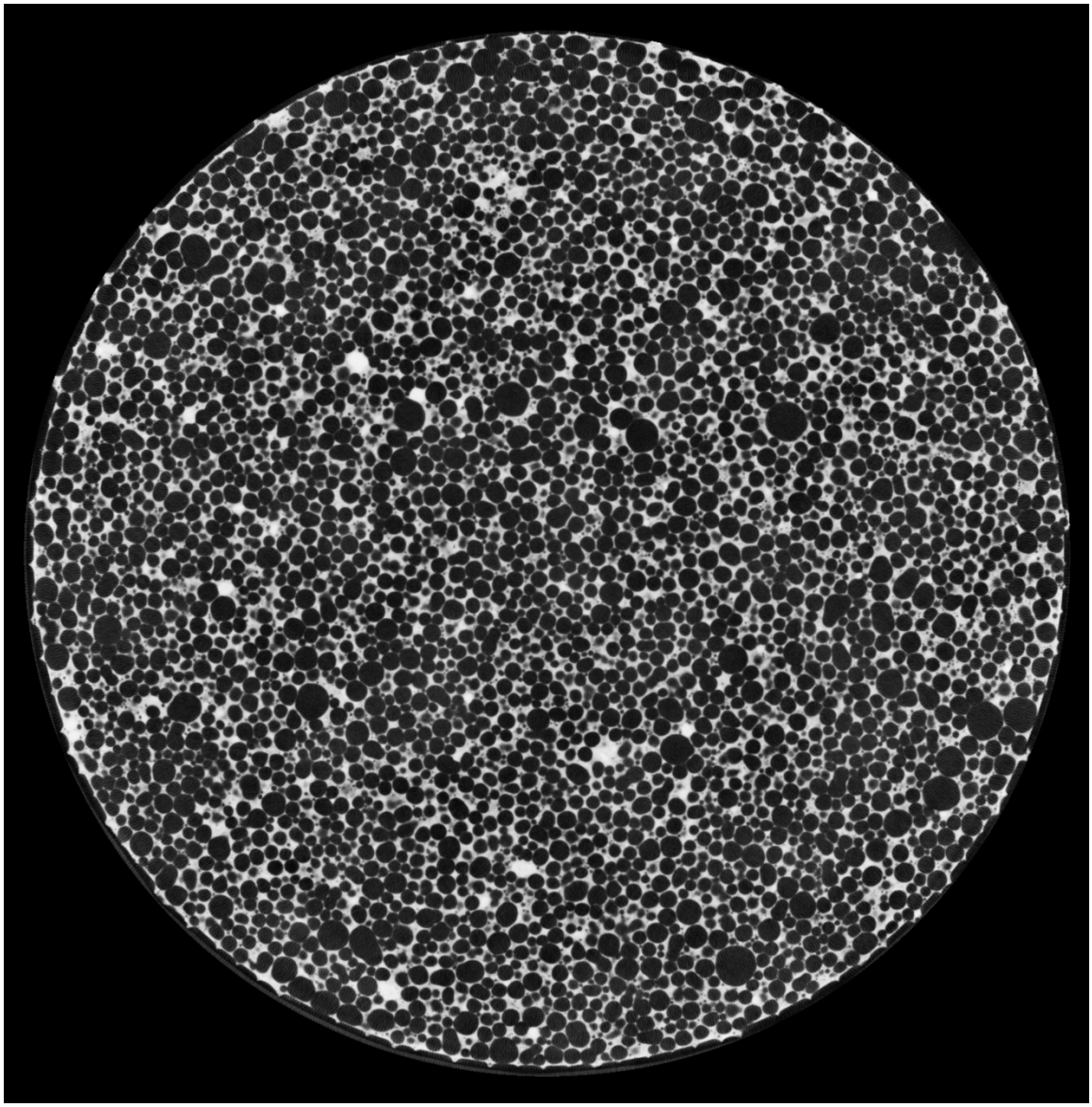

Figure 61. CT scan image of specimen B1-23 after the M5 treatment, No. 0729.

The image cross-section is located 0.778” below the center of the specimen. The dark spherical objects are the foamed air voids, and the light matrix being the concrete skeleton structure. The degree of saturation is 10.05%. No free pore water is visible in the image.

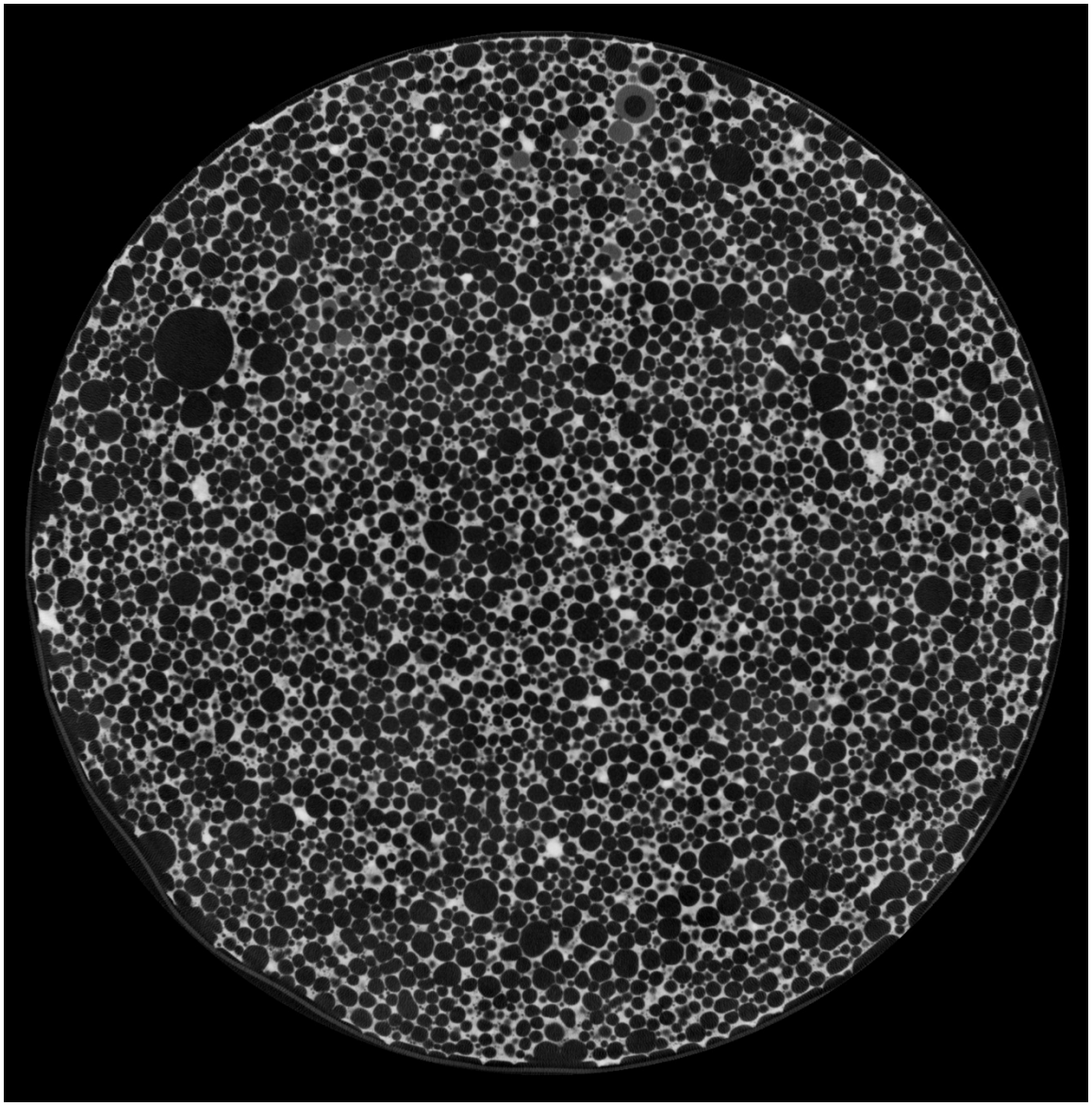

Figure 62. CT scan image of specimen B1-23 after the D1 treatment, No. 0243.

The image cross-section is located 0.778” above the center of the specimen. The dark spherical objects are the foamed air voids, and the light matrix being the concrete skeleton structure. The degree of saturation is 16.86%. Free pore water is visible in the image as grey spheres.

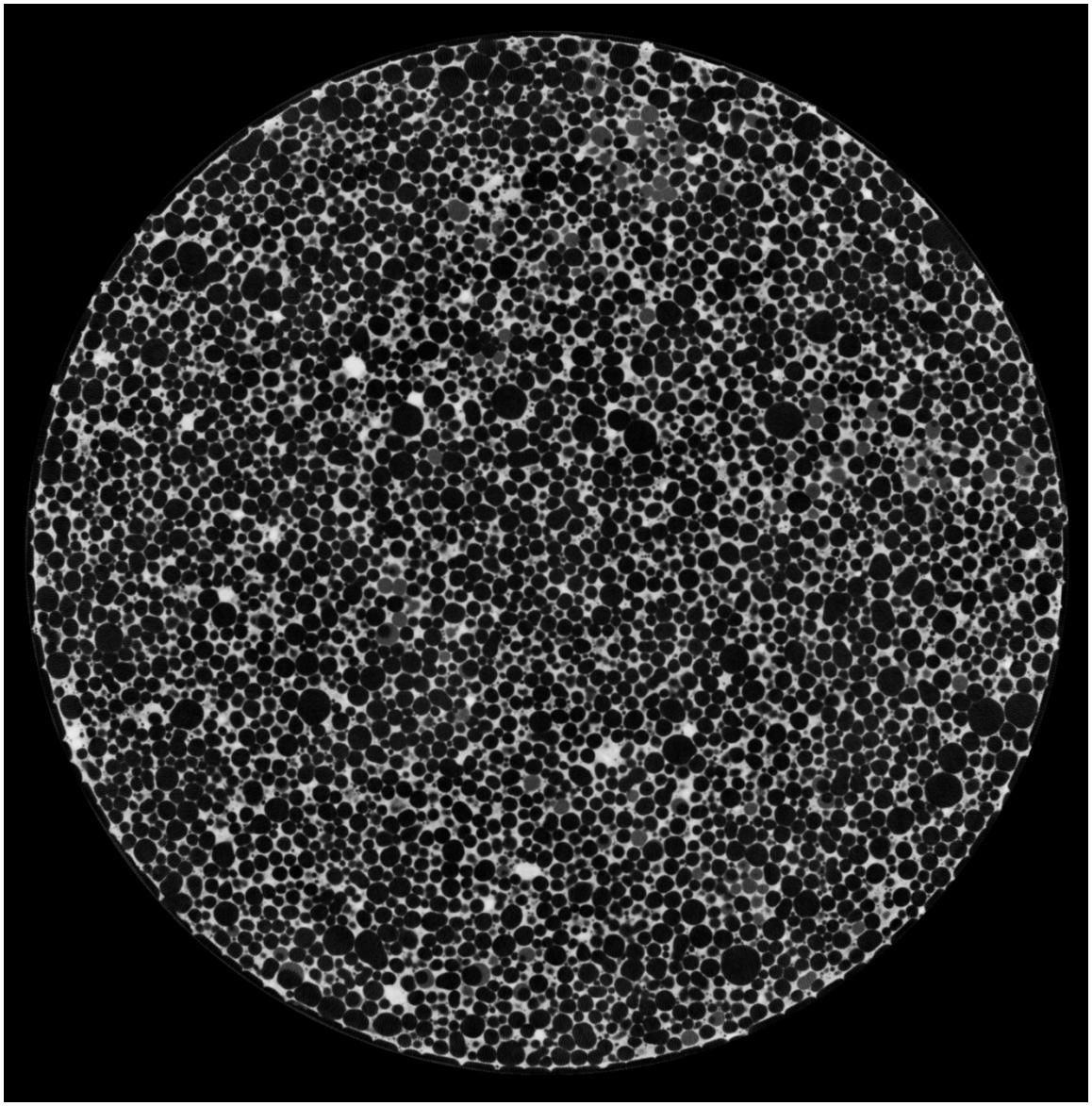

Figure 63. CT scan image of specimen B1-23 after the D1 treatment, No. 0729.

The image cross-section is located 0.778” below the center of the specimen. The dark spherical objects are the foamed air voids, and the light matrix being the concrete skeleton structure. The degree of saturation is 16.86%. Free pore water is visible in the image as grey spheres.

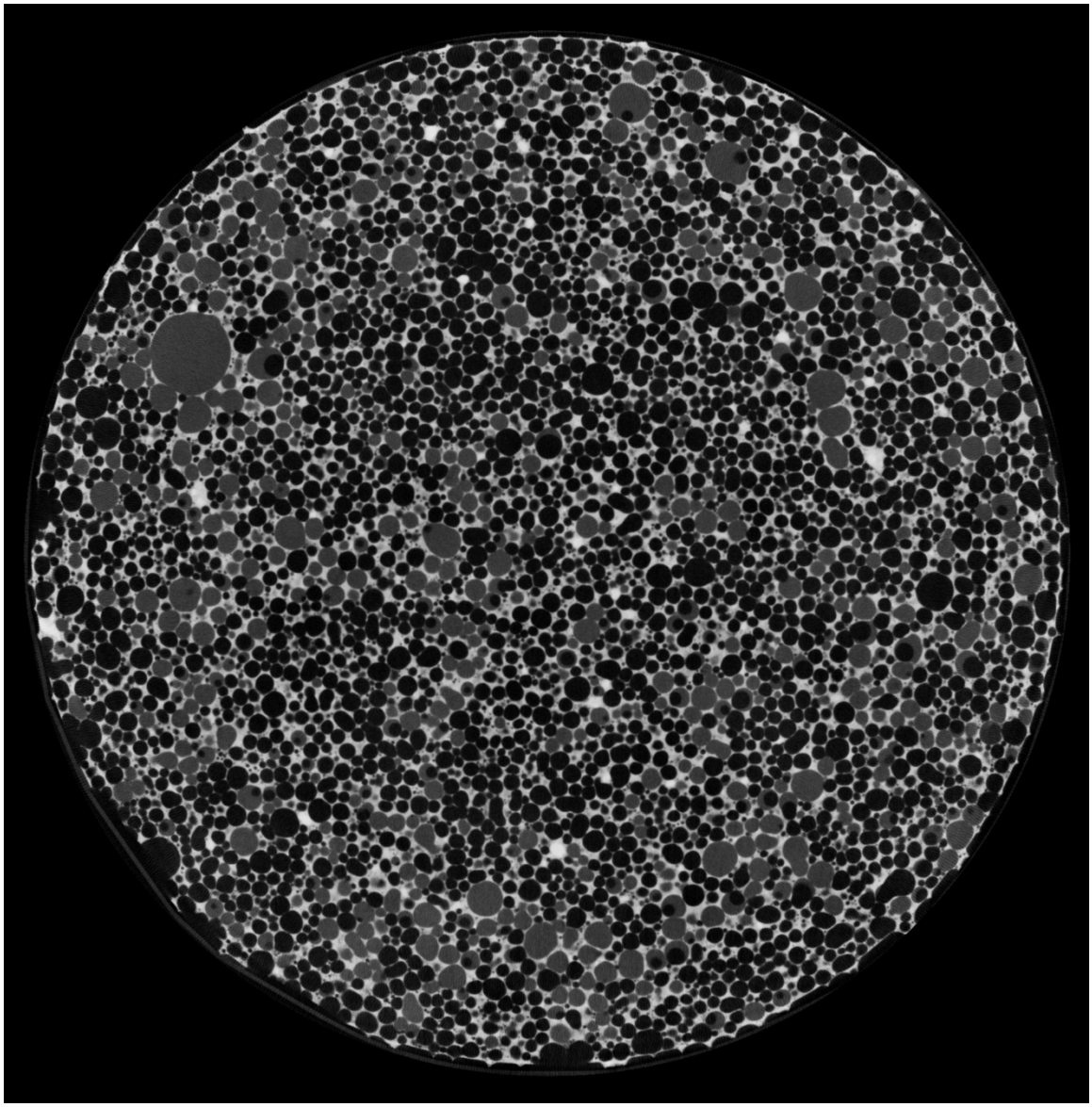

Figure 64. CT scan image of specimen B1-23 after the V8 treatment, No. 0243.

The image cross-section is located 0.778” above the center of the specimen. The dark spherical objects are the foamed air voids, and the light matrix being the concrete skeleton structure. The degree of saturation is 35.37%. Free pore water is visible in the image as grey spheres.

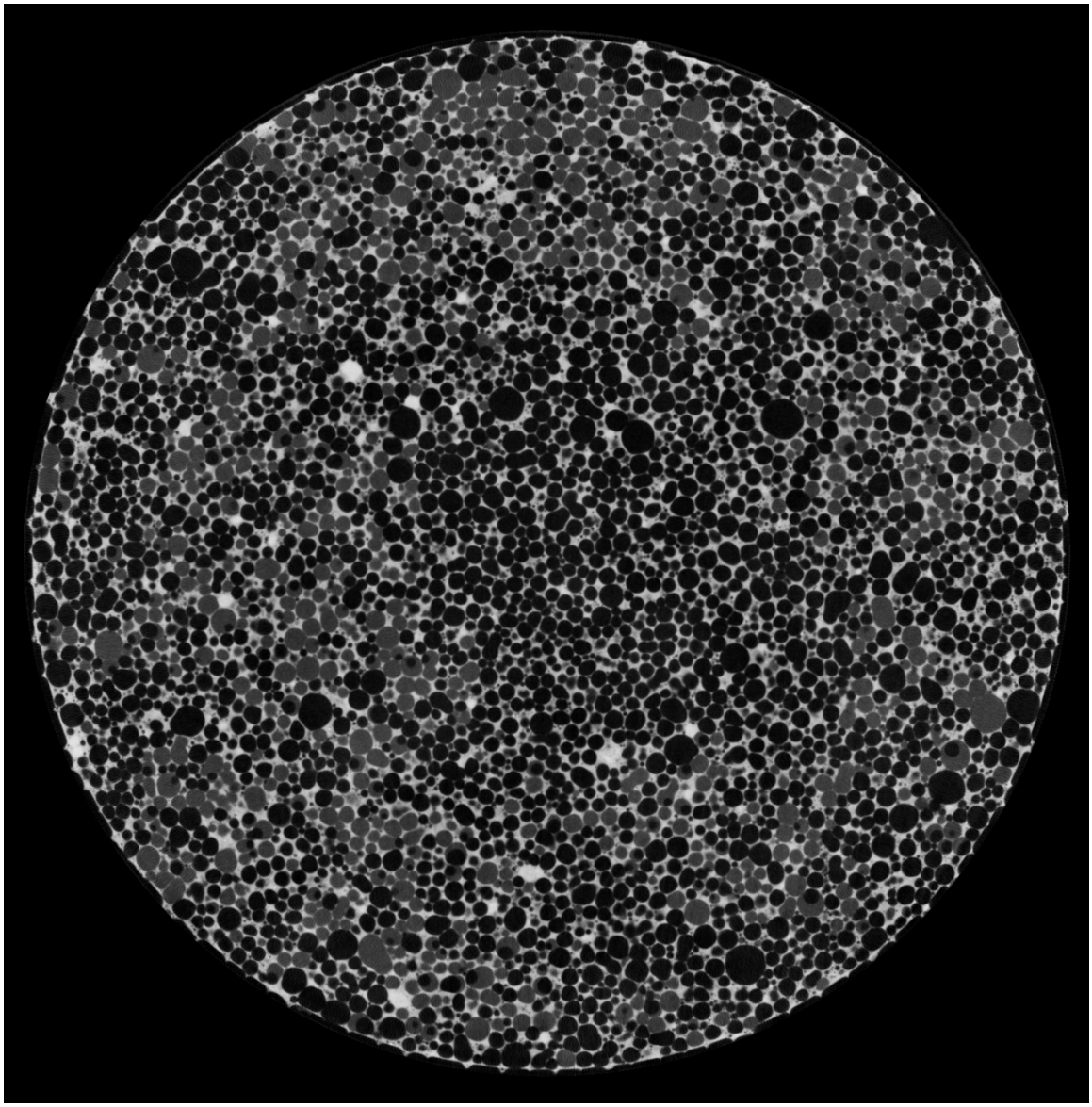

Figure 65. CT scan image of specimen B1-23 after the V8 treatment, No. 0729.

The image cross-section is located 0.778” below the center of the specimen. The dark spherical objects are the foamed air voids, and the light matrix being the concrete skeleton structure. The degree of saturation is 35.37%. Free pore water is visible in the image as grey spheres.

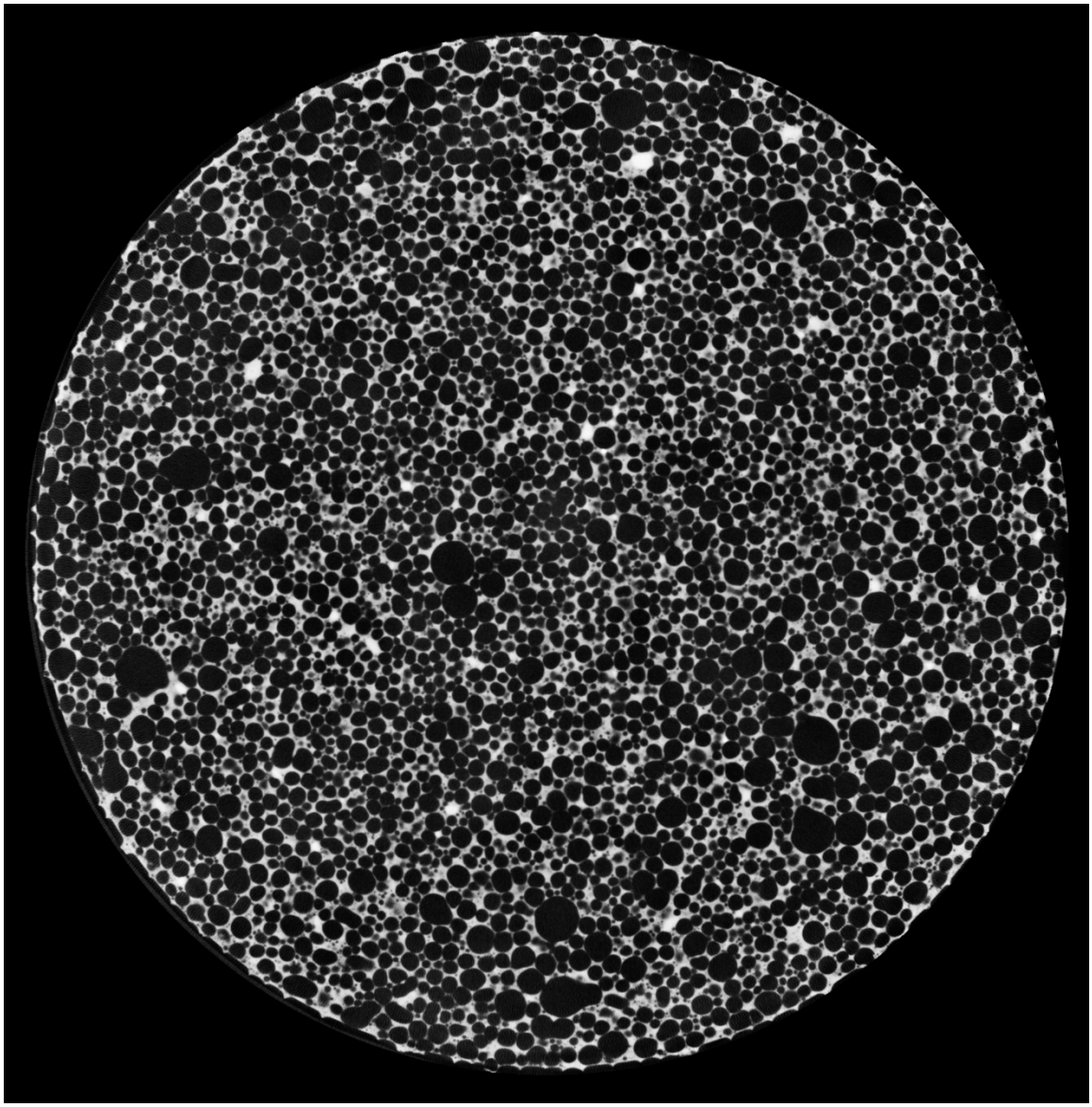

Figure 66. CT scan image of specimen B1-24 after the AD treatment, No. 0243.

The image cross-section is located 0.778” above the center of the specimen. The dark spherical objects are the foamed air voids, and the light matrix being the concrete skeleton structure. The degree of saturation is 1.77%. No free pore water is visible in the image.

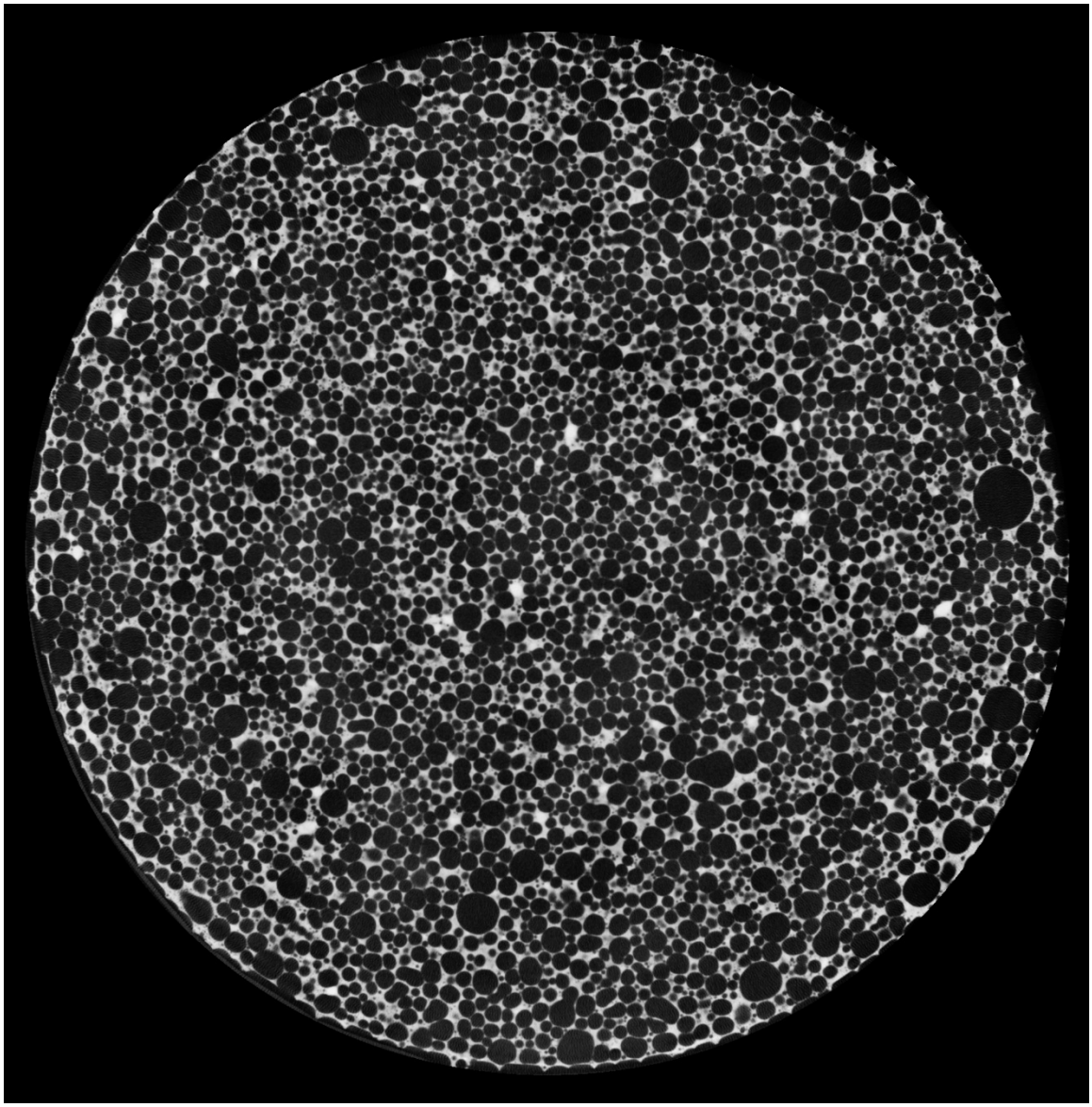

Figure 67. CT scan image of specimen B1-24 after the AD treatment, No. 0729.

The image cross-section is located 0.778” below the center of the specimen. The dark spherical objects are the foamed air voids, and the light matrix being the concrete skeleton structure. The degree of saturation is 1.77%. No free pore water is visible in the image.

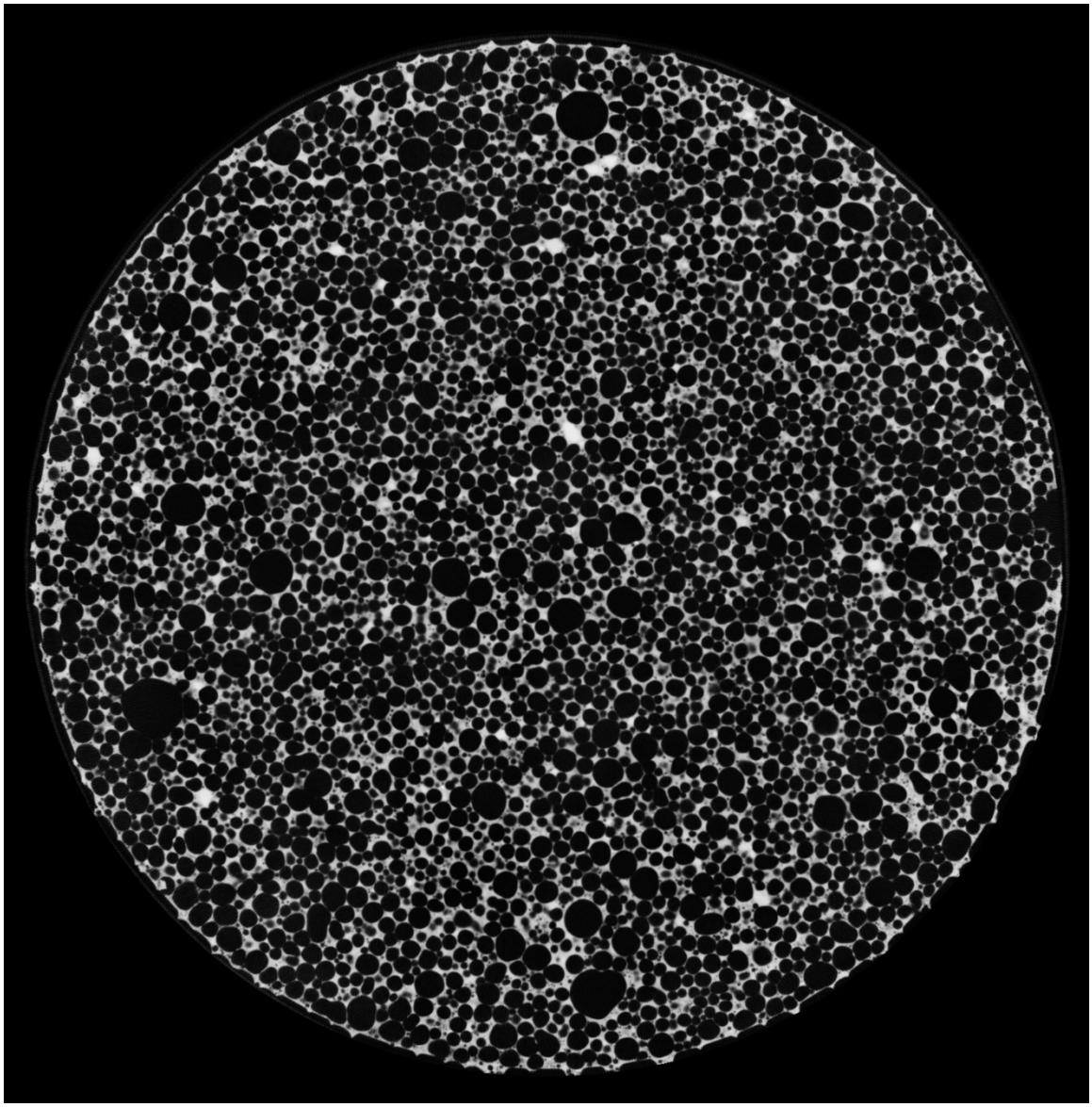

Figure 68. CT scan image of specimen B1-24 after the M5 treatment, No. 0243.

The image cross-section is located 0.778” above the center of the specimen. The dark spherical objects are the foamed air voids, and the light matrix being the concrete skeleton structure. The degree of saturation is 9.99%. No free pore water is visible in the image.

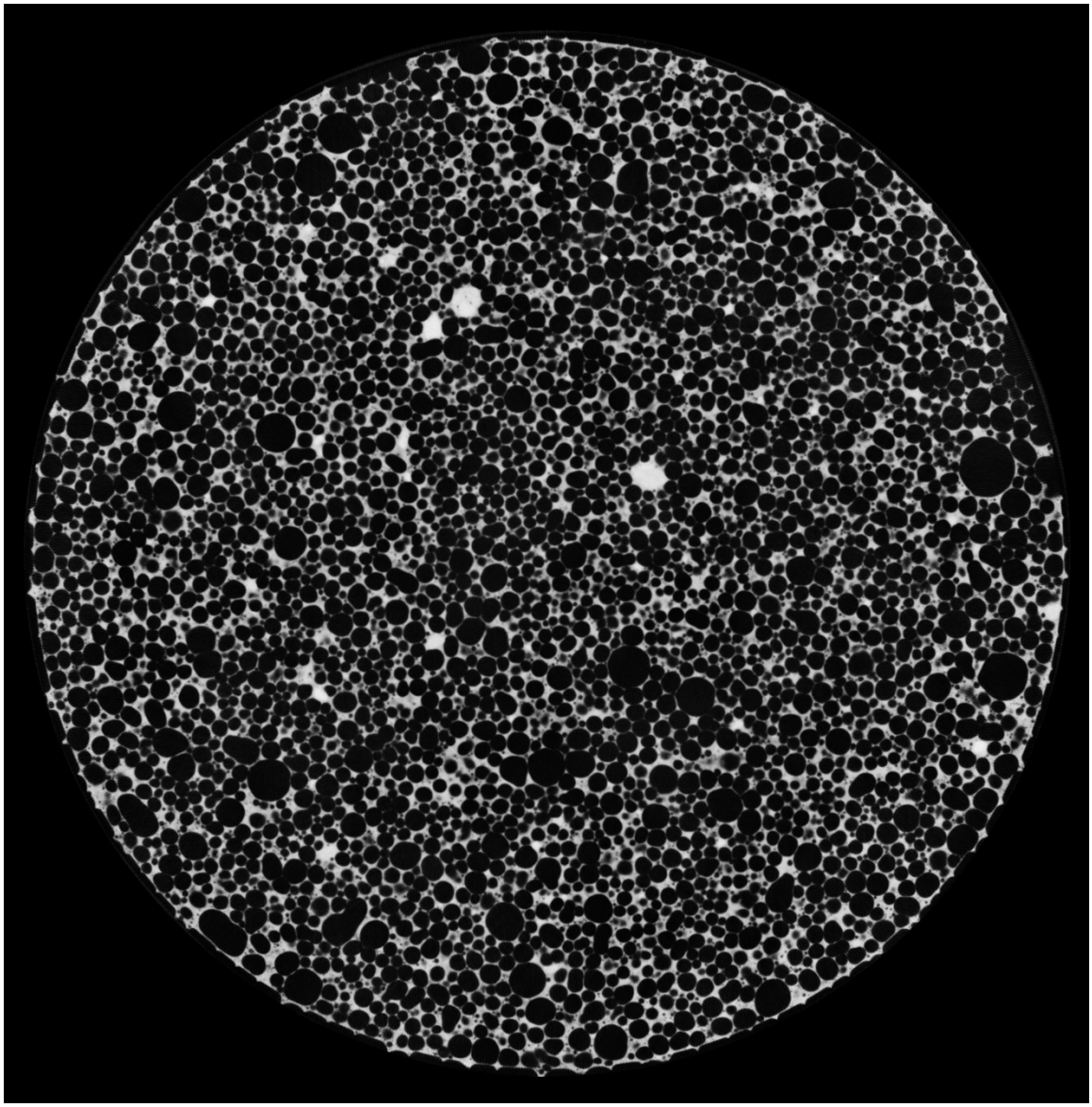

Figure 69. CT scan image of specimen B1-24 after the M5 treatment, No. 0729.

The image cross-section is located 0.778” below the center of the specimen. The dark spherical objects are the foamed air voids, and the light matrix being the concrete skeleton structure. The degree of saturation is 9.99%. No free pore water is visible in the image.

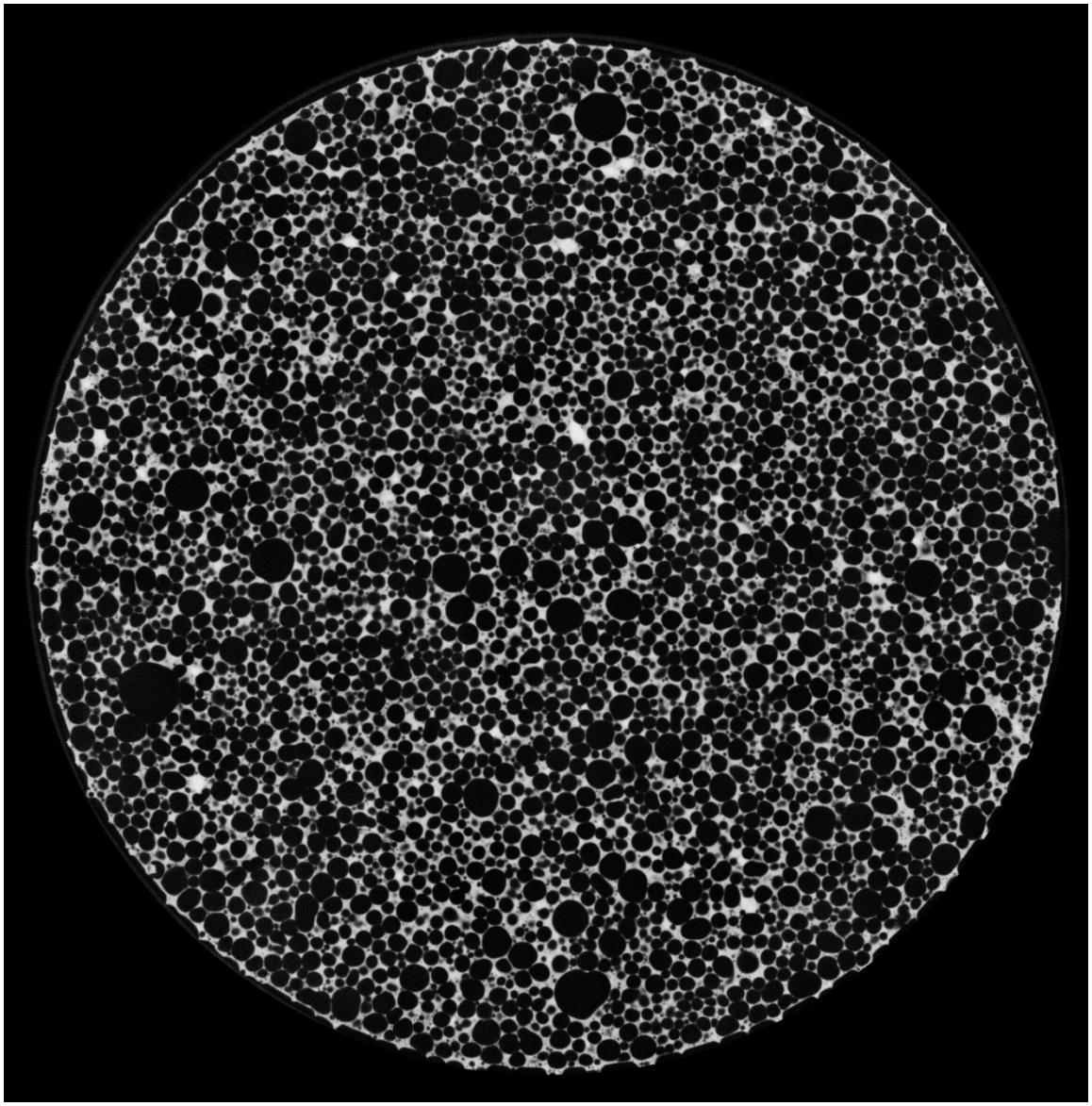

Figure 70. CT scan image of specimen B1-24 after the D1 treatment, No. 0243.

The image cross-section is located 0.778” above the center of the specimen. The dark spherical objects are the foamed air voids, and the light matrix being the concrete skeleton structure. The degree of saturation is 16.35%. No free pore water is visible in the image.

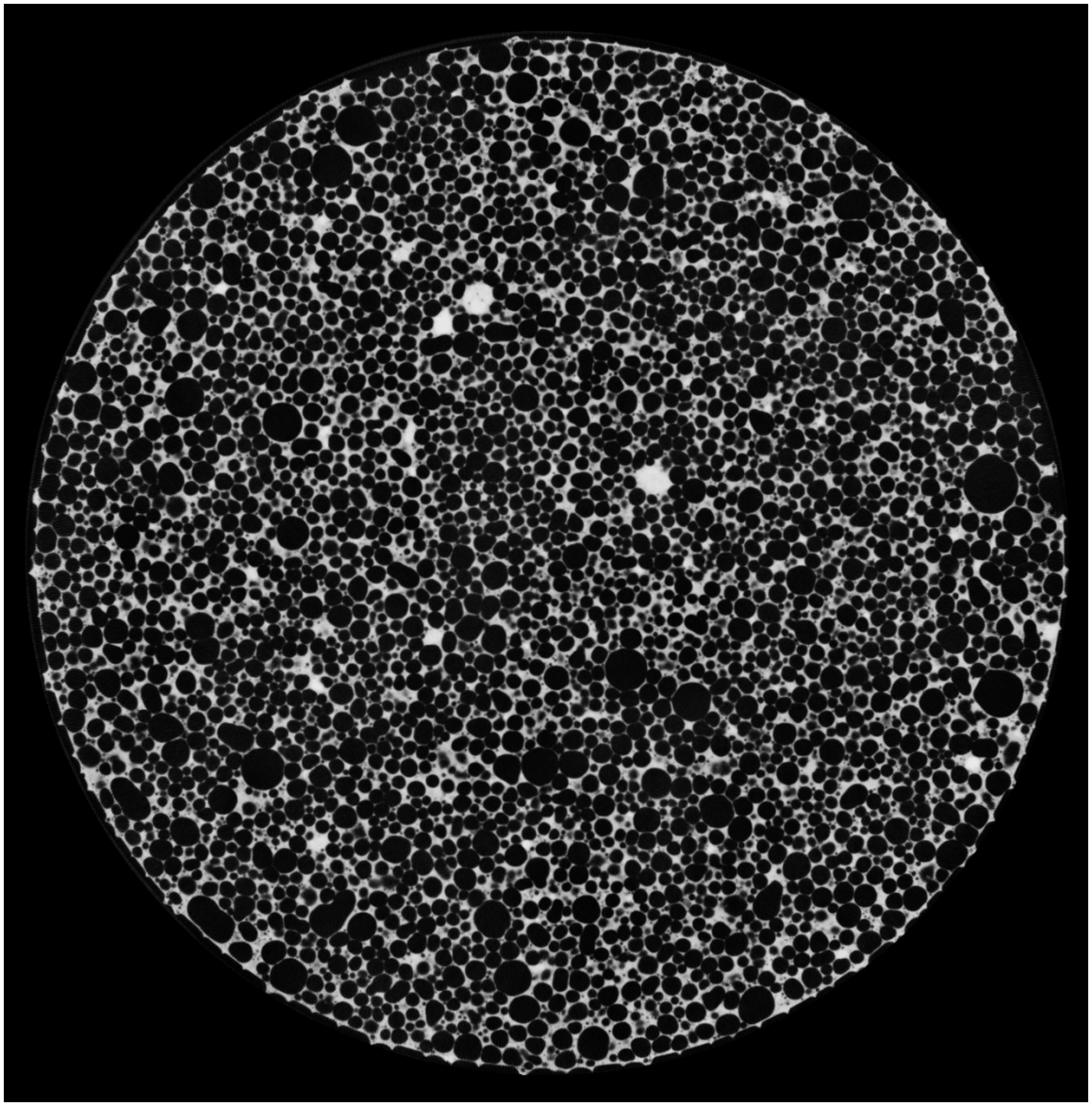

Figure 71. CT scan image of specimen B1-24 after the D1 treatment, No. 0729.

The image cross-section is located 0.778” below the center of the specimen. The dark spherical objects are the foamed air voids, and the light matrix being the concrete skeleton structure. The degree of saturation is 16.35%. No free pore water is visible in the image.

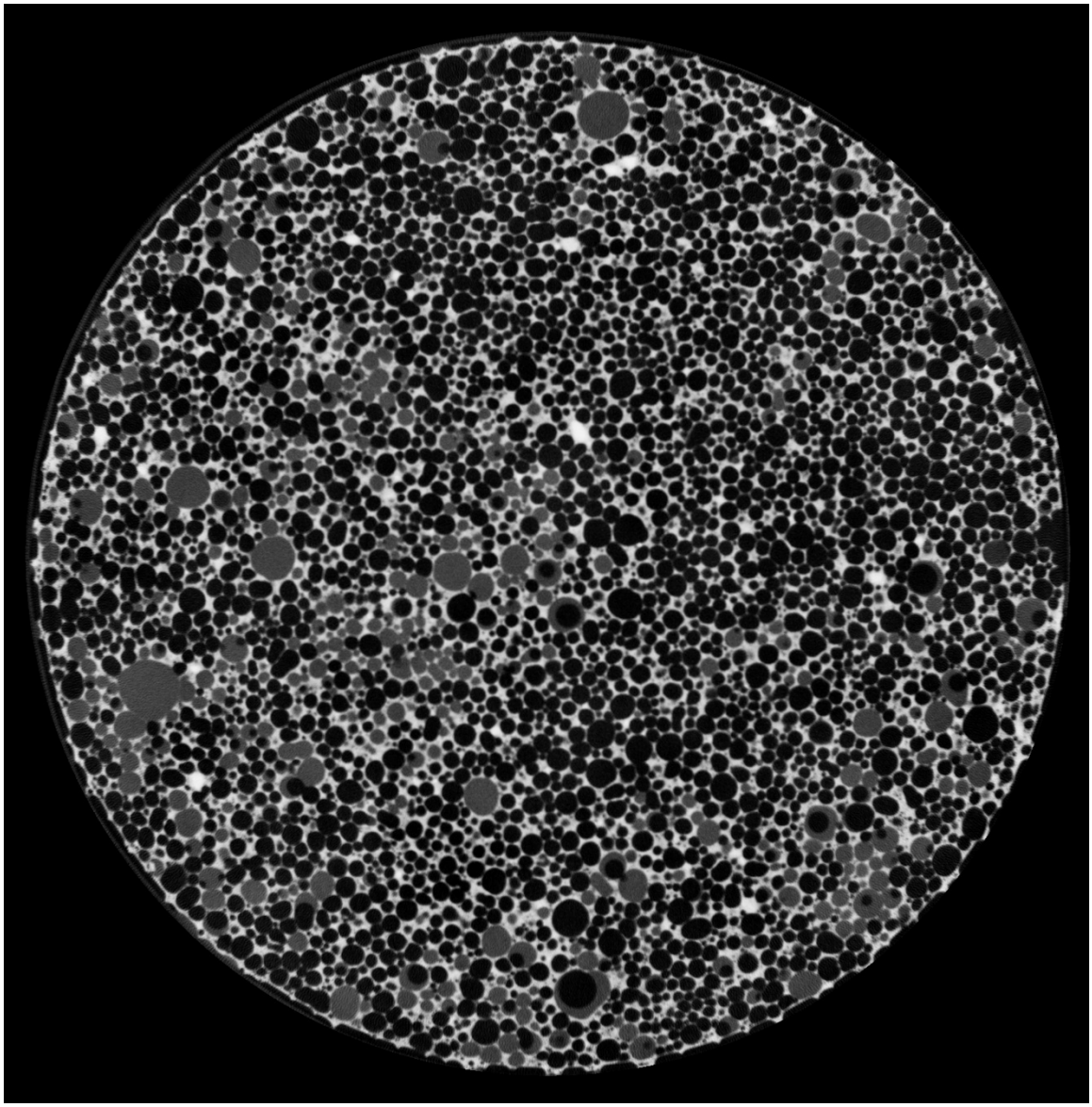

Figure 72. CT scan image of specimen B1-24 after the V8 treatment, No. 0243.

The image cross-section is located 0.778” above the center of the specimen. The dark spherical objects are the foamed air voids, and the light matrix being the concrete skeleton structure. The degree of saturation is 24.67%. Free pore water is visible in the image as grey spheres.

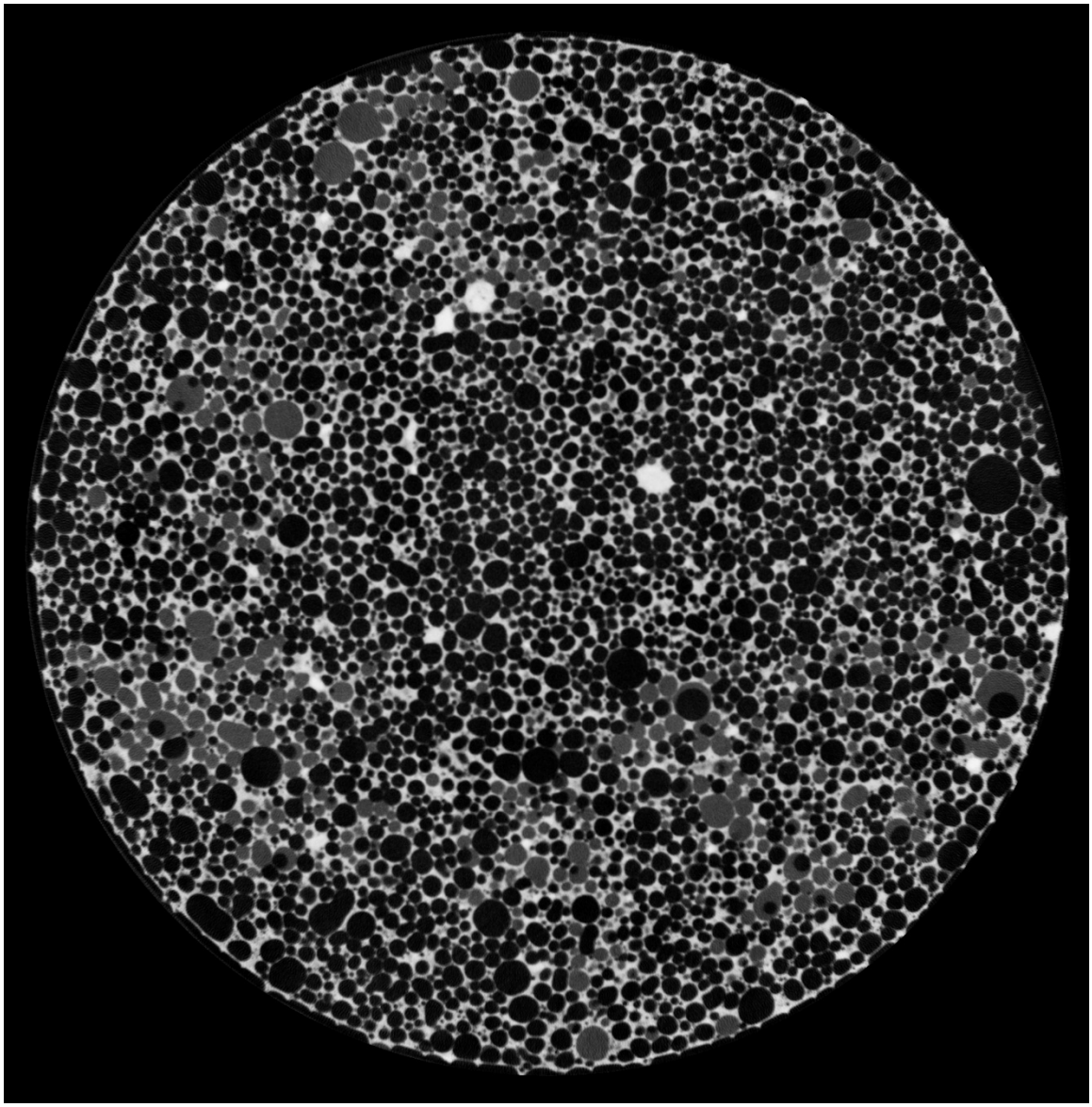

Figure 73. CT scan image of specimen B1-24 after the V8 treatment, No. 0729.

The image cross-section is located 0.778” below the center of the specimen. The dark spherical objects are the foamed air voids, and the light matrix being the concrete skeleton structure. The degree of saturation is 24.67%. Free pore water is visible in the image as grey spheres.

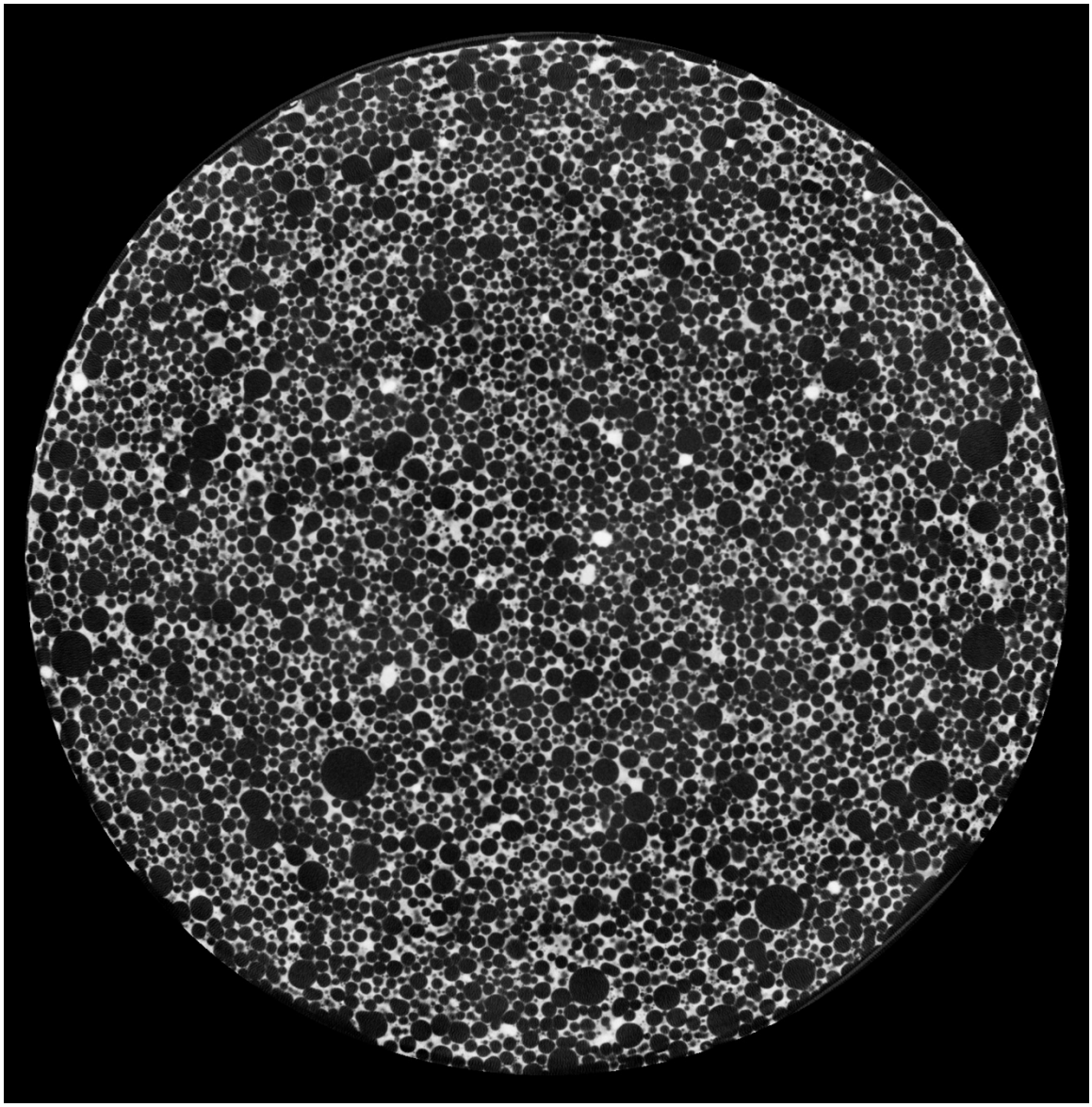

Figure 74. CT scan image of specimen B3-24 after the AD treatment, No. 0243.

The image cross-section is located 0.778” above the center of the specimen. The dark spherical objects are the foamed air voids, and the light matrix being the concrete skeleton structure. The degree of saturation is 1.67%. No free pore water is visible in the image.

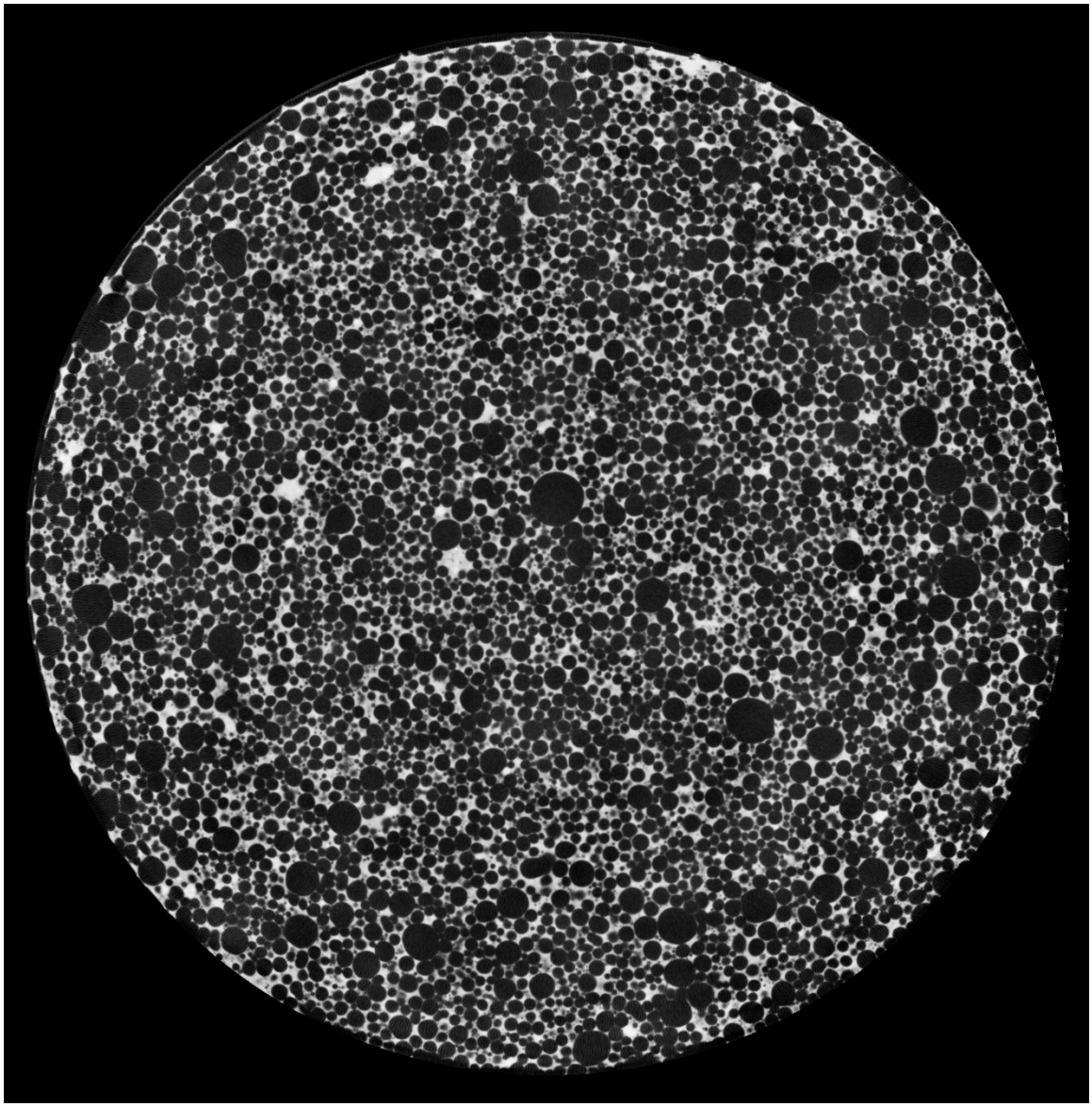

Figure 75. CT scan image of specimen B3-24 after the AD treatment, No. 0729.

The image cross-section is located 0.778” below the center of the specimen. The dark spherical objects are the foamed air voids, and the light matrix being the concrete skeleton structure. The degree of saturation is 1.67%. No free pore water is visible in the image.

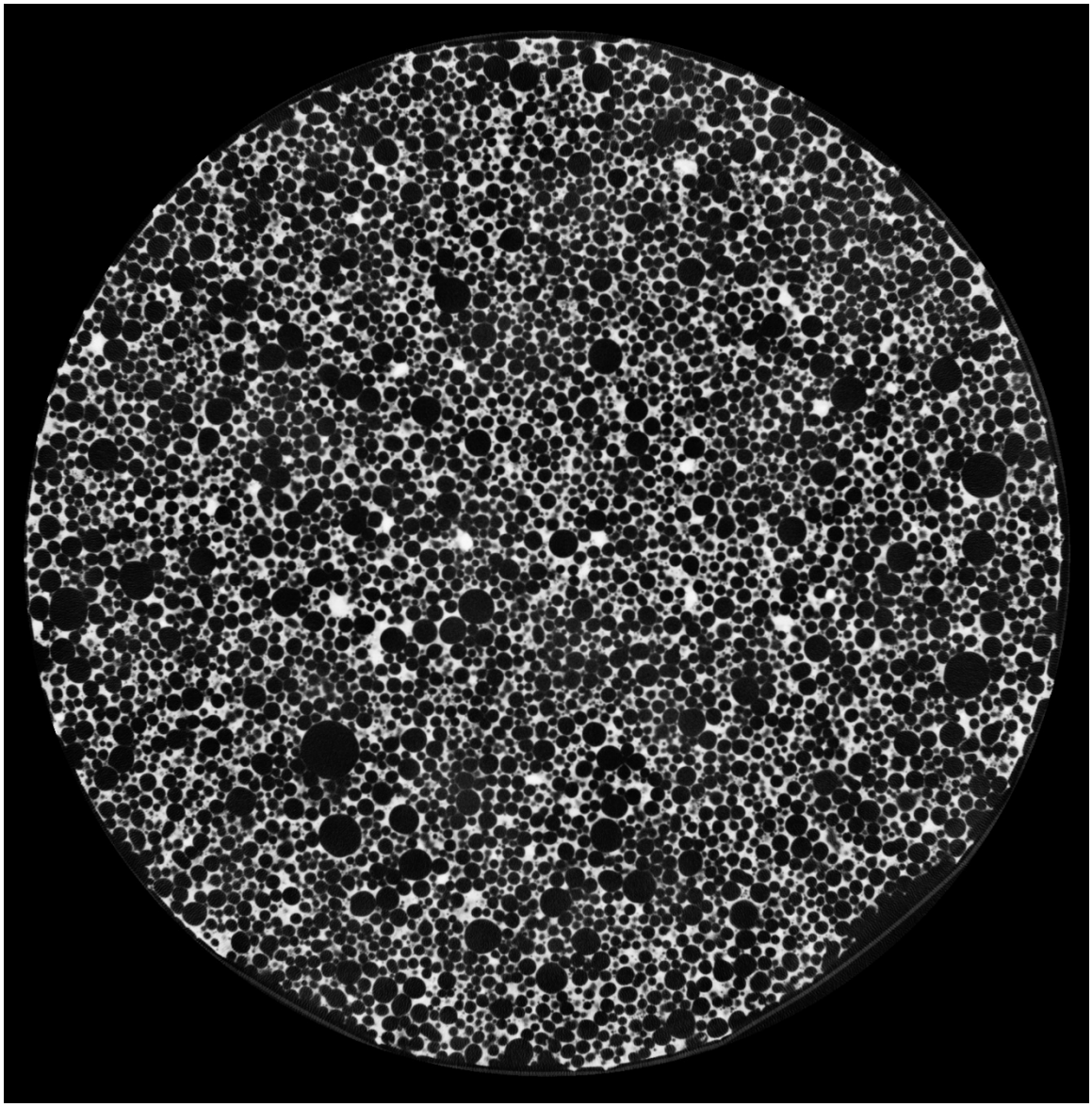

Figure 76. CT scan image of specimen B3-24 after the M5 treatment, No. 0243.

The image cross-section is located 0.778” above the center of the specimen. The dark spherical objects are the foamed air voids, and the light matrix being the concrete skeleton structure. The degree of saturation is 10.80%. No free pore water is visible in the image.

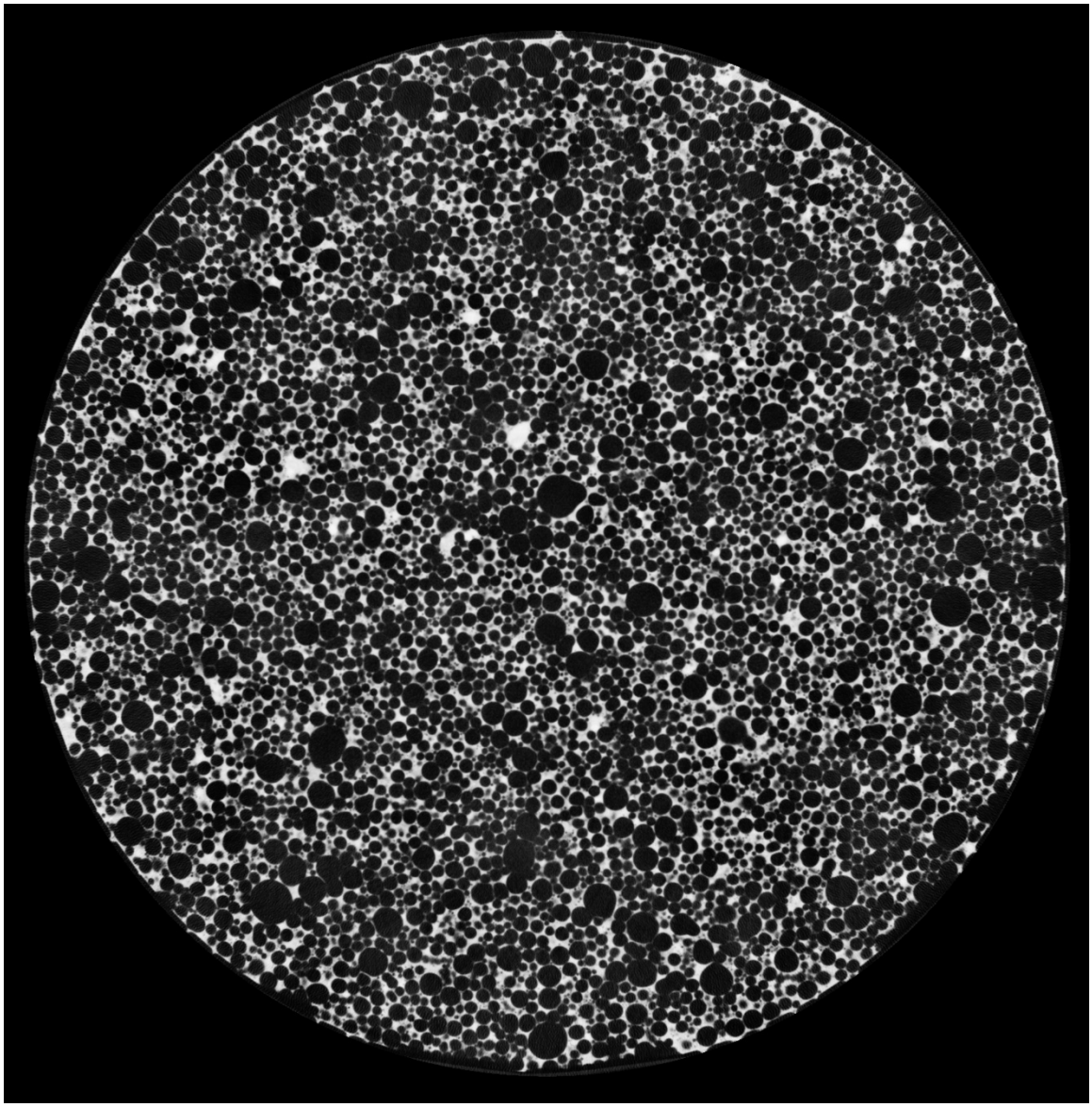

Figure 77. CT scan image of specimen B3-24 after the M5 treatment, No. 0729.

The image cross-section is located 0.778” below the center of the specimen. The dark spherical objects are the foamed air voids, and the light matrix being the concrete skeleton structure. The degree of saturation is 10.80%. No free pore water is visible in the image.

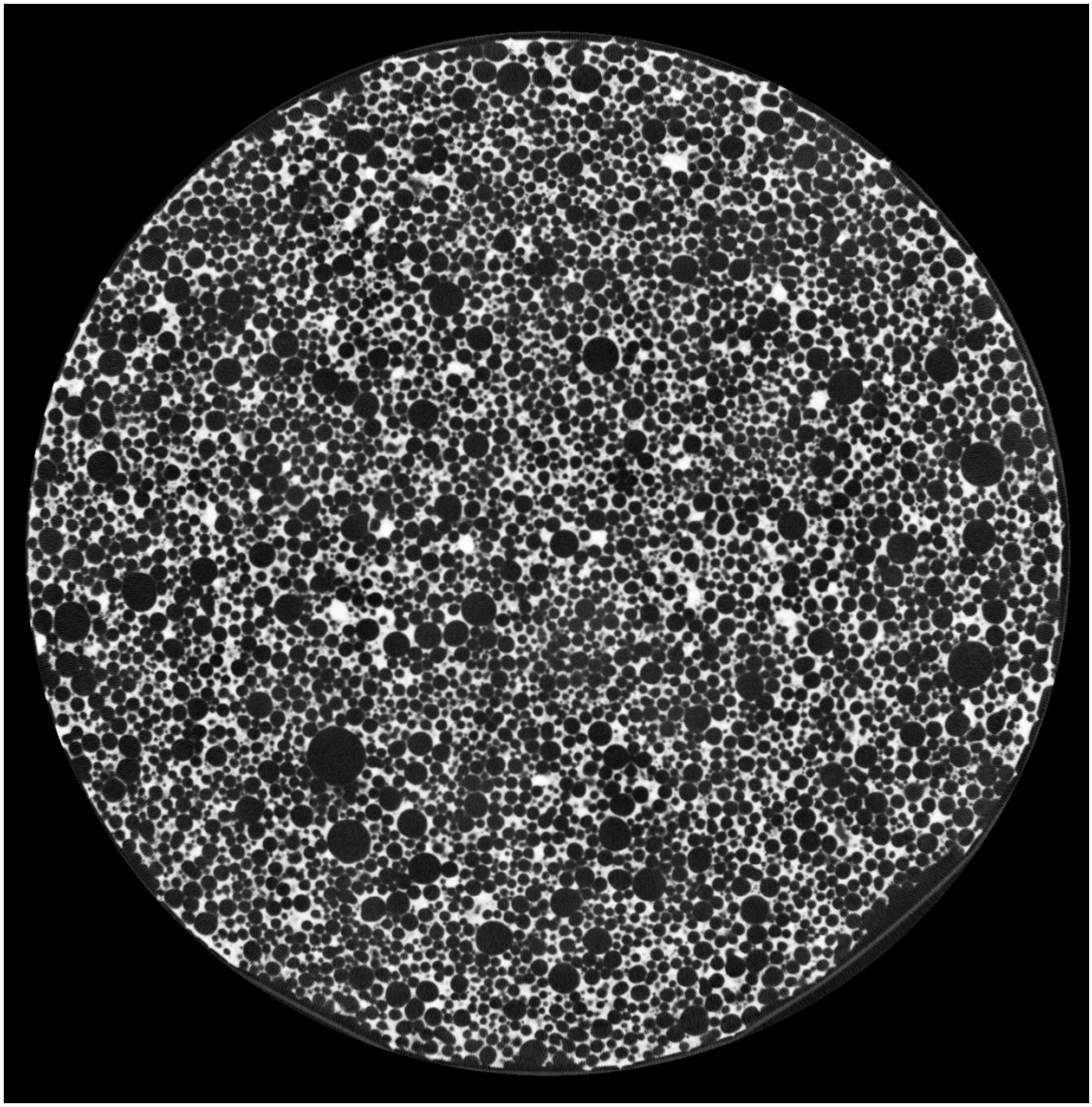

Figure 78. CT scan image of specimen B3-24 after the D1 treatment, No. 0243.

The image cross-section is located 0.778” above the center of the specimen. The dark spherical objects are the foamed air voids, and the light matrix being the concrete skeleton structure. The degree of saturation is 16.43%. Free pore water is visible in the image as grey spheres.

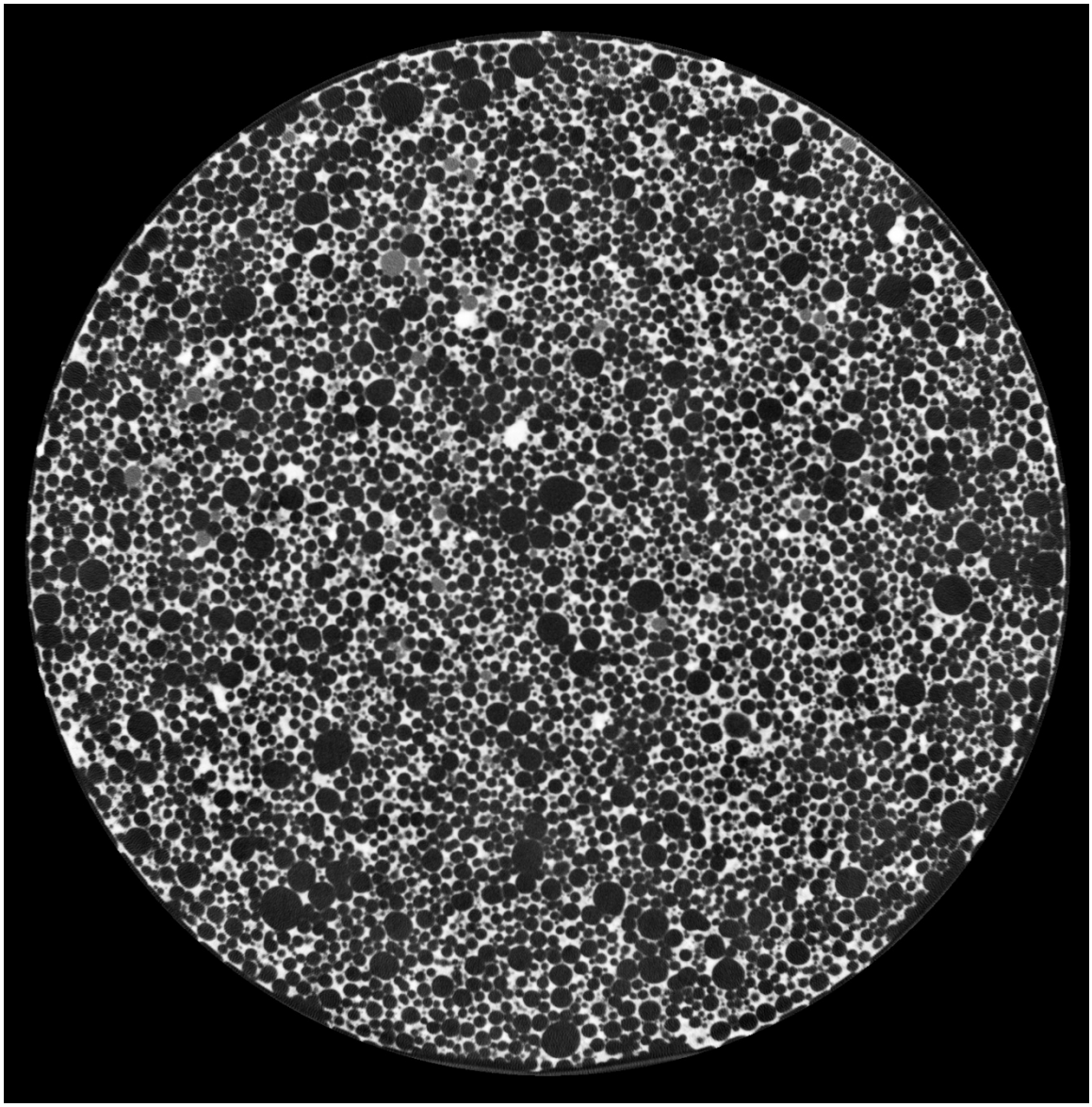

Figure 79. CT scan image of specimen B3-24 after the D1 treatment, No. 0729.

The image cross-section is located 0.778” below the center of the specimen. The dark spherical objects are the foamed air voids, and the light matrix being the concrete skeleton structure. The degree of saturation is 16.43%. Free pore water is visible in the image as grey spheres.

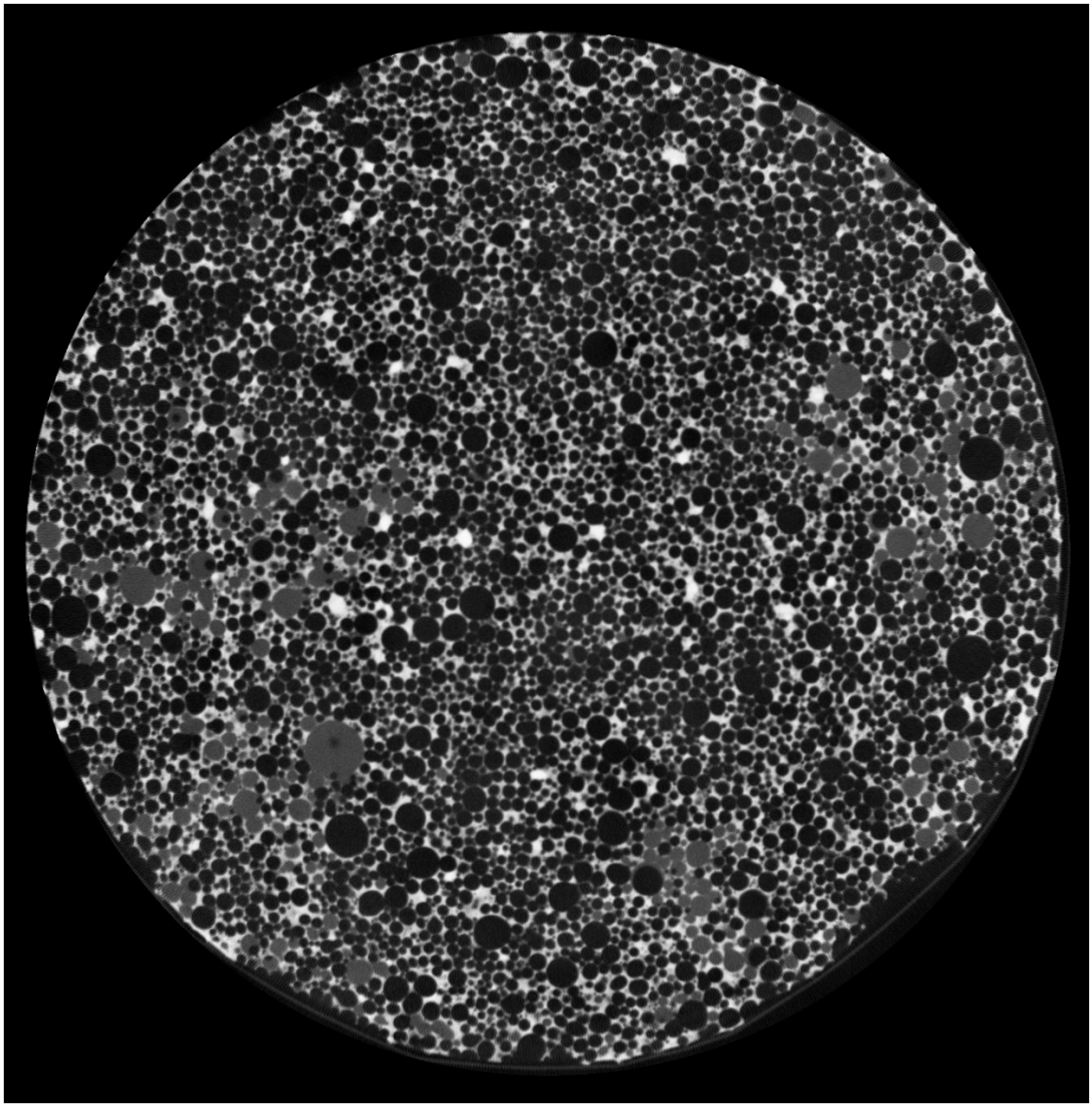

Figure 80. CT scan image of specimen B3-24 after the V8 treatment, No. 0243.

The image cross-section is located 0.778” above the center of the specimen. The dark spherical objects are the foamed air voids, and the light matrix being the concrete skeleton structure. The degree of saturation is 30.61%. Free pore water is visible in the image as grey spheres.

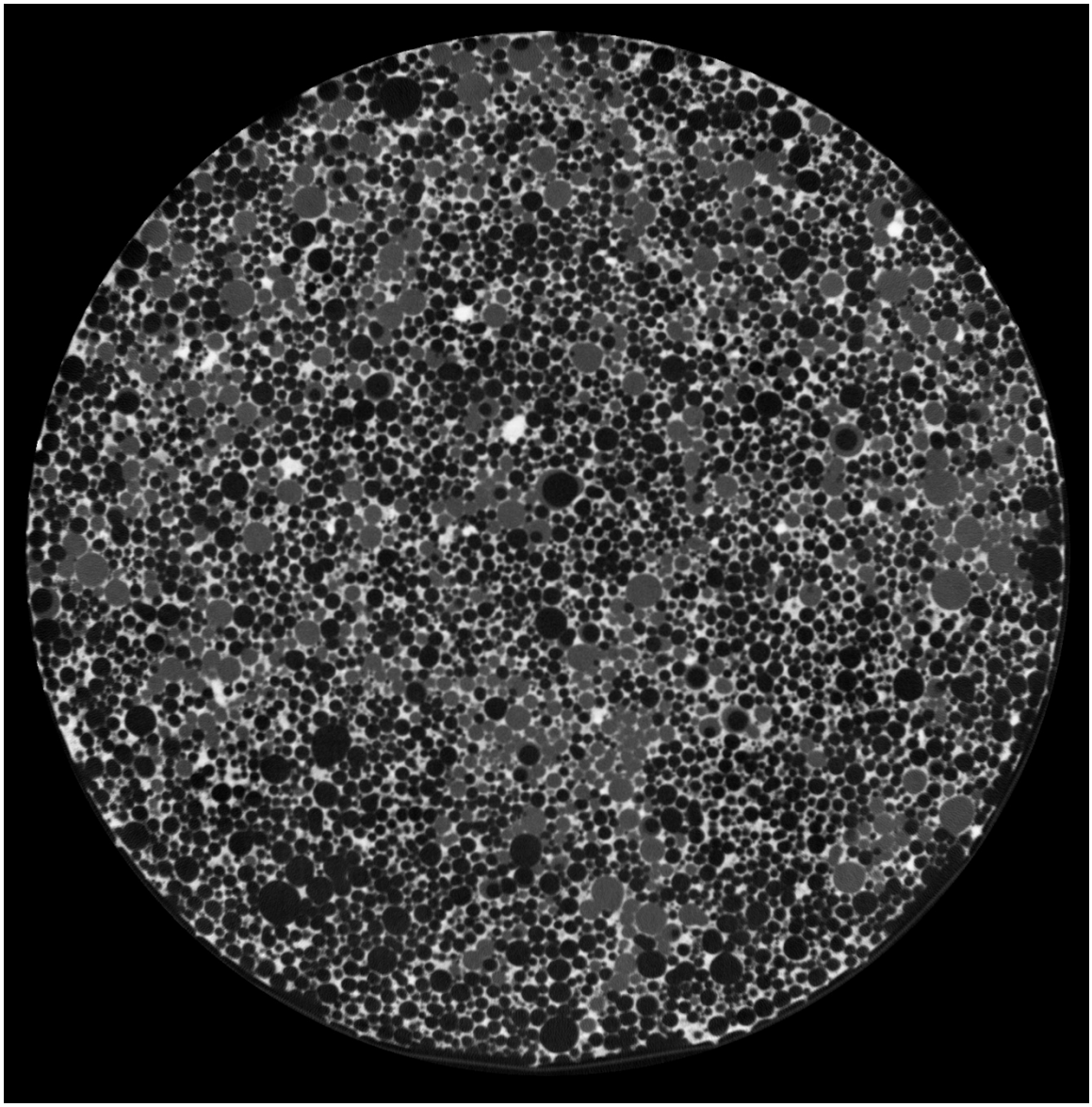

Figure 81. CT scan image of specimen B3-24 after the V8 treatment, No. 0729.

The image cross-section is located 0.778” below the center of the specimen. The dark spherical objects are the foamed air voids, and the light matrix being the concrete skeleton structure. The degree of saturation is 30.61%. Free pore water is visible in the image as grey spheres.

APPENDIX C

RESILIENT MODULUS TEST RESULTS

See Appendix_C_Resilient_Modulus_Test_Results.pdf

APPENDIX D

UNCONFINED COMPRESSIVE STRENGTH TEST RESULTS

See Appendix_D_Unconfined_Compressive_Strength_Results.pdf

APPENDIX E

TRIAXIAL COMPRESSION STRENGTH TEST RESULTS

See Appendix_E_Triaxial_Compression_Strength_Results.pdf

REFERENCES

AASHTO Technical Subcommittee: 1a, Soil and Unbound Recycled Materials. 2017. *T 307-99 Standard Method of Test for Determining the Resilient Modulus of Soils and Aggregate Materials*. Washington D.C.: AASHTO.

ACI Committee 523. 2006. *Guide for Cast-in-Place Low Density Cellular Concrete*. Cellular Concrete. American Concrete Institute.

Aerix Industries. n.d. "Clarification on Classes of LDCC." Aerix Industries.

Allen, D. L., and B. W. Meade. 1984. *An Evaluation of Elastizell Concrete as a Lightweight Fill Material*. Research Report. Kentucky Transportation Research Program, College of Engineering, University of Kentucky.

Amran, Y. H. M., N. Farzadnia, and A. A. Abang Ali. 2015. "Properties and applications of foamed concrete; a review." *Construction and Building Materials*, 101: 990–1005. https://doi.org/10.1016/j.conbuildmat.2015.10.112.

ASTM C09 Committee. 2011a. *C513/C513M-11 Test Method for Obtaining and Testing Specimens of Hardened Lightweight Insulating Concrete for Compressive Strength*. ASTM International.

ASTM C09 Committee. 2011b. *C869/C869M-11 Specification for Foaming Agents Used in Making Preformed Foam for Cellular Concrete*. ASTM International.

ASTM C09 Committee. 2012. *C495/C495M-12 Test Method for Compressive Strength of Lightweight Insulating Concrete*. ASTM International.

ASTM C09 Committee. 2015. *C666/C666M-15 Test Method for Resistance of Concrete to Rapid Freezing and Thawing*. ASTM International.

ASTM C09 Committee. 2019a. *C796/796M-19 Test Method for Foaming Agents for Use in Producing Cellular Concrete Using Preformed Foam*. ASTM International.

ASTM C09 Committee. 2019b. *C215-19 Test Method for Fundamental Transverse, Longitudinal, and Torsional Resonant Frequencies of Concrete Specimens*. ASTM International.

ASTM C09 Committee. 2019c. *C1138M-19 Test Method for Abrasion Resistance of Concrete (Underwater Method)*. ASTM International.

ASTM C16 Committee. 2019a. *C177-19 Test Method for Steady-State Heat Flux Measurements and Thermal Transmission Properties by Means of the Guarded-Hot-Plate Apparatus*. ASTM International.

ASTM C16 Committee. 2019b. *C1363-19 Test Method for Thermal Performance of Building Materials and Envelope Assemblies by Means of a Hot Box Apparatus*. ASTM International.

ASTM C16 Committee. 2021. *C518-21 Test Method for Steady-State Thermal Transmission Properties by Means of the Heat Flow Meter Apparatus*. ASTM International.

ASTM D18 Committee. 2014. *D854-14 Standard Test Methods for Specific Gravity of Solids by Water Pycnometer*. ASTM International.

ASTM D18 Committee. 2016a. *D5084-16a Test Methods for Measurement of Hydraulic Conductivity of Saturated Porous Materials Using a Flexible Wall Permeameter*. ASTM International.

ASTM D18 Committee. 2016b. *D2166/2166M-16 Standard Test Method for Unconfined Compressive Strength of Cohesive Soil*. ASTM International.

ASTM D18 Committee. 2019a. *D2434-19 Test Method for Permeability of Granular Soils (Constant Head)*. ASTM International.

ASTM D18 Committee. 2019b. *D2216-19 Standard Test Methods for Laboratory Determination of Water (Moisture) Content of Soil and Rock by Mass*. ASTM International.

ASTM D18 Committee. 2020. *D7181-20 Test Method for Consolidated Drained Triaxial Compression Test for Soils*. ASTM International.

ASTM E05 Committee. 2020. *E119-20 Test Methods for Fire Tests of Building Construction and Materials*. ASTM International.

Averyanov, S. 2018. “Analysis of construction experience of using lightweight cellular concrete as a subbase material.” Waterloo, Ontario, Canada: University Of Waterloo.

Bartlett, S. F. 2015. “Application of Caltrans mechanically stabliized earth wall design requirements to lightweight cellular concrete backfill.”

Bartlett, S. F., and E. C. Lawton. 2008. “Evaluating the Seismic Stability and Performance of Freestanding Geofoam Embankment.” *6th National Seismic Conference on Bridges and Highways*. Charleston, SC.

Bartlett, S. F., A. C. Trandafir, E. C. Lawton, and B. N. Lingwall. 2011. “Applications of EPS Geofoam in Design and Construction of Earthquake Resilient Infrastructure.” *EPS 2011*. Oslo Norway.

Cabrera, J. G., and C. J. Lynsdale. 1988. “A new gas permeameter for measuring the permeability of mortar and concrete.” *Magazine of Concrete Research*, 40 (11): 177–182.

Chica, L., and A. Alzate. 2019. “Cellular concrete review: new trends for application in construction.” *Construction and Building Materials*, 200: 637–647. https://doi.org/10.1016/j.conbuildmat.2018.12.136.

Davich, P., J. Labuz, B. Guzina, and A. Drescher. 2004. *Small Strain and Resilient Modulus Testing of Granular Soils*. 117. St. Paul, Minnesota: Minnesota Department of Transportation.

Decký, M., M. Drusa, K. Zgútová, M. Blaško, M. Hájek, and W. Scherfel. 2016. “Foam Concrete as New Material in Road Constructions.” *Procedia Engineering*, 161: 428–433. https://doi.org/10.1016/j.proeng.2016.08.585.

Draper, N. R., and H. Smith. 1998. *Applied Regression Analysis*. Wiley Series in Probability and Statistics. New York: John Wiley & Sons, Inc.

Elliott, R. P., and S. I. Thornton. 1988. “Resilient Modulus and AASHTO Pavement Design.” *Transportation Research Record*, (1196): 116–124.

Galle, C. 2001. “Effect of drying on cement-based materials pore structure as identified by mercury intrusion porosimetry: a comparative study between oven-, vacuum-, and freeze-drying.” *Cement and Concrete Research*, 11.

Inti, S., T. W. Evans, M. Flores, J. S. Solanki, and C. V. Chandramouli. 2021. “Permeable low-density cellular concrete (PLDCC) as a replacement for aggregate layers in permeable parking lots.” *Developments in the Built Environment*, 8: 100060. https://doi.org/10.1016/j.dibe.2021.100060.

Jones, M. R., and A. McCarthy. 2005. “Preliminary views on the potential of foamed concrete as a structural material.” *Magazine of Concrete Research*, 57 (1): 21–31.

Kearsley, E. P., and P. J. Wainwright. 2001. “The effect of high fly ash content on the compressive strength of foamed concrete.” *Cement and Concrete Research*, 31 (1): 105–112. https://doi.org/10.1016/S0008-8846(00)00430-0.

Kearsley, E. P., and P. J. Wainwright. 2002. “The effect of porosity on the strength of foamed concrete.” *Cement and Concrete Research*, 32 (2): 233–239. https://doi.org/10.1016/S0008-8846(01)00665-2.

Kozłowski, M., and M. Kadela. 2018. “Mechanical characterization of lightweight foamed concrete.” *Advances in Materials Science and Engineering*, 2018: 1–8. https://doi.org/10.1155/2018/6801258.

Lannen, T., N. D. Skinner, and J. S. Keim. 2018. *Strength and Abrasion Testing of Cellular Grout*. 12. Great Plains Regional Office, Billings, MT: U.S Department of the Interior, Bureau of Reclamation, Research & Development Office.

Lee, M. Y., D. R. Bronowski, and R. D. Hardy. 2004. Laboratory constitutive characterization of cellular concrete. SAND Report No. SAND2004-1030. Sandia National Laboratories. Albuquerque, New Mexico

Levine, D. M., P. P. Ramsey, and R. K. Smidt. 2001. *Applied Statistics for Engineers and Scientists*. Upper Saddle River, New Jersey 07458.

Liu, X., C. Ni, K. Meng, L. Zhang, D. Liu, and L. Sun. 2020. “Strengthening mechanism of lightweight cellular concrete filled with fly ash.” *Construction and Building Materials*, 251: 118954. https://doi.org/10.1016/j.conbuildmat.2020.118954.

Nambiar, E. K. K., and K. Ramamurthy. 2007. “Air-void characterisation of foam concrete.” *Cement and Concrete Research*, 37 (2): 221–230. https://doi.org/10.1016/j.cemconres.2006.10.009.

Namsone, E., G. Šahmenko, and A. Korjakins. 2017. “Durability properties of high performance foamed concrete.” *Procedia Engineering*, 172: 760–767. https://doi.org/10.1016/j.proeng.2017.02.120.

Narayanan, N., and K. Ramamurthy. 2000. “Structure and properties of aerated concrete: a review.” *Cement and Concrete Composites*, 22 (5): 321–329. https://doi.org/10.1016/S0958-9465(00)00016-0.

Ostle, B., and L. C. Malone. 1988. *Statistic in Research: Basic Concepts and Technicques for Research Workers*. Iowa State University, Ames, IA.

Pradel, D., and B. Tiwari. 2015. “The use of MSE walls backfilled with Lightweight Cellular Concrete in soft ground seismic areas.” *3rd International Conference on Deep Foundations*, 8. Mexico: Mexican Society for Geotechnical Engineering.

Ramamurthy, K., E. K. Kunhanandan Nambiar, and G. Indu Siva Ranjani. 2009. “A classification of studies on properties of foam concrete.” *Cement and Concrete Composites*, 31 (6): 388–396. https://doi.org/10.1016/j.cemconcomp.2009.04.006.

Sandler, I. S., and D. Rubin. 1979. “An algorithm and a modular subroutine for the CAP model.” *International Journal for Numerical and Analytical Methods in Geomechanics*, 3 (2): 173–186.

Schwartz, F. W., and H. Zhang. 2003. *Fundamentals of Groundwater*. John Wiley & Sons, Inc.

Seely, D., J. Bunger, J. Patten, J. Wiser, and S. Luthier. 2014. “Gas Containment and Water Exclusion Testing.” Colorado School of Mines.

Song, Y., and D. A. Lange. 2021. “Measuring dynamic Young’s modulus of low-density foam concrete using resonant frequency test.” *Journal of Testing and Evaluation*, 50 (1). https://doi.org/10.1520/JTE20200414.

Sutmoller, N. 2020. “An introduction to low-density cellular concrete and advanced engineered foam technology.” *Geo-Congress 2020*, 630–640. Minneapolis, Minnesota: American Society of Civil Engineers.

Taylor, S. 2015. “Cellular concrete: a cushion over a fault line.” *Tunnel Business Magazine*, 2015.

Taylor, S., and G. Halsted. 2021. *Guide to Lightweight Cellular Concrete for Geotechnical Applications*. Iowa State University, Ames, IA: National Concrete Pavement Technology Center.

Teig, J., and J. Anderson. 2012. “Innovative Design for the Colton Flyover Grade Separation of UPRR and BNSF, Colton, CA.” *AREMA 2012 Annual Conference & Exposition*. Chicago, IL.

Tikalsky, P. J., J. Pospisil, and W. MacDonald. 2004. “A method for assessment of the freeze–thaw resistance of preformed foam cellular concrete.” *Cement and Concrete Research*, 34 (5): 889–893. https://doi.org/10.1016/j.cemconres.2003.11.005.

Tiwari, B., B. Ajmera, R. Maw, R. Cole, D. Villegas, and P. Palmerson. 2017. “Mechanical properties of lightweight cellular concrete for geotechnical applications.” *Journal of Materials in Civil Engineering*, 29 (7): 06017007. https://doi.org/10.1061/(ASCE)MT.1943-5533.0001885.

Tiwari, B., B. Ajmera, and D. Villegas. 2018. “Dynamic properties of lightweight cellular concrete for geotechnical applications.” *Journal of Materials in Civil Engineering*, 30 (2): 04017271. https://doi.org/10.1061/(ASCE)MT.1943-5533.0002155.

Von Quintus, H., B. Killingsworth, and Harold, L. 1998. Analysis relating to pavement material characterizations and their effects on pavement performance. 223. Report No. FHWA-RD-97-085. Austin, TX. Federal Highway Administration.

Wu, H., J. Liu, and X. Zhang. 2020. "Feasibility study on use of cellular concrete for air convection embankment on permafrost foundations in Fairbanks, Alaska." *Transportation Geotechnics*, 22: 100317. https://doi.org/10.1016/j.trgeo.2020.100317.

Yoder, E. J., and M. W. Witczak. 1975. *Principals of Pavement Deisgn*. John Wiley & Sons, Inc.